NAVAL POSTGRADUATE SCHOOL

MONTEREY, CALIFORNIA

THESIS

MECHANICAL PROPERTIES OF NANO BORON NITRIDE AND MICRO BORON CARBIDE REINFORCED ALUMINUM COLD SPRAY COATINGS

by

David M. Tauber

December 2022

Thesis Advisor: Troy Ansell
Second Reader: Chanman Park

THIS PAGE INTENTIONALLY LEFT BLANK

REPORT DOCUMENTATION PAGE	*Form Approved OMB No. 0704-0188*

1. AGENCY USE ONLY ***(Leave blank)***	**2. REPORT DATE** December 2022	**3. REPORT TYPE AND DATES COVERED** Master's thesis

4. TITLE AND SUBTITLE MECHANICAL PROPERTIES OF NANO BORON NITRIDE AND MICRO BORON CARBIDE REINFORCED ALUMINUM COLD SPRAY COATINGS	**5. FUNDING NUMBERS** RMKT1
6. AUTHOR(S) David M. Tauber	
7. PERFORMING ORGANIZATION NAME(S) AND ADDRESS(ES) Naval Postgraduate School Monterey, CA 93943-5000	**8. PERFORMING ORGANIZATION REPORT NUMBER**
9. SPONSORING / MONITORING AGENCY NAME(S) AND ADDRESS(ES) Office of Naval Research (ONR)	**10. SPONSORING / MONITORING AGENCY REPORT NUMBER**

11. SUPPLEMENTARY NOTES The views expressed in this thesis are those of the author and do not reflect the official policy or position of the Department of Defense or the U.S. Government.

12a. DISTRIBUTION / AVAILABILITY STATEMENT Approved for public release. Distribution is unlimited.	**12b. DISTRIBUTION CODE** A

13. ABSTRACT (maximum 200 words)

With regards to cold spraying, wear resistant metal coatings reinforced with boron nitride nanotubes (BNNTs) have remained unexplored when compared to carbon nanotube-based composites. Using commercially pure aluminum powder, 1-3 μm B_4C powder, and BNNTs, multiple reinforced metal matrix composite powders were fabricated via high energy ball milling (HEBM). The powder compositions included an Al control, a 4 vol.% B_4C composition, a 4 vol.% BNNT composition, and a 2 vol.% B_4C with 2 vol.% BNNT composition. The compositions were sprayed onto AZ31 substrates using helium. The coatings were evaluated using nanoindentation, micro-indentation hardness, adhesion, and tensile tests. The coatings were then qualitatively evaluated under an optical microscope and scanning electron microscopes. Good dispersion of the ceramic reinforcements throughout the Al matrix was achieved via HEBM. A 14.1% increase and a 20.8% increase in micro-indentation hardness over the control were achieved for the Al/BNNT and the Al/B_4C/BNNT compositions, respectively. Adhesion testing led to the Al/B_4C/BNNT composition failing cohesively and the control failing adhesively at approximately the same force. The Al/B_4C adhesion tests experienced a combination of the two failure modes at a 31.2% increase in force over the control. Stress vs. strain curves from tensile testing demonstrated that the load is partially supported by the cold spray coating until the coating ruptures.

14. SUBJECT TERMS cold spray, high energy ball milling, HEBM, solution powder mixing, aluminum, boron nitride, BNNT, nano, nanotubes, boron carbide, magnesium, ceramic, composite, aerospace, SEM, TEM, hardness, adhesion, adhesive, cohesive, tensile strength, MMC, metal matrix composite, ceramic matrix composite, CMC, helium, B_4C	**15. NUMBER OF PAGES** 135
	16. PRICE CODE

17. SECURITY CLASSIFICATION OF REPORT Unclassified	**18. SECURITY CLASSIFICATION OF THIS PAGE** Unclassified	**19. SECURITY CLASSIFICATION OF ABSTRACT** Unclassified	**20. LIMITATION OF ABSTRACT** UU

NSN 7540-01-280-5500

Standard Form 298 (Rev. 2-89)
Prescribed by ANSI Std. 239-18

THIS PAGE INTENTIONALLY LEFT BLANK

Approved for public release. Distribution is unlimited.

MECHANICAL PROPERTIES OF NANO BORON NITRIDE AND MICRO BORON CARBIDE REINFORCED ALUMINUM COLD SPRAY COATINGS

David M. Tauber
Lieutenant, United States Navy
BS, United States Naval Academy, 2016

Submitted in partial fulfillment of the
requirements for the degree of

MASTER OF SCIENCE IN MECHANICAL ENGINEERING

from the

NAVAL POSTGRADUATE SCHOOL
December 2022

Approved by: Troy Ansell
Advisor

Chanman Park
Second Reader

Brian S. Bingham
Chair, Department of Mechanical and Aerospace Engineering

THIS PAGE INTENTIONALLY LEFT BLANK

ABSTRACT

With regards to cold spraying, wear resistant metal coatings reinforced with boron nitride nanotubes (BNNTs) have remained unexplored when compared to carbon nanotube-based composites. Using commercially pure aluminum powder, 1-3 μm B_4C powder, and BNNTs, multiple reinforced metal matrix composite powders were fabricated via high energy ball milling (HEBM). The powder compositions included an Al control, a 4 vol.% B_4C composition, a 4 vol.% BNNT composition, and a 2 vol.% B_4C with 2 vol.% BNNT composition. The compositions were sprayed onto AZ31 substrates using helium. The coatings were evaluated using nanoindentation, micro-indentation hardness, adhesion, and tensile tests. The coatings were then qualitatively evaluated under an optical microscope and scanning electron microscopes. Good dispersion of the ceramic reinforcements throughout the Al matrix was achieved via HEBM. A 14.1% increase and a 20.8% increase in micro-indentation hardness over the control were achieved for the Al/BNNT and the Al/B_4C/BNNT compositions, respectively. Adhesion testing led to the Al/B_4C/BNNT composition failing cohesively and the control failing adhesively at approximately the same force. The Al/B_4C adhesion tests experienced a combination of the two failure modes at a 31.2% increase in force over the control. Stress vs. strain curves from tensile testing demonstrated that the load is partially supported by the cold spray coating until the coating ruptures.

THIS PAGE INTENTIONALLY LEFT BLANK

TABLE OF CONTENTS

LIST OF FIGURES

LIST OF TABLES

THIS PAGE INTENTIONALLY LEFT BLANK

LIST OF ACRONYMS AND ABBREVIATIONS

Al	aluminum
Al_3C_4	aluminum carbide
Al_2O_3	alumina
ASTM	American Society for Testing and Materials
B_4C	micron boron carbide
B_2O_3	boron oxide
BNNT	boron nitride nanotube
BNNB	boron nitride nanobarb
BPR	ball to powder ratio
CMC	ceramic matrix composite
CNT	carbon nanotube
CVD	chemical vapor deposition
DOD	Department of Defense
DSC	differential scanning calorimetry
EPIC	extended pressure inductively coupled plasma
HABS	hydrogen-assisted boron nitride nanotube synthesis
He	helium
HEBM	high energy ball mill
HVOF	high velocity oxygen fuel
HTP	high temperature and pressure
IAW	in accordance with
Mg	magnesium
MMC	metal matrix composite
nD	nano diamond
Ni	nickel
RGO	reduced graphene oxide
RPM	revolutions per minute
SBM	solution ball milling
SiC	silicon carbide
SEM	scanning electron microscope

SS	stainless steel
TEM	transmission electron microscope
TGA	thermogravimetric analysis
TiC	titanium carbide
Vol.%	volume percentage
WC	tungsten carbide
Wt.%	weight percentage

ACKNOWLEDGMENTS

I would like to thank my late thesis advisor, Dr. Andy Nieto, who guided and mentored me through the start of my time at NPS and through the beginning of my thesis process.

I would like to also thank Dr. Troy Ansell, who took over without any hesitation as my thesis advisor during a very gloomy time at NPS. Thank you for letting me walk, unannounced, into your office and bounce different ideas off you throughout the day. You were a great help.

Most importantly, thank you to my wife, Katie, for being patient with me throughout the thesis process.

THIS PAGE INTENTIONALLY LEFT BLANK

I. INTRODUCTION

A. MOTIVATION

The industrial complex of the Department of Defense (DOD) is large and all encompassing. The DOD has assets ranging from micro robots to massive aircraft carriers displacing 100,000 long tons. A commonality throughout many of the DOD's platforms is that their components are made of metal or encased in metal. These metal components experience varying degrees of load, impact, thermal variation, stress, and fatigue when operating in their specific operational environments. Prolonging the life and maintenance intervals of platforms, such as aircraft, would be beneficial for cost reduction to the U.S. Government. One option to increase the life of components, specifically metallic components, are to coat them with a protective coating to enhance hardness, wear, corrosion, and tensile properties.

One of many coating options is cold spray. Cold spray, a thermal spray process, has been studied and experimented with as an option to manufacture these protective coatings. Cold spray coatings can consist of a variety of mixtures containing metallic, ceramic, or polymer particles. This thermal coating process is desirable due to its ability to adhere particles to substrates without using high temperatures to melt (or partially melt) the particles together on the substrate surface. Attractive protective coatings include metal matrix composites (MMC) and ceramic matrix composites (CMC). This study will focus on MMCs which utilize a base metal matrix and reinforcing materials to create coatings tailored for specific applications. MMCs have been shown to be effective in improving mechanical and physical properties of coatings.

Micro- and nanometric materials are two possibilities to be used to reinforce MMCs. Their size imparts unique properties to the composite. Nanotubes, which are defined as having a diameter or length of less than 100 nm, provide a very small dimension of reinforcement. Due to their size, they can fit into crevices/voids/pores to act as anchoring sites within the cold spray coating. A nanometric material becoming increasingly commercially available is a ceramic known as boron nitride nanotubes (BNNT). BNNTs,

which have a small diameter and are long, are enticing due to their desirable and contrasting properties over other, more common nanomaterials such as carbon nanotubes (CNT).

B. OBJECTIVES

The main objective of this thesis is to fabricate new ceramic particulate reinforced aluminum nanocomposite powders for use in cold spray applications. The goal is for these dual reinforced MMCs to have enhanced properties over commercially pure aluminum powder. The ceramics utilized in the MMC will combine varying volume percentages (vol.%) of micro- boron carbide (μB_4C) and BNNTs. Boron carbide and boron nitride are classified as ceramics. Currently, there is no published literature on cold spraying BNNTs and specifically Al/B_4C/BNNT MMCs. This thesis will lay a foundation for future studies into BNNT reinforced MMCs. All coatings and powder microstructures will be characterized through combinations of scanning electron microscope (SEM), transmission electron microscope (TEM), and optical microscope. Mechanical tests and characterization will include nanoindentation, micro-indentation, adhesion testing, and cold spray coated tensile testing.

II. BACKGROUND

A. GAS DYNAMIC COLD SPRAY

At its most basic level, gas dynamic cold spray (or just cold spray) is a material deposition technique that utilizes a fine powder propelled at high velocities onto a substrate to produce a solid protective coating or barrier. This process is a subset of thermal spraying but unlike most thermal spray processes (the most common being high velocity oxygen fuel (HVOF)), cold spray does not utilize temperatures above the melting temperature of the powder. Traditional thermal spray methods melt powder particles as they are propelled onto the substrate. These melted particles adhere to both the substrate and to other particles, and then quickly solidify. Instead, cold spray achieves adhesion by accelerating particles to extremely high velocities, using a carrier gas, on the order of 300–1200 m/s [1]. The carrier gas, which is heated, imparts high amounts of kinetic energy onto metallic or ceramic particles. Figure 1 compares cold spray's velocity and lower operating temperatures, 100–500ºC [1], verse other thermal spray methods. These high particle velocities are possible by sending a pressured carrier gas (generally inert) through a convergent-divergent de Laval nozzle. Since cold spray does not melt the powder particles the final coatings display many of the same characteristics and mechanical properties as the original powder particles [2]. When compared to other thermal spray coatings, cold spray coatings exhibit less porosity, high homogeneity, increased hardness, less oxide formation, less shrinkage, and a higher Young's modulus [2].

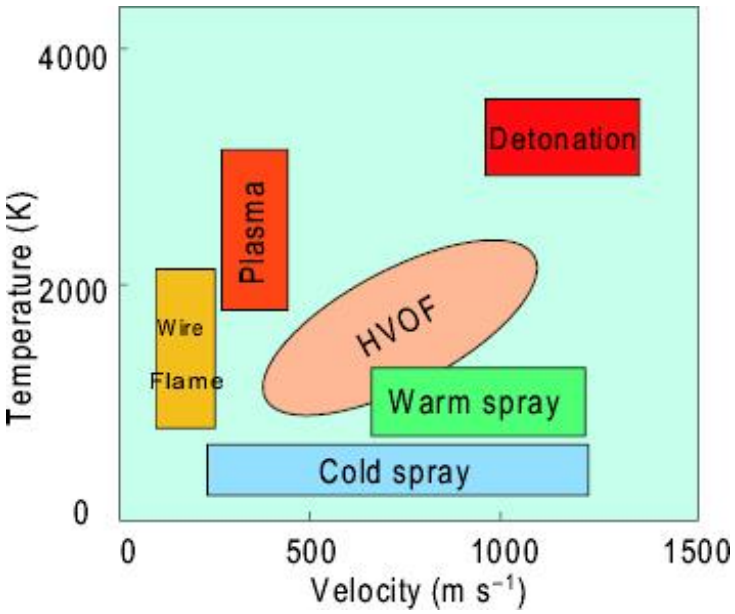

Figure 1. Comparison of thermal spray processes. Source: [3].

A traditional cold spray apparatus contains a compressed source of the carrier gas, an operating/control panel, a powder feeder, a heater, and the de Laval nozzle, see Figure 2.

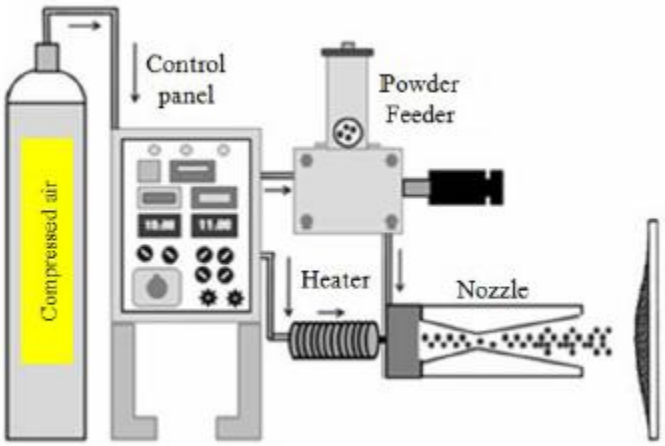

Figure 2. A simple diagram of the cold spray process and equipment. Source: [2].

The powder particles must meet or exceed a certain velocity to adhere to the substrate [4]. This velocity is based off parameters such as material properties, pressure, temperature, gas type, stand-off distance, nozzle design, etc., and is referred to as the critical velocity [5]. When the powder particles reach their critical velocity and collide into the substrate, they plastically deform. These flattened out particles are referred to as splats. Figure 3 identifies important colds spray parameters that affect material deposition and mechanical properties. Within the cold spray community, there is debate on how these splats physically adhere to each other and the substrate. One idea is that during the permanent deformation of the particles there is damage to the thin surface layer, an example being an oxide layer, of the splat or substrate. Since the splats are in such close contact, a form of pressure bonding takes place [6]. A second theory is that metallurgical bonding occurs between the substrate and splats due to phase transformations. When the particles undergo severe plastic deformation their surface area increases. The increased surface area experiences friction with the substrate and leads to the coating staying in place with no chemical reactions between the materials [7]. A third theory is that when the splats impact the substrate or each other they experience diffusion bonding or metallurgical bonding attributed to molten impact from shear instability [8]. Whichever theory is correct, and it is likely a combination of the three, cold spray does not rely on the melting of powders. This gives the technique advantages over other thermal spray coating techniques.

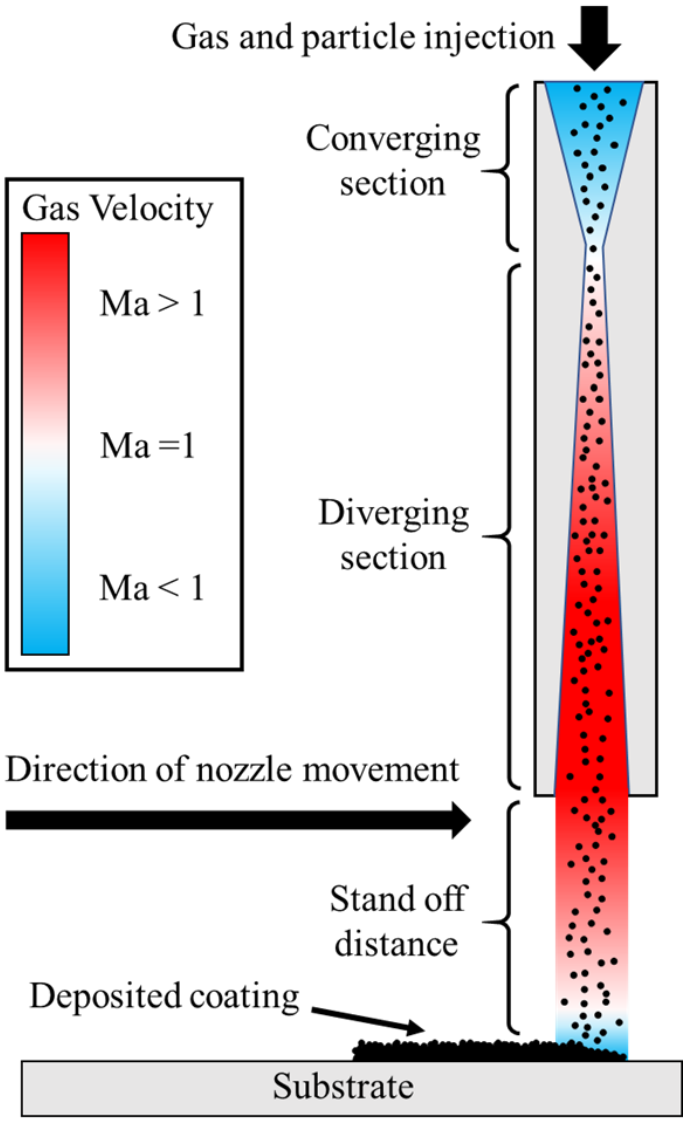

Figure 3. Cold spray parameters and definitions. Source: [9].

An additional advantage of cold spray is the equipment can be designed to be mobile. Most cold spraying is done within a lab or manufacturing environment, but the comparably lower temperatures required to cold spray allow equipment to be scaled down and made portable. A portable apparatus would encourage repairs or coatings to be completed outside a manufacturing environment. If cold spray can become more portable and accessible, personnel in the DOD and industry will potentially be able to increase a wide range of component's shelf life by employing the technology.

B. EFFECTS ON ADHESION

Although the cold spray adhesion mechanism is still being debated, there is no argument on the importance of adhesion within cold spay. Adhesion between the substrate and the cold spray coating as well as the cold spray coating to itself is critical to achieve resilient and resistant cold spray coatings. There are many factors that can influence adhesion but measured adhesion strength is largely dependent on the velocity and the imparted thermal interaction when a powder interacts with a surface during the cold spray process [8]. The gas that carries the particle to the substrate can also affect the adhesion strength of the coating by changing the critical velocity of the particle. The most common carrier gases are inert helium and nitrogen; compressed air can be used as well. A study by Gilmore et al. [10], found that helium is the best option to use as the carrier gas during cold spray. Helium can reach higher peak particle velocities verse the other gases when tested at equal inlet conditions. The lower density of helium allows the gas particles to encounter less drag force [10]. This will equate to higher powder exit velocity from the de Laval nozzle. To obtain the high particle velocity, nitrogen can be utilized with a higher carrier gas temperature, or helium can be used without increasing the carrier gas temperature [8]. Another factor that can affect adhesion strength is the characteristics of the feedstock and substrate material [11]. In general, hard substrates will have a lower adhesion strength than soft substrates. Soft substrates will experience higher adhesion strength due to jet formation or the process of a powder particle, soft or hard, slightly eroding the surface of the substrate [11]. Regarding adhesion, the ideal combination is a feedstock material that can slightly penetrate the substrate and simultaneously deform into a flat splat [11].

C. POWDER PROCESSING

There are many approaches to process or fabricate a composite powder. Ball milling is a proven technique with multiple subsets that include high energy ball milling (HEBM), cryogenic mechanical milling (cryomilling), solution ball milling (SBM), rotational milling modeling, and shift-speed ball milling [12]. The general idea behind ball milling is a mixture of powders is placed into a milling jar with milling media. Then the milling jars are rotated at high RPMs for specific periods of time to thoroughly mix the powder.

HEBM is the most common mixing and dispersion technique; as well as the simplest. Cylindrical metal jars are filled with the powder(s) and milling balls made of a hard, unreactive metal or a ceramic. The ratio of the milling balls to the powder (BPR) has an influence on the post processed metal characteristics. For example, a 1:5 BPR would indicate that for a 60 g sample of powder, there would be 12 grams of milling balls. These jars are placed into a planetary ball mill or high energy mill. The milling machine shakes at high RPMs, transferring energy to the milling balls and the powder within the jars. The machine is turned off and on for specific intervals. Close attention must be paid to the powder due to the high amounts of heat that occur within the jars; this high heat can cause cold welding or sintering of the powder and milling balls [12]. After the milling is finished, the mixed powder must be assessed through a microscopy technique, such as a scanning electron microscope (SEM), to ensure the powder's morphology, physical characteristics, and dispersion is satisfactory. HEBM can be destructive if not performed correctly [12].

Cryomilling is a ball milling process that uses a cryogenic media to keep the material cool throughout the milling process. Cryomilling has some advantages over HEBM in producing nanostructured alloys, primarily due to the reduction in heat. This reduction in heat encourages deagglomeration of nanoparticles and oxidation is reduced [12].

The final ball milling method that will be discussed is solution ball milling (SBM). Wet chemistry and conventional ball milling are combined to deagglomerate and mix nanoparticles. A solution (often isopropanol with surfactant) is mixed with a low wt.% of nanoparticles. The solution is milled with milling media to create a slurry. The slurry settles and the upper solution is poured out. The final slurry is dried in an oven. The final powder is generally less damaged and flakier than processing through HEBM [12].

D. BORON CARBIDE REINFORCED METAL MATRIX COMPOSITES

Cold spray coatings can be fabricated from one single elemental powder or many combinations of metals, alloys, and/or ceramics. There are applications in which a deposited layer of pure metal is chosen; likely applications where the protective coating is monitored and replaced or repaired periodically. Often, the environments in which a cold

spray coating is utilized is less predictable. The coating must be able to perform optimally when facing diverse conditions such as corrosion, impact, wear, and high temperature, to name a few. MMCs provide solutions to these dynamic problems.

MMCs have been utilized to improve mechanical and physical properties of multiple materials by employing a base metal and improving its properties with reinforcing metals or ceramics. These composites can be reinforced by particles, short fibers or whiskers, continuous fibers, or layering, see Figure 4 [13]. Due to the versatility of MMCs and the ability to refine material properties without large increases in material weight, MMCs are an area of interest to the aerospace, defense, robotics, and marine industries. When fabricating an MMC, in this case to specifically increase hardness and tailor adhesion strength, the base metal is typically ductile and the ceramic reinforcement hard. There are many different ceramic reinforcements used in MMCs, but two commonly studied ceramic classes are oxides and carbides. This combination of the tough, ductile base metal matrix reinforced with a hard ceramic theoretically makes a MMC with an increased hardness and resistance to wear [14].

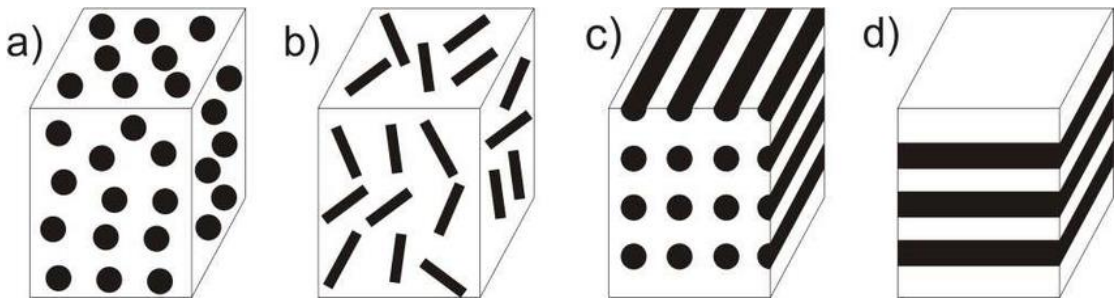

Figure 4. Metal matrix composite reinforcements a) particles b) short fibers c) continuous fibers d) layering. Source: [13].

Nearly any metal powder can be used as the matrix for an MMC. However, this does not mean that any metal is the correct choice for an MMC matrix. Post fabrication imagery, such as SEM images, often reveal the compatibility of the metal matrix and its associated reinforcement. Aluminum powder (as well as aluminum alloys) is often used as the MMC matrix material due to its tailorability and favorable materials properties. These

properties include corrosion resistance, ductility, low density, and a high strength to weight ratio [15].

A ceramic reinforcement that has good properties and an ability to improve the mechanical qualities of a MMC coating is boron carbide. The specific properties that make B_4C a candidate for MMC reinforcements include a low density (2.51 g/cm^3), high modulus (445 GPa), high melting point (2450ºC), high thermal stability, and good chemical resistance when compared to other common reinforcing ceramics such as silicon carbide (SiC) and aluminum oxide (Al_2O_3) [16]. B_4C is also the third hardest material [17]. Uniquely, B_4C has a high ability to absorb neutrons which makes a cold spray coating composed of a B_4C reinforced MMC a prime candidate for neutron shielding applications [14].

As advertised, many ceramics have desirable properties that would work well in an MMC, but when these materials are utilized in MMCs they often do not produce the expected results. Lee et al. [14] studied how reinforcing carbide ceramics effect the deposition efficiency, hardness, and wear resistance of a low-pressure cold spray coating. The matrix utilized was nickel (Ni) and the carbides were B_4C, titanium carbide (TiC), and tungsten carbide (WC). The carbide with the highest fracture toughness, WC, not the highest hardness, B_4C, had the highest deposition efficiency. Due to the lower fracture toughness of B_4C, the particles experienced increased rates of fracture and in turn rebounded from the surface during the spray, causing a lower deposition efficiency than the other carbides [14]. Although the micro-hardness of all three reinforced MMCs were similar, the poor deposition efficiency of B_4C led to the highest wear rate [14]. The density and hardness of B_4C continues to make the ceramic an enticing reinforcement option. By altering cold spray parameters such as the carrier gas, deposition rate, and pressure an MMC successfully reinforced with B_4C would create a resilient coating.

Deciding to use B_4C as the reinforcement is just the first step. The next question that arises is what size and how much B_4C should be used in the dual reinforced MMC coating being fabricated? Lee et al. [14] found that the largest improvement in micro-hardness occurs when the reinforcing carbide vol.% is between 3–15; although percentages less than 3 vol.% were not studied. B_4C powders vary immensely in size. The size ranges

from the tens of microns down to the nanoscale. Sova et al. [18] found that small, fine ceramic particles (< 20 μm) can roughen the substrate surface as well as previously deposited layers to promote adhesion, while large particles hinder layer growth. Nieto et al. [19], studied different size B_4C reinforcements within an aluminum matrix. Nano-B_4C was found to have superior properties over micron and sub-micron B_4C. The powders from this study were fabricated under controlled laboratory conditions through cryogenic mechanical alloying and dual mode dynamic forging; these powders were not cold sprayed. Nano-ceramic reinforcements tend to agglomerate due to their high surface energy [12]. When processing MMCs via a HEBM an increase in temperature can increase the surface energy of the nano-B_4C; the heightened temperature increases the potential for these particles to then agglomerate [20]. Utilizing HEBM to manufacture the powders that will already contain a nanomaterial, BNNT, suggests that B_4C on the low micron (1-10 μm) scale may be appropriate.

E. BORON NITRIDE NANOTUBES

BNNTs, which exhibit unique properties, have a wide range of applications including semi-conductors, mechanical reinforcements, heat sink layers, piezoelectric applications, neutron shielding, and filtration [21]. As previously mentioned, literature relating to cold spraying of BNNTs is non-existent; this is one of the primary reasons this study is being undertaken. Generally, literature on the topic of BNNTs (not just cold spray) is quite low when compared to the more mainstream carbon nanotubes (CNT). Figure 5 illustrates the large difference between the number of peer-reviewed publications found on the Scopus database from 2000–2019 [22]. A possible reason for this contrast is the manufacturing challenges associated with producing BNNTs.

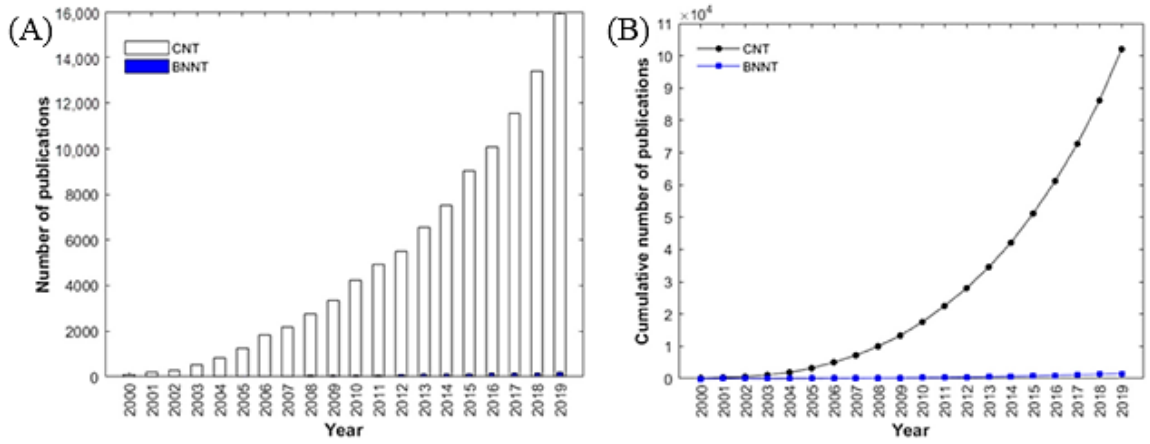

Figure 5. BNNT publications: (A) annual peer-reviewed (B) cumulative peer-reviewed. Source: [22].

Manufacturing challenges related to large scale production of BNNTs, such as high temperature and pressure, is one of the main reasons as to why these ceramics are not utilized to a greater capacity in material applications [23]. Throughout literature, CNTs and BNNTs are compared or co-exist largely due to their similar properties and tubular structure. CNTs, unlike BNNTs, have been successfully produced at large scale for over 20 years using multiple different synthesis techniques. Companies who produce and sell BNNTs often keep their proprietary manufacturing techniques in house, but academics have successfully recreated, invented, and improved upon many synthesis and manufacturing processes. These processes can cover both the bottom-up and top-down approaches to associated with producing nanomaterials.

Kim et al. [23] studied the tradeoffs of BNNT synthesis techniques that have attempted to be scaled up. Successful synthesis of BNNTs can have trades off; two of which are cost and toxicity. To avoid the toxicity of B-N-H compounds used in producing H-BN phases, the simple reaction of $2B + N_2 \rightarrow 2BN$ showed promise [23]. This reaction could be used to scale up production, but the high temperature and pressure reactions remained a barrier that needed to be overcome. A simple, and cheap solution was ball milling boron powder in a NH_3 atmosphere. Then, post ball milling, the boron powder was annealed at high temperatures (1200ºC) in an N_2 atmosphere (later ammonia was used) achieving high yield production of low purity BNNTs [24]. Other more complicated and limiting synthesis

techniques of BNNTs include chemical vapor deposition (CVD), high temperature and pressure (HTP) method, hydrogen-assisted boron nitride nanotube synthesis (HABS) method and extended-pressure inductively coupled plasma (EPIC) method [23]. These techniques often continue to lack scalability, are difficult to consistently reproduce high quality BNNTs, and require reliable sources of boron, which can be scarce [23].

The scalability and quality of BNNTs does continue to improve. Since their inception in 1995 [25], nanotube production has continued to scale up from milligrams of low quality BNNTs to kilograms of high quality BNNTs being readily accessible for purchase [23].

BNNT's crystalline structure, like CNTs, are sp^2 bonded atoms that make up hexagonal rings [21], see Figure 6. The biggest difference in the crystalline structure is that the BNNTs are made up of alternating, polar covalent B-N bonds (instead of covalent C-C) bonds. The bonds are considered polar covalent due to the differences in electronegativity between boron and nitrogen [22]. This difference in electronegativity gives BNNTs one of its most unique characteristics: electrical insulation [21].

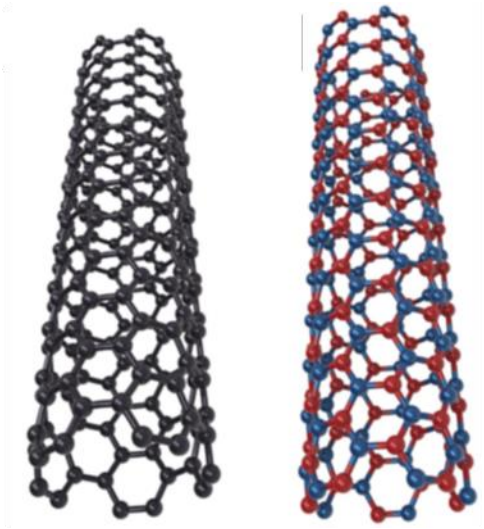

Figure 6. Structure of CNT (left) and BNNT (right). The blue atoms represent boron, and the red atoms represent nitrogen. Source: [21].

Like all nanomaterials, a nanotube is defined as having one dimension less than 100 nm. In the case of nanotubes, the dimension that characteristically meets this criterion is its diameter. The first published instance of a BNNT was a multi-walled nanotube with inner diameters of 1 to 3 nm and lengths up to 200 nm [25]. More recently, BNNTs have been produced with lengths as long as 100–200 μm [26]. As industry continues to produce further extended BNNTs, the applications and uses of this nanomaterial will continue to evolve.

BNNTs exhibit astonishing mechanical properties with a tensile strength up to 61 GPa [27] and are the strongest lightweight nano material with a Young's modulus of ~1.2 TPa [28]. They have a high thermal conductivity comparable to CNTs [28]. BNNTs exhibit less curling than CNTs due to strong interlayer bonding [22] which reduces agglomeration during dispersion. Additionally, they retain high flexibility and fracture toughness [30]. Other properties of interest include BNNT films that displayed tunable hydrophobic and wettability properties [28], transparency in visible and infrared regions with absorption in UV regions [23], thermal neutron absorption [23], and the ability to produce electricity when mechanically bent deformed or straightened [29].

Many of the aforementioned properties are similar to CNTs. This is one of the primary reasons BNNTs and CNTs are often associated throughout literature and experiments. However, BNNTs do exhibit some unique properties (from CNTs) that make this ceramic enticing for specific applications and fields of study/industry. One such property is its thermal stability and oxidation behavior. Kostoglou et al. [22], conducted differential scanning calorimetry (DSC) and thermogravimetric analysis (TGA) tests on both BNNTs and CNTs in synthetic air up to 1300°C. The tests found that BNNTs remains stable until ~900°C and fully oxidized to B_2O_3 at ~1100°C. This substantially outperformed CNTs which remailed stable only until ~450°C and were fully burned off at 800°C. At the conclusion of the test, the BNNTs did not burn off [22]. These results are significant and assert that BNNTs can be an important material for reinforcement in high temperature applications such as aerospace.

Another unique property is the electrical insulation ability of BNNTs (while also being thermally conductive). Of note, CNTs are electrically conductive, thus a side-by-side

comparison between these two nanomaterials is unnecessary. Kim et al. [21], discussed BNNTs excellent insulating behavior due to a wide band gap of 5–6 eV. This is not due to the chirality or diameter of the nanotubes but rather the difference in electronegativity within the B-N bonds; boron (2.04) and nitrogen (3.04) [21]. The high thermal stability paired with the thermal conductivity and electrical insulation make BNNTs a promising choice for electronic applications.

Two studies have successfully employed BNNTs or boron nitride nano-platelets (BNNPs) by thermal spraying. Pandey et al. [30] reinforced an Al_2O_3 matrix with 5 vol.% BNNT for use in plasma spraying. Al_2O_3 with CNTs as a reinforcement is common, but at temperatures above 1800ºC, aluminum carbide (Al_3C_4) can form; this carbide can have negative effects on the coating's mechanical properties. Post spraying, only the reaction product of AlB_{10} was found and imaging showed the BNNTs to be uniformly distributed throughout coating. The BNNT composite showed an increase in relative density, hardness, and fracture toughness when compared to the alumina control sample [30].

The second study was conducted by Norrell et al. [31] and utilized a dual reinforcement MMC; the matrix was aluminum, and the reinforcements were 2 vol.% each of nano-B_4C and BNNPs. The powder was fabricated via cryomilling and then cold sprayed utilizing helium as a carrier gas onto an AA6061 substrate. Imaging of the post cryomilled powder showed good coating uniformity of the reinforcements on the aluminum powder. Dual nano reinforced coatings were found to have a 12% increase in hardness over the pure aluminum coating [31]. However, the reinforced coatings did show increased susceptibility to pitting corrosion, and after long exposure to a corrosive environment the aluminum substrate and coating both showed signs of galvanic corrosion.

F. DUAL REINFORCEMENT METAL MATRIX COMPOSITES

Dual reinforcement MMCs add an additional reinforcement to a conventional MMC. These highly tailored MMCs are manufactured to provide additional improvements to the metal matrix and its single reinforcement. The goal of any MMC is to achieve a synergistic effect of particular material properties. For example, an aluminum matrix reinforced with µ-SiC and nano graphene platelets would ideally produce a hardness value

greater than the hardness of the two reinforcements and the aluminum matrix. Achieving a synergistic effect is often easier said than done. Dual reinforcement MMCs are not new, but what is new is the different reinforcements being utilized, the amount of the reinforcements, the manufacturing process, the size of the particles, and the application of the reinforcements.

Li et al. [32] manufactured an aluminum matrix composite reinforced with reduced graphene oxide (RGO) and CNTs using a flake powder assembly process. The final vol.% of the RGO-CNT hybrid was 1.5 vol.%. The dual reinforced MMC was then manufactured into tensile specimens. The dual reinforced MMC bar showed a 60% higher tensile strength than the pure aluminum matrix tensile bars with increases in both Young's modulus and yield strength. The study determined these synergistic effects in strengthening are due to a network of interconnected RGO and CNTs connected throughout the matrix [32].

A study conducted by Kwon et al. [33] utilized nano-diamond (nD) and multi-walled CNTs to reinforce an aluminum matrix. Mechanical ball milling was used to create a 1 vol.% mixture of each nano-reinforcement with aluminum. This powder was then hot-pressed into a bar for testing. The dual reinforced MMC hardness and flexural strength were five and seven times higher, respectively, than pure aluminum. The even distribution of the nD and CNTs within the matrix and ultimately the hot-pressed bar allowed for good load transferring capacity during testing [33].

Zhang et al. [34] utilized nano-SiC to promote the dispersion and deagglomeration of CNT reinforcements in an aluminum matrix, as well as to act as a reinforcing particle. Multiple dual reinforcement MMCs, between 0.25 and 0.75 vol.% per reinforcement, were fabricated using ultrasonic dispersion, planetary ball milling, spark plasma sintering, and finally hot extrusion through a die. The 0.5 vol.% reinforcement increased the tensile strength over pure aluminum by 94%. SiC did work to better disperse CNTs in the matrix and prevent CNTs from peeling or pulling out. Well dispersed CNTs contributed to the increase in tensile strength by transferring load and hindering dislocation movement when the aluminum matrix experiences plastic deformation [34].

This study will utilize ball milled powder cold sprayed onto a Mg substrate utilizing He as the carrier gas. The powders will be comprised of combinations of Al, B_4C, and BNNTs. Post cold spraying, the coatings will undergo tests to quantify the effect the MMC reinforcements have on the mechanical properties of the various composite coatings. Throughout testing, the pure aluminum powder will be used as the control cold spray coating for comparison. Advanced characterization methods will be used to evaluate the different cold spray coating's microstructures and results from the mechanical testing.

THIS PAGE INTENTIONALLY LEFT BLANK

III. MATERIALS AND EXPERIMENTAL PROCEDURES

A. SELECTION OF MATERIALS

1. Commercially Pure Aluminum

This study will utilize commercially pure Al as the base metal matrix for the cold spray coating. Al was chosen as the base matrix due its tailorable properties and its good resistance to corrosion. Additionally, pure Al is soft and relatively weak when compared to other structural metals. These properties make Al a good base metal matrix candidate to use ceramics as reinforcements. Pure Al was chosen over Al alloys to reduce the number of variables (alloying metals) that can possibly influence the characteristics or properties of the cold spray coatings, as well as pure Al's good machinability.

The Al powder was sourced from CenterLine Supersonic Spray Technology (Catalogue No. SST-A5001). The composition is minimum 99.5% pure Al and the particle size ranges from 5 to 45 μm [35]. Particles, as received, from the manufacturer are seen in Figure 7. Particles have an irregular, rounded morphology. The morphology of the powder may be altered by HEBM, but the goal is for the morphology to remain non-flattened. A flattened particle will have different aerodynamic characteristics than the original rounded powder when injected into the high velocity helium carrier gas flow. If the orientation of the flattened particles is not optimized, they risk not being picked up in the carrier gas. The flattened particles that are injected into the gas flow, will not likely reach the critical velocity required to adhere to the substrate or previously deposited cold spray layer, resulting in a poor deposition efficiency. The average particle size of the powders in Figure 7 aligns with the manufacturer's specifications.

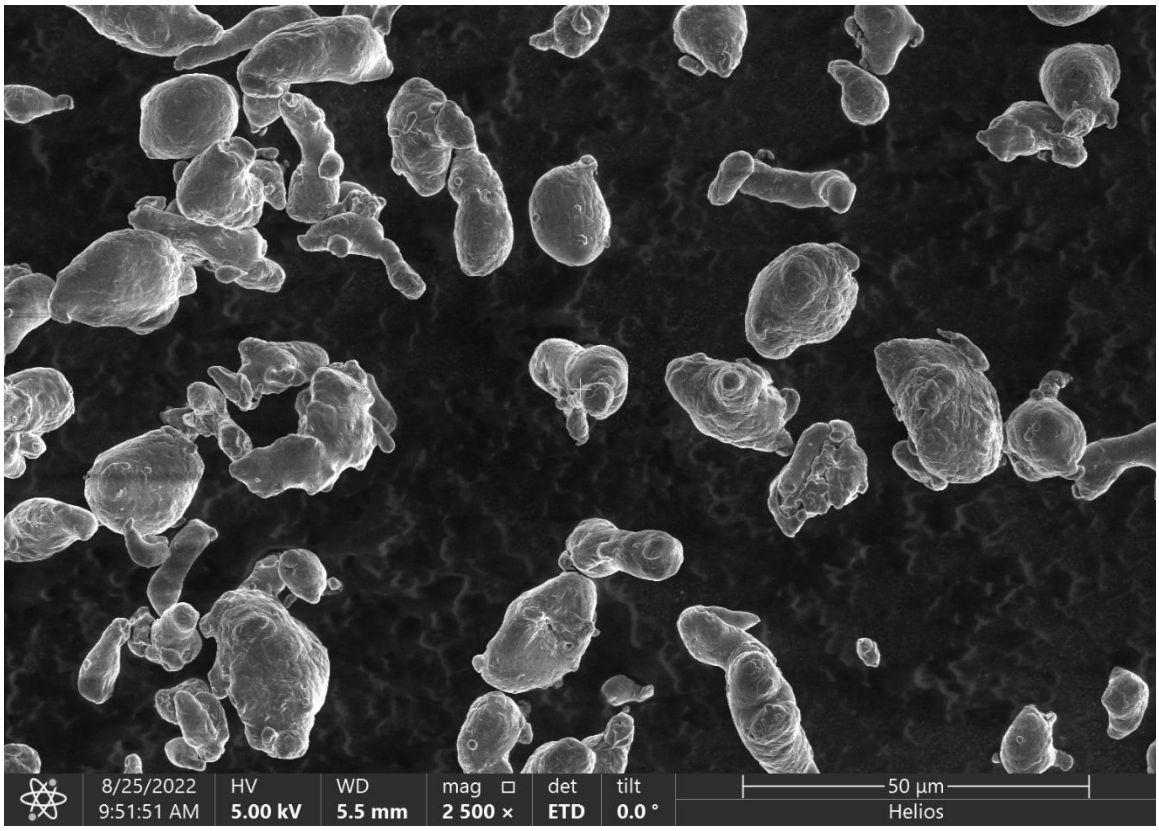

Figure 7. Aluminum powder as received from manufacturer

2. Ceramic Reinforcements

As discussed in Chapter 1, Section B, "Objectives," two ceramic reinforcements were chosen for this study: µB_4C and BNNTs. The B_4C was sourced from U.S. Research Nanomaterials, Inc (Stock No. US1020M). The purity is 99.9% and consists of particles ranging in size from 1 to 3 µm [36]. The B_4C particles are irregular shapes and appear to have slightly jagged edges that resemble a brittle fracture. B_4C's morphology allows it to be easily identified in the mixed powder SEM images and SEM images of the sprayed coating. Figure 8 is a TEM image of the B_4C particles taken by the manufacturer and Figure 9 is an SEM image of the particles.

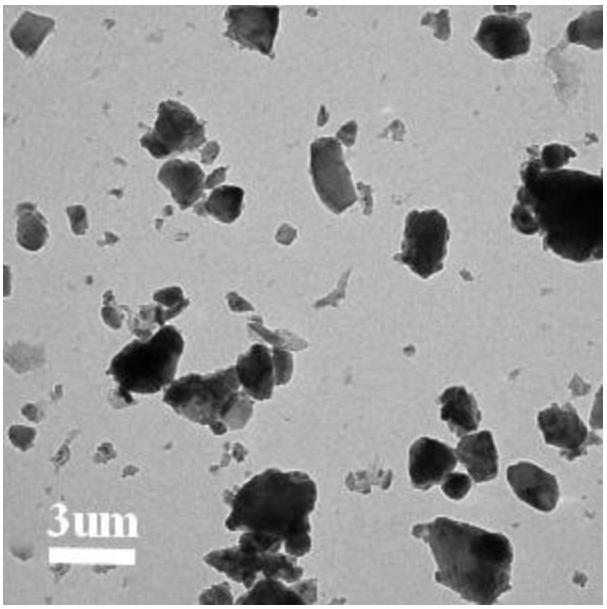

Figure 8. TEM image of B_4C. Source: [36].

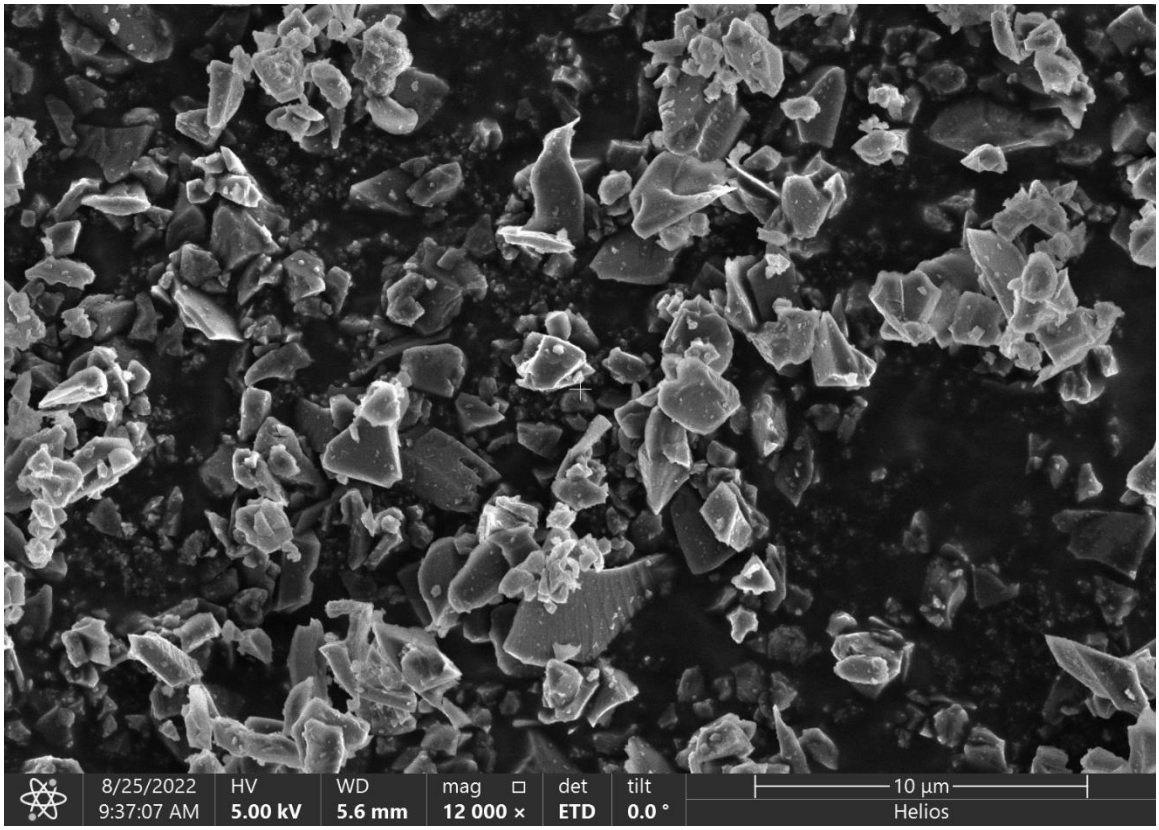

Figure 9. SEM image of B_4C, as received from manufacturer

The uniqueness of this study lies with the use of BNNTs as a reinforcement within the cold spray coating. In recent years, more companies are beginning to manufacture high yields of BNNTs. The BNNTs chosen are manufactured by BNNano (BNNB-P-90A1). BNNano refers to these BNNTs as "Boron Nitride Nanobarb(s)^{TM}" due to the nanotubes irregular shape and the resemblance of barbs along the outer nanotube walls. Figure 10 shows a TEM image of a nanobarb from BNNano. Note that the terms "nanotube" and "nanobarb" will be used synonymously throughout this study. The powder produced by BNNano is greater than 90% nanobarbs. The nanotubes have a wall count of 1–3, a nominal width of 60 nm, and a nominal length of 20 μm [37]. As received from the manufacturer, the BNNTs appear to be agglomerated. Figure 11 is a SEM image showing a deagglomerated BNNT surrounded by clusters of agglomerated BNNTs.

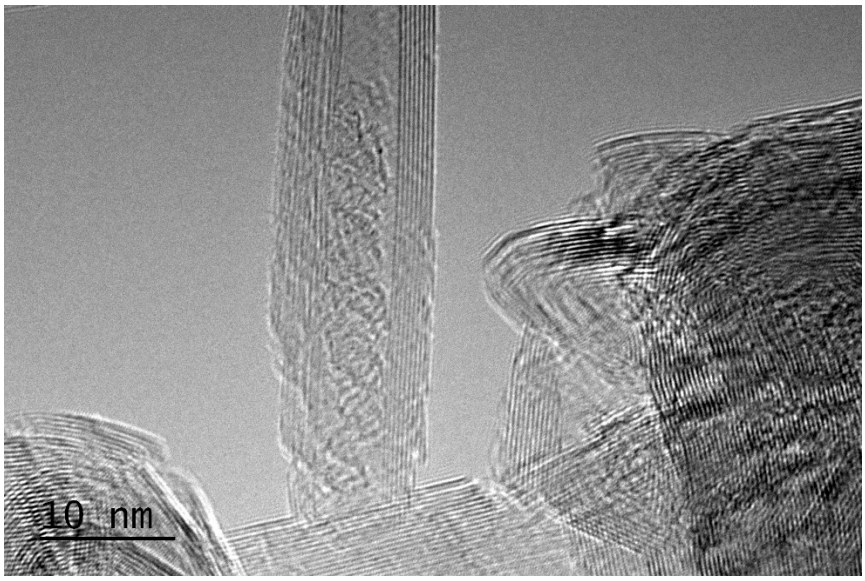

Figure 10. BNNT TEM image as received from manufacturer

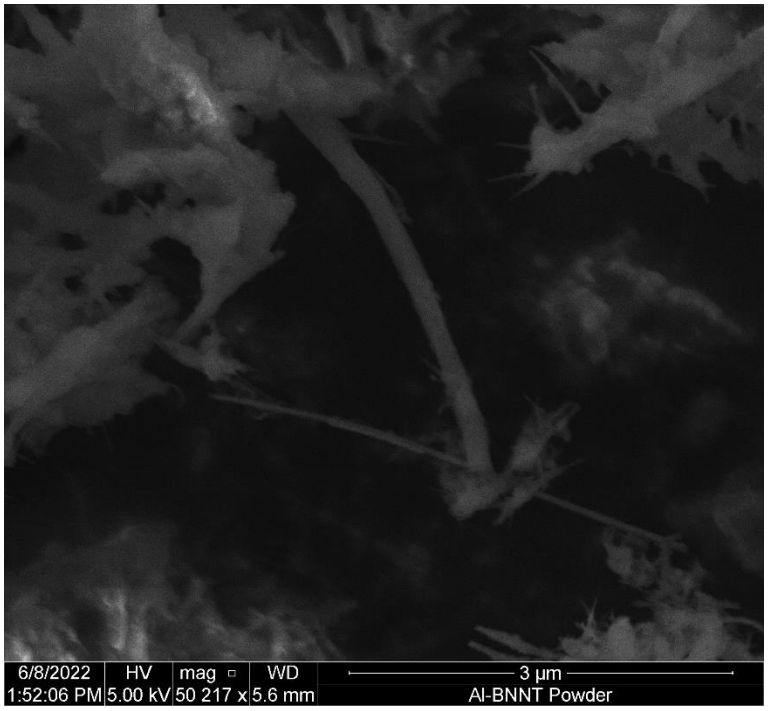

Figure 11. Various morphologies and agglomerations of BNNTs under the SEM

3. Magnesium Substrate

The substrate for this study was an AZ31 Mg alloy. Multiple substrates were cut into rectangular bars measuring approximately 153.0 x 22.5 x 9.4 mm; some of these bars were machined into tensile testing specimens. The AZ31 alloy consists of a combination of the elements shown in Table 1.

Table 1. AZ31 Alloy Elemental Composition, wt%. Source: [38].

Al	Zn	Mn	Si	Cu	Ni	Fe	Mg
2.5-3.5	0.6-1.4	0.2-1.0	0.1	0.05	0.005	0.005	Balance

AZ31 was chosen as the substrate material due to its low density, light weight, and good mechanical properties. These properties contribute to why AZ31 is often used in

multiple aircraft parts throughout the aircraft manufacturing industry [39]. Reinvigorated interest in space has sparked interest in Mg alloys for weight reduction, but its lack of flammability resistance and corrosion resistance has hampered increased use [40]. A coating containing BNNT's, which have high temperature stability and very good electrical insulation properties, could allow aircraft and space industries to re-evaluate their use of Mg.

B. HIGH ENERGY BALL MILLING

Four compositions combining Al, B_4C, and BNNTs were milled together using various vol.%, see Table 2. Note that the Al/B_4C/BNNT composition will sometimes be referred to as "All3."

Table 2. Coating Composition Summary

Composition ID	Al [vol.%]	B_4C [vol.%]	BNNT [vol.%]
Al	100	0	0
Al/B_4C	96	4	0
Al/BNNT	96	0	4
Al/B_4C/BNNT	96	2	2

Each composition required a minimum of 120 grams of powder for multiple samples to be cold sprayed. Due to limited quantities of powders, specifically BNNTs, the compositions were calculated and measured using densities provided by the manufacturers, recorded in Table 3.

Table 3. Densities of Powders

Powder	Density [g/cm^3]
Al	2.70
B_4C	2.52
BNNT	2.29

The fabrication of the composite powders was conducted via HEBM. As referenced in Chapter II, Section C, "Powder Processing," HEBM combines the powder with a milling media into a cylindrical metal jar and is shaken at high RPMs. The milling media and the powder collide causing powder particles to deagglomerate, spread evenly throughout the matrix, and cold weld to each other. The final milled powder should retain its original irregular, rounded shape and have reinforcing ceramics distributed throughout.

The milling machine used was the SPEX SamplePrep Mixer/Mill 8000D which operates at approximately 1060 cycles per minute [41]. Rice experimented with different BPR using Al as a matrix with B_4C and graphene nanoplatelets as the ceramic reinforcements [9]. The experiment utilized BPR of 1:10, 1:5, 1:1, 2:1, and 5:1 with cycles of 2, 10 and 30; each cycle being 2 min of the machine rotating (on) and 5 min of the machine resting (off). A BPR of 1:5 was the most effective in keeping the cold spray powder small, cylindrical, and uniform. These results were used as the starting point to create the composite powder for the current experiment.

Initially, 75 g of the Al powder and the Al/B_4C powder was milled using a BPR of 1:5, and 10 cycles (5 on, 5 off). Immediately, it was evident that the 75 g of powder had difficulty fitting with the 15 g of 304 stainless steel balls in the metal jar. The powder had to be repeatedly tamped down to fit the entire 75 g. When milling was complete, the Al matrix retained its original shape, but the B_4C had not been adequately distributed and remained slightly agglomerated.

The next run looked to properly distribute and deagglomerate the B_4C within the Al matrix. 50 g of the Al powder and 50 g of the Al/B_4C powder was milled using a BPR of 1:3, and 10 cycles (5 on, 5 off). Less powder within the mixing jar allowed for more open space. This open space allowed the 304 stainless steel mixing balls to impart more momentum and do more work onto the powder. For the Al/B_4C powder, the Al matrix still retained its original shape and the B_4C was better distributed. See Figure 12 for a comparison between the two Al/B_4C milling parameters.

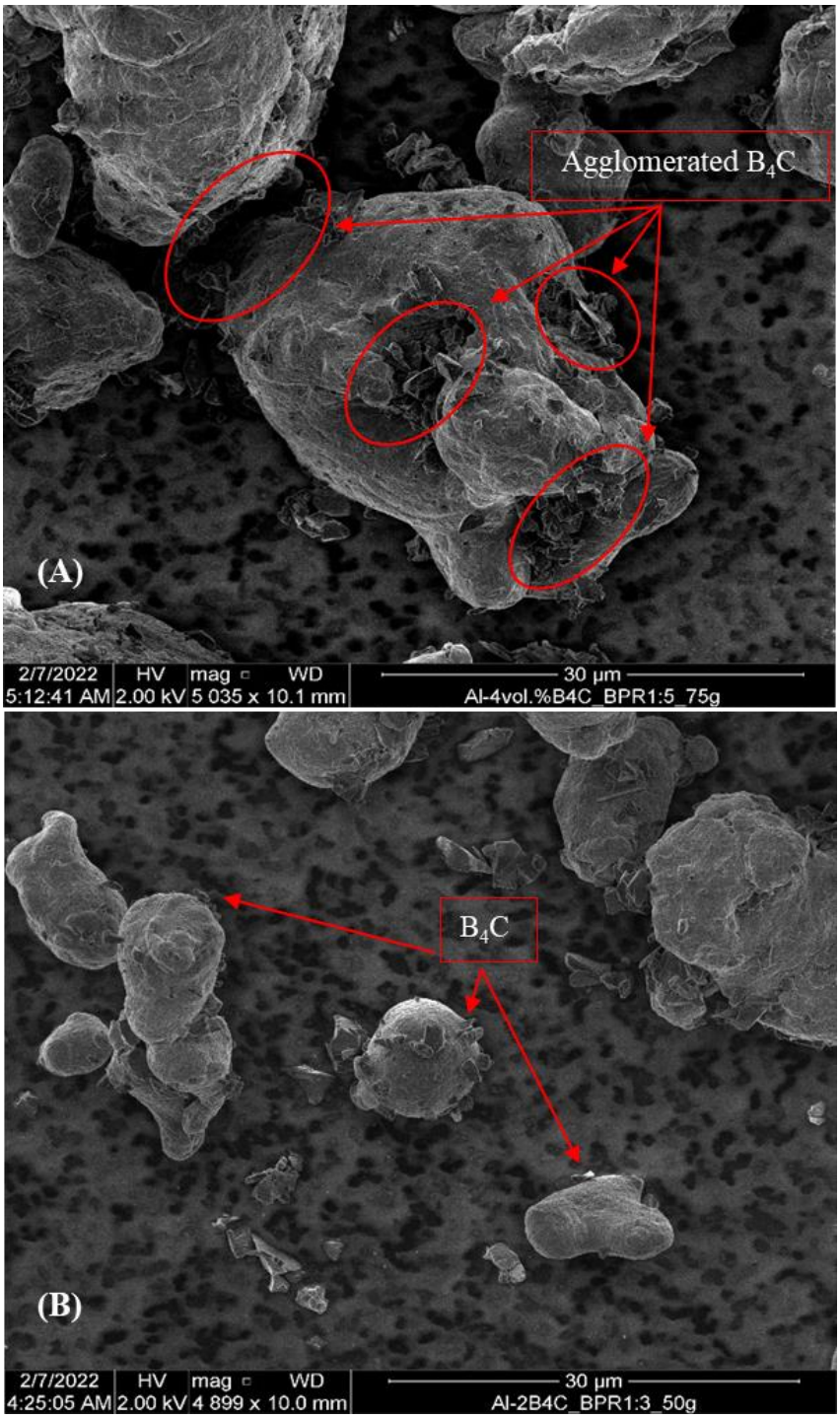

Figure 12. Al/B_4C HEBM trial powder a) 75 g, 1:5 BPR b) 50 g, 1:3 BPR

In the 75 g pure Al sample, the Al retained its original morphology, but the effect of the ball milling was evident; the particles showed signs of impact. When the metal

HEBM powder jar containing the 50 g pure Al sample was opened after the 10 cycles, the Al had sintered to itself and to the 304 stainless steel milling balls, see Figure 13. The Al/ B_4C sample did not undergo this anomaly likely due to the high temperature resistance of the B_4C or the hard B_4C powder particles breaking apart similar Al sintering.

Figure 13. Aluminum sintered stainless steel milling ball (left) and original milling ball (right)

To dissipate heat within the milling jar and prevent sintering, the HEBM machine was opened between each cycle to circulate air and the milling jars were opened after the fifth cycle to allow the powder additional air cooling. To maximize the amount of powder being mixed during each HEBM run, and to minimize the momentum imparted onto the milling balls, the final parameters recorded in Table 4 were chosen.

Table 4. HEBM Final Parameters

Mass of Powder	Milling Media	Containment	BPR	Run Rest Cycle	Cycles
60 g	3 mm 504 SS Balls	SS Jar	1:5	5 min on 5 min off	10

C. COLD SPRAYING

The four compositions were mixed via HEBM to produce at least 120 g of each composition. The powders were then transferred to glass, non-reactive containers and placed into a 75°C oven for at least 12 hours to dry out any additional moisture before cold spraying.

Before spraying the cold spray samples, the Mg bars were lightly sanded with 800 grit grinding disks at 200 RPM to remove any oxidation from the surface. After sanding, the bars were cleaned with ethanol and dried under a heat gun. Cold spray literature varies in recommendations to prepare the substrate via some variation of grit blasting or not to prepare the substrate surface [11]. Due to Mg not being an extremely hard metal, it was determined that the surface did not need to be prepped as particles would adhere to the surface more easily. On average, substrates prior to spraying measured 153.0 x 22.5 x 9.4 mm and 153.0 x 22.5 x 6.2 mm. The thinner set of substrates were sprayed exclusively for tensile testing.

The machine utilized to cold spray the samples was a Centerline Supersonic Spray Technologies division (SST) Series P Spray Machine, with an X-Feeder, and a Series P Automatic Spray Gun; He was chosen as the carrier gas. The nozzle installed on the cold spray system was a polymer nozzle. Initially, all samples were cold sprayed using the parameters recorded in Table 5. Due to poor deposition efficiencies and inconsistent coating thickness, the Al/BNNT and the Al/B_4C/BNNT powders had to be resprayed with alternate parameters. The final Al/B_4C/BNNT parameters are recorded in Table 6. The Al/BNNT coating continued to have coating thickness problems, so spray trials were

conducted to determine the optimum parameters. The spray trial parameters are recorded in Table 7 with the final spray parameters italicized.

Table 5. Final Al and Al/B_4C Coating Spray Parameters

Feed Rate	Nozzle Temp.	Gas Pressure	Traverse Speed	Stand-off Distance	Line Spacing
8.4 g/min	305ºC	1.2 MPa (175 psi)	40 mm/s	12.7 mm (0.5 in)	1 mm

Table 6. Final Al/B_4C/BNNT Coating Spray Parameters

Feed Rate	Nozzle Temp.	Gas Pressure	Traverse Speed	Stand-off Distance	Line Spacing
18 g/min	305ºC	1.2 MPa (175 psi)	40 mm/s	12.7 mm (0.5 in)	1 mm

Table 7. Spray Trial and *Final* Al/BNNT Coating Spray Parameters

Feed Rate	Nozzle Temp.	Gas Pressure	Traverse Speed	Stand-off Distance	Line Spacing
18 g/min	305ºC	1.2 MPa (175 psi)	40 mm/s	12.7 mm (0.5 in)	1 mm
18 g/min	305 ºC	1.2 MPa (175 psi)	20 mm/s	12.7 mm (0.5 in)	0.5 mm
18 g/min	305 ºC	1.2 MPa (175 psi)	20 mm/s	12.7 mm (0.5 in)	1 mm
18 g/min	*305 ºC*	*1.2 MPa (175 psi)*	*15 mm/s*	*12.7 mm (0.5 in)*	*1 mm*
18 g/min	305 ºC	1.2 MPa (175 psi)	10 mm/s	12.7 mm (0.5 in)	0.5 mm
18 g/min	305 ºC	1.2 MPa (175 psi)	10 mm/s	12.7 mm (0.5 in)	1 mm

Figure 14 shows the visual results from the Al/BNNT spray trials. Visually the results are similar, so the optical microscope was used to inspect the porosity and coating thickness of the samples. The middle sample in Figure 14 is the sample that showed the least porosity and most consistent coating thickness.

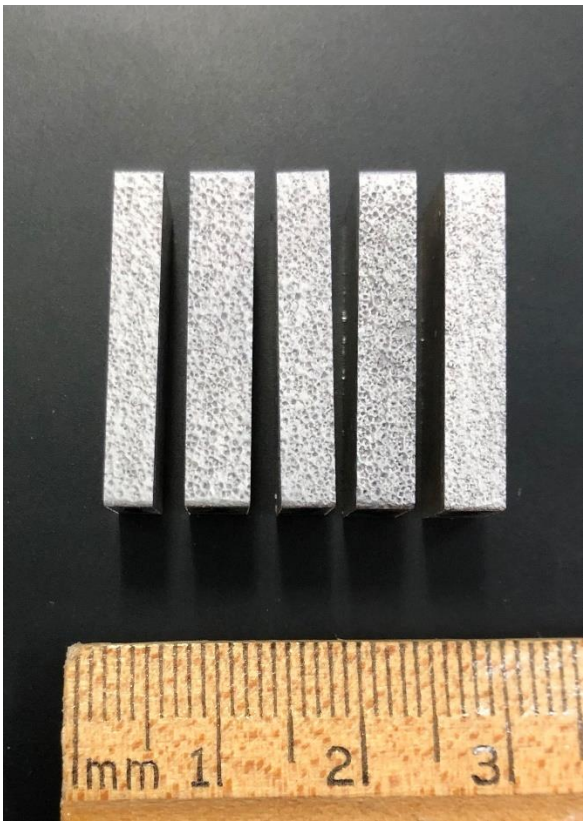

Figure 14. Sectioned samples from aluminum and BNNT spray trials

D. SAMPLE PREPARATION

Many mechanical and microscopy techniques require the cold spray samples be prepared in a polished epoxy cylinder, called a "puck," to ensure that these techniques produce consistent, replicable results. Post cold spraying, each cold sprayed piece was cross-sectioned perpendicular to the coating using a Struers Secotom-20 and hot mounted into a non-conductive epoxy puck using a Struers CitoPress-10. All epoxy pucks were mounted according to the manufacturer's instructions. An example of an unpolished puck can be seen in Figure 15.

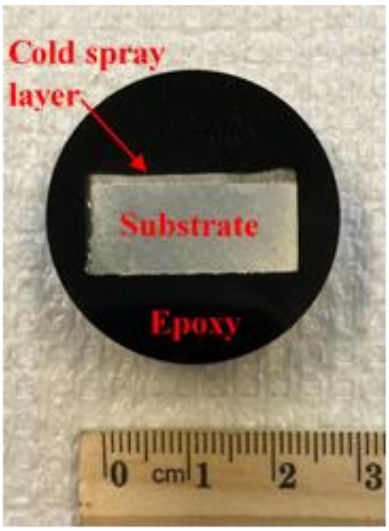

Figure 15. Example of unpolished puck used for testing and characterization

Even when alloyed, Mg is a soft metal that is susceptible to corrosion. Use of a systematic automatic polishing machine left scratches, an uneven surface, and corrosion on mounted cross sections. Instead, the pucks were individually hand ground and polished to a mirror finish with minimal (if any) scratches. The grinding and polishing parameters are recorded in Table 8. Times are approximate based off each puck's progression during the process when viewed under an optical microscope. Of note, the main goal of the polishing was to achieve a mirror finish without large scratches on the Al matrix coatings, the Mg substrate's characteristics make achieving this same finish extremely difficult.

Table 8. Grinding and Polishing Parameters

Step	Grit/Solution	Time (min)	RPM
1	320	5	250
2	500	5-10	250
3	800	10-15	250
4	1200	10-15	250
5	1 μm Alumina*	≥30	250

*Details on step 5 appear in the following text.

Step 5 in Table 8 required a set of trials due to the sensitivity of the Mg substrate. Two different brands of 1 μm diamond water-based suspensions and a 1 μm alumina water-based suspension were utilized to polish the pucks to the final mirror finish. During the polishing step, water is used to wash away the suspension from the puck's surface. All three 1 μm water-based suspensions caused severe corrosion on the Mg substrate which migrated into the cold spray coatings. This corrosion left a chalky white or orange coating that could be removed from the puck face only by re-grinding. To prevent this corrosion from occurring on the puck's face, water was avoided. A polishing pad was moistened with methanol and then sprinkled with Buehler MicroPolish II Alumina 1 μm powder. The polishing pad was then spun at 250 RPM and light pressure was applied to the puck. The powder was applied to the pad every 5 minutes for the first 20 minutes and the methanol was sprayed onto the pad every 2–3 minutes to keep it moist. The puck was periodically examined with the naked eye and the optical microscope to confirm the sample was properly polished.

After polishing was complete, half of each sample was etched to provide surface and microstructural contrast. The etchant utilized was Keller's reagent (a mixture of

2.5 vol.% nitric acid, 1.5 vol.% hydrochloric acid, and 1.0 vol.% hydrofluoric acid in water); an appropriate etchant for Al. This etchant quickly and severely corrodes Mg. The etchant will appropriately corrode the Al matrix splats and grain boundaries [42]. A cotton swab was dipped in the etchant, rubbed with pressure onto the puck, and wiped off after 30 seconds. This was repeated at 5 second intervals until the splat boundaries became visible under the optical microscope.

E. SAMPLE STORAGE

Due to Al and Mg being susceptible to oxidation and/or corrosion the samples were carefully stored between microscopy characterization and mechanical testing. The samples were stored in a SECADOR Desiccator at less than 10% relative humidity, or a PELCO 2251 Vacuum Desiccator chamber at approx. 98 kPa vac.

F. MECHANICAL TESTING

1. Nanoindentation

Nanoindentation is a versatile tool that can provide information about material on the nanoscale using the Oliver-Pharr method [43], [44]. The Oliver-Pharr method, which was introduced in 1992, uses the load vs displacement curve of an indentation to determine a material's hardness and elastic modulus. The method improved upon earlier methods by examining the load vs displacement curve as non-linear rather than linear. This improvement allowed for changes in calculations, shape of the indenter, and the depth of the indentation to produce accurate hardness and elastic modulus values [43], [44]. An example schematic of a load vs displacement curve is shown in Figure 16.

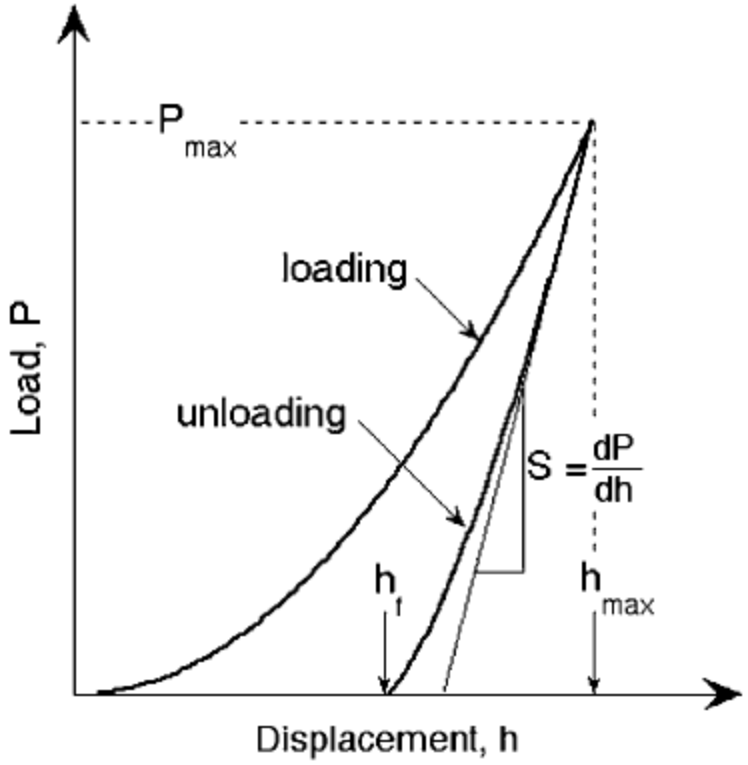

P_{max} is max load, h_{max} is max displacement, h_f is final displacement, and S is stiffness.

Figure 16. Load vs displacement curve used in nanoindentation. Source: [44].

A total of 100 nanoindentations were conducted on each of the four compositions using the Agilent Technologies Nano Indenter G200 and NanoSuite software with a Berkovich indenter. The nanoindenter has two main modes, load and displacement, this experiment utilized load. The parameters for the 100 nanoindentations are recorded in Table 9.

Table 9. Nanoindentation Parameters

% to Unload	Max Load	Peak Hold Time [s]	Time to Load/ Unload [s]	Poisson's Ratio
100	2.942 mN (0.300 gf)	3	10	0.330 [45]

The percent to unload is used for stiffness calculations. The indenter applies a load for 10 seconds until the max load is reached. Then the max load is held for 3 additional seconds and unloaded to a load of zero over 10 seconds. The Poisson's ratio for pure Al is utilized for elastic modulus calculations [45]. The 100 test points were evenly distributed within the cold spray coating. Each point was then checked to verify the test point did not fall on a scratch, pore, or other imperfection.

2. Microhardness

A total of 15 microhardness indentions were conducted on each of the four compositions using the Struers DuraScan Vickers Hardness tester. All indentations were made on the cold spray coating and careful attention was paid to ensure indentations were sufficiently spaced. All tests utilized a Vickers measurement type, HV 0.1 test method (0.9807 N), and a 40x objective lens to inspect the indentations.

3. Adhesion Test

Adhesion tests were conducted on each of the four compositions in accordance with (IAW) American Society for Testing and Materials (ASTM) D4541 standard. The adhesion tests varied from three to four tests per coating composition based off the size and amount of material available on each specimen. The tests were conducted using the Elcometer 510 Model T, an automatic adhesion tester, along with Master Bond EP15ND-2 epoxy. The adhesion tester allows the user to set a constant pull rate and displays the final stress value when the coating fails. Master Bond EP15ND-2 is a one component, heat-cured epoxy with a tensile strength exceeding 82.7 MPa that is primarily used in the ASTM specification C633 [46]. The manufacturer's specifications indicated the epoxy should be cured from 148.9-176.7ºC for 60–90 minutes. The epoxy was cured in a Thermo Scientific Lindberg/ Blue M furnace. Testing parameters are recorded in Table 10.

Table 10. Adhesion Test Parameters

Dolly Size	Pull Rate	Cure Time/Temp	Ambient temp at time of test
10 mm	1.03 MPa/s	90 min @ 174ºC	20ºC

The Master Bond EP15ND-2 epoxy was used over other glues to ensure that the adhesion tests did not fail at the glue-substrate or glue-dolly interface. Instead, the adhesion tests should fail at the substrate (delamination or adhesion failure) or within the cold spray coating itself (cohesive failure). Some failures may also combine aspects of the above three failure modes. After the test, all adhesion failures will be visually inspected and classified by failure mode.

4. Tensile Test

Each cold spray composition was re-sprayed onto a thinner substrate to produce one additional specimen per composition. The four cold sprayed specimens were then cut into two tensile testing specimens for a total of eight tensile testing specimens. The sub-sized specimens were cut to the correct size IAW ASTM E8/E8M - 09 standard. Figure 17 shows the dimensions of the tensile specimen. Note, the tensile specimen shown in Figure 17 does not include the cold spray coating thickness as a dimension.

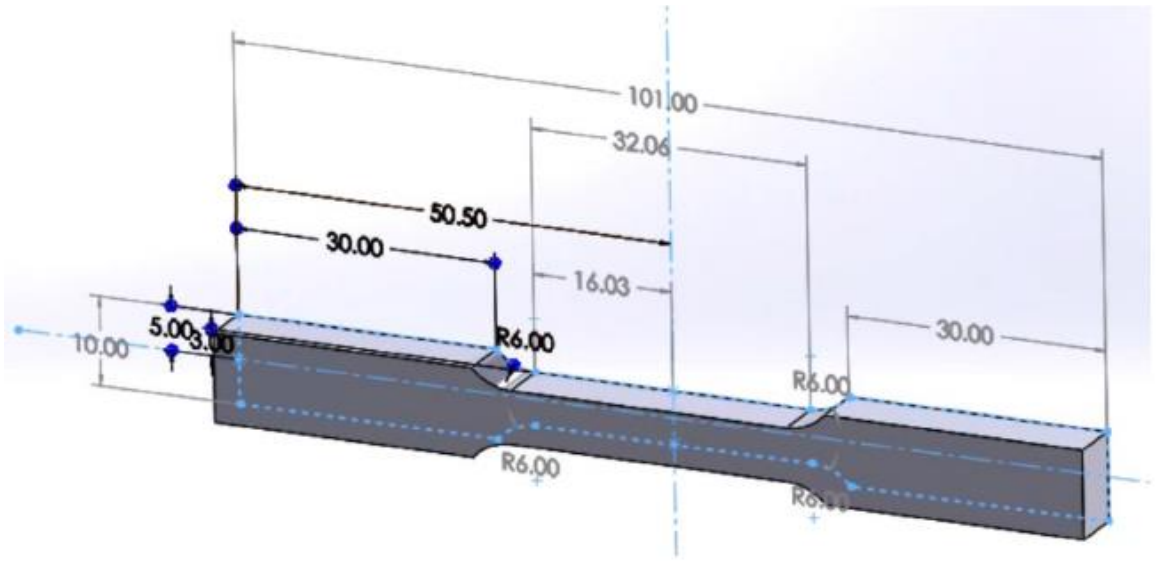

Figure 17. Computer model rendering of tensile test specimen's dimensions in millimeters. Source: [47].

Table 11 shows the average cold spray coating thickness, in millimeters, for each specimen undergoing tensile testing. Attempts were made to reduce the thickness of the Al cold spray coatings, but because of helium shortages, the final sprayed Al coatings were drastically thicker than the other coatings.

Table 11. Average Cold Spray Coating Thickness of Each Tensile Specimen Prior to Testing, in Millimeters

Al #1	**Al #2**	**Al/B_4C #1**	**Al/B_4C #2**	**Al/ BNNT #1**	**Al/ BNNT #2**	**Al/B_4C/ BNNT #1**	**Al/B_4C/ BNNT #2**
1.56	1.55	0.70	0.68	0.52	0.49	0.48	0.47

Tensile tests were conducted on the INSTRON 5982 Universal Testing Instrument. The INSTRON 5982 has modern data acquisition hardware that allows high data acquisition rates during the tests. During each test, the specimens were subjected to a strain rate of 2 mm/min IAW ASTM E8/E8M – 09. All 8 specimens have a gauge length, L_o, of

32.06 mm. The average cross-sectional area of each specimen, considering the average cold spray coating thickness, is shown in Table 12.

Table 12. Average Cross-Sectional Area, A, of Each Tensile Specimen, in Square Millimeters

Al #1	**Al #2**	**Al/B_4C #1**	**Al/B_4C #2**	**Al/ BNNT #1**	**Al/ BNNT #2**	**Al/B_4C/ BNNT #1**	**Al/B_4C/ BNNT #2**
47.34	47.23	41.75	41.63	41.32	41.14	40.58	40.52

The outputs from the INSTRON 5982 are time since test initiation, force [N], and displacement [mm]. Using these parameters and the following equations for strain and stress, the associated stress vs. strain plots can be tabulated. Strain, ε, is given by:

$$\varepsilon = \frac{\Delta L}{L_o} \tag{1}$$

where ΔL is the change in length of tensile specimen, and L_o is the tensile specimen's gauge length.

Stress, σ, is given by:

$$\sigma = \frac{F}{A} \tag{2}$$

where F is the instantaneous force being applied to the tensile specimen and A is the tensile specimen's original cross-sectional area.

G. CHARACTERIZATION

1. Metallurgical Inspection

All samples suspended in the epoxy puck were examined using the Nikon Model Epiphot 200 Microscope with the Nikon Digital Sight DS-2Mv. The Nikon was used for visual inspections at lower magnification to characterize and inspect the overall sample.

The images taken on the Nikon can be magnified between 2.5 and 100 times in both bright and dark field.

Ceramic B_4C and BNNT can cause samples to charge when being examined in the SEM. To prevent this, each sample was sputter coated with 4–5 nm of gold or platinum/ palladium in the Cressington 208HR sputter coater under an argon vacuum. The unetched half was covered in copper tape, allowing a clear path for the electrons around the non-conductive epoxy puck. Samples that were not mounted in an epoxy puck were examined in the SEM by securing the samples with copper tape onto SEM stubs.

The Thermo-Fisher Scientific (FEI) Inspect F50 SEM and the FEI Helios 5 UX SEM were used for examining the samples at high magnifications. Electron beam voltages varying from 2 kV to 20 kV were utilized in conjunction with multiple working distances to optimize images. TEM images were taken with a FEI Tecnai Osiris TEM operating at 200 kV, a 70 μm C2 aperture, and a 50 μm objective aperture.

2. ImageJ

ImageJ is a software program used for image processing and evaluation. The software will be utilized to understand how the ceramic reinforcing particles affect the porosity of the cold spray coatings. Porosity is the percentage of the coating that consists of pores, or voids. In most thermal sprayed coatings, porosity is an undesirable property. Areas of porosity can act as beginning sites for fractures or cracks; negatively affecting the overall strength of the cold spray coating. Porosity was measured within ImageJ using images taken on the SEM and optical microscope.

ImageJ will also be utilized to accurately measure cold spray coating thickness. ImageJ allows the user to adjust measurements to pristinely match the scale in the image. The measurement tool can then measure the coating thickness at multiple locations to within a pixel.

3. Deposition Efficiency

As mentioned in Chapter III, Section C, “Cold Spraying,” there were variances in each compositions cold spray parameters due to the ultimate thickness of the cold spray

coating. By observation only, increasing the vol.% of ceramic reinforcements in the Al matrix seemed to drastically decrease the deposition efficiency. This could be qualitatively seen by observing the difference in the final cold spray coating thicknesses.

The deposition efficiency was measured during the cold spraying of each tensile test specimen. An additional 10% was added to the calculated results. This 10% takes into account overspray, powder that remains in the cold spray lines post cold spraying, and powder loss during transfer between canisters. The deposition efficiency, *DE %*, is given by:

$$DE\ \% = \frac{Substrate\ Mass_F - Substrate\ Mass_I}{Powder\ Mass_I - Powder\ Mass_F} * 100 \quad (3)$$

where $Substrate\ Mass_F$ is the final substrate mass including the cold spray coating, $Substrate\ Mass_I$ is the uncoated substrate mass, $Powder\ Mass_I$ is the mass of the powder before spraying, and $Powder\ Mass_F$ is the mass of the remaining powder.

THIS PAGE INTENTIONALLY LEFT BLANK

IV. RESULTS AND DISCUSSION

A. MIXED POWDER CHARACTERIZATION

The four powder compositions manufactured via HEBM were examined under the SEM. Each composition was imaged and analyzed to ensure the Al powders were not flattened, ceramic reinforcing particles were distributed throughout the matrix, and ceramic reinforcing particles were not over agglomerated.

1. Aluminum Powder

The Al powder post HEBM is shown in Figure 18. The 1:5 BPR kept the Al morphology similar to that of the Al powder received from the manufacturer seen in Figure 7. None of the Al appears to be flattened or overly deformed.

Figure 18. Aluminum powder post HEBM

2. Aluminum and B_4C Powder

Figure 19 shows the Al and B_4C powder post HEBM. The B_4C can be identified, even at low magnifications. The B_4C is dispersed throughout the matrix and is on the surface of the Al powder. Where there are agglomerations of the ceramic, the agglomerations occur primarily where the B_4C is causing the Al powder to adhere to each other. The B_4C is acting like glue.

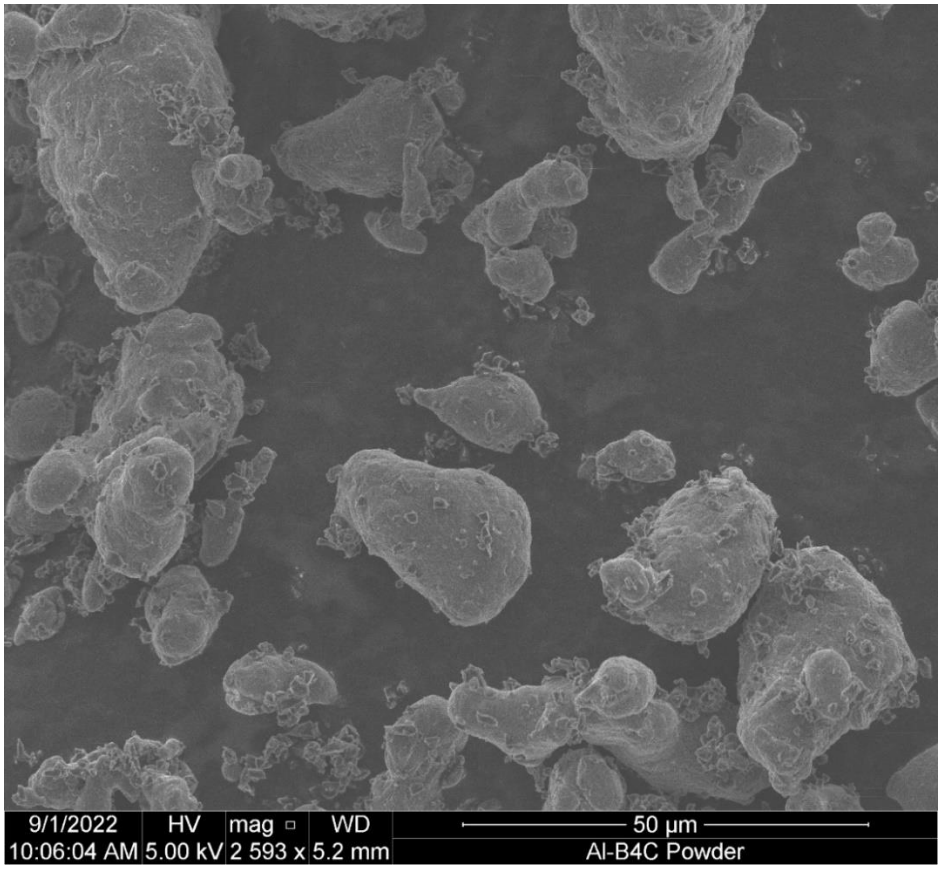

Figure 19. Aluminum and B_4C powder post HEBM

Figure 20 is a magnified image of the Al and B_4C powder; selected B_4C or agglomerated B_4C are circled in red. Here, three pieces of Al powder are being bridged by B_4C. The B_4C is also dispersed on the surface of the Al particles. Prior to cold spraying it is ideal to have a good distribution of reinforcing ceramics. When the Al is cold sprayed and forms a splat, the reinforcing particles on the surface of the Al will be trapped in the

splat boundaries. Ideally, the B_4C trapped in the splat boundary will act as an anchor during mechanical testing.

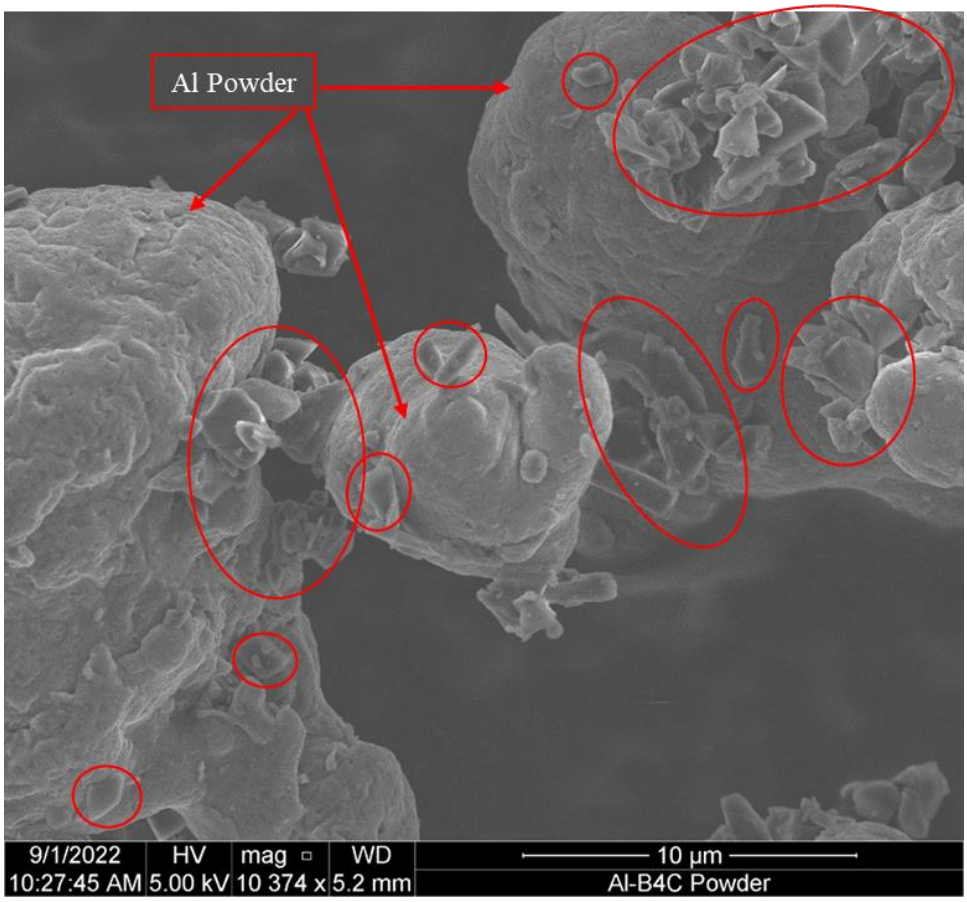

Figure 20. Magnified aluminum and B_4C SEM image

3. Aluminum and BNNT Powder

Figure 21 is a low magnification image of the Al and BNNT powder. Again, the Al generally retains the original shape, although the powder does look more "beaten up" then the other images. This could possibly be due to the presence of the BNNT during the HEBM process.

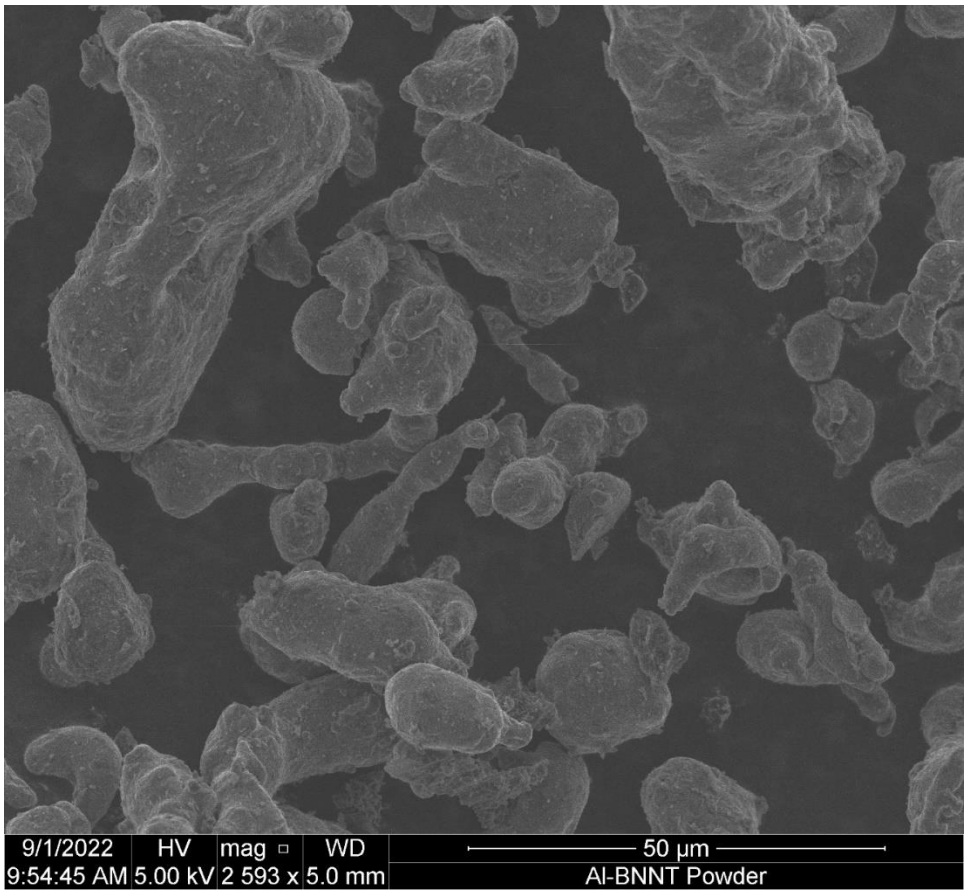

Figure 21. Aluminum and BNNT powder post HEBM

Distribution of the BNNTs throughout the Al matrix needs to be verified. Due to their small dimensions, single BNNTs are difficult to identify using any microscopy technique, including an SEM. Often, it is much easier to find agglomerations of BNNTs and then search for single BNNTs in the vicinity.

Figure 22a shows a small agglomeration of BNNTs, circled in red. On the Al particle there appears to be additional "chopped up" BNNTs scattered throughout the surface. An intact BNNT is preferred, but any BNNT presence on the Al particle is good. Figure 22b shows a magnified image of the agglomeration. Utilizing ImageJ the agglomeration has a maximum thickness of 520 nm, a minimum thickness of 280 nm, and a length of 2.4 µm. The end of the agglomeration in Figure 22b appears to have some "spikes" measuring around 40 nm in thickness. This indicates the nanotubes are likely agglomerated length wise.

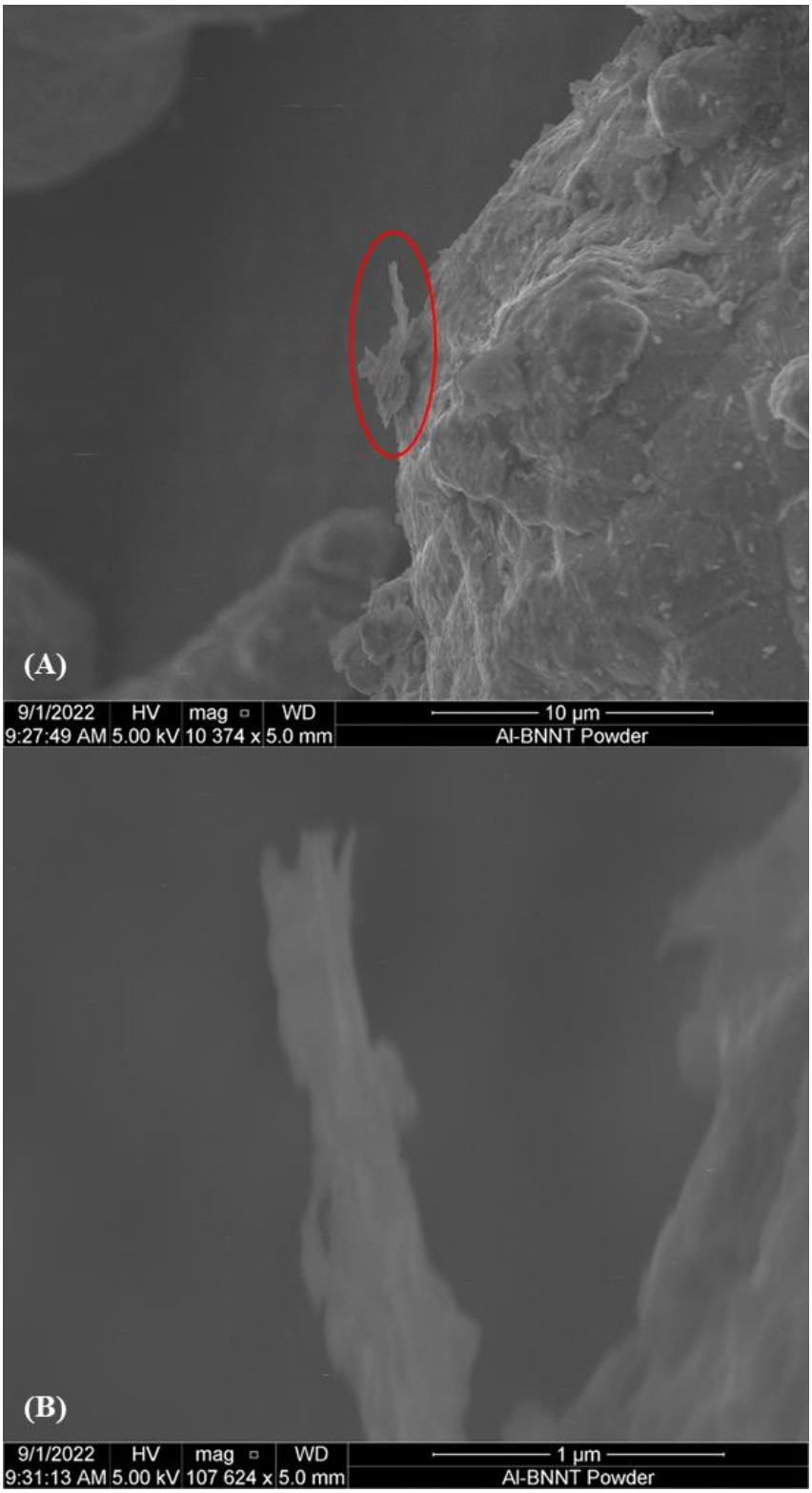

Figure 22. a) BNNTs on the aluminum matrix b) magnified image of BNNTs

Figure 23 shows two other agglomerations of BNNTs, circled in red. The agglomeration near the center of the figure has a maximum thickness of 670 nm, a minimum thickness of 280 nm, and a length of 4.2 µm. BNNT agglomerations often have a "fluffy" appearance, as seen in Figure 21 and Figure 22. Other than the agglomerations circled in red in Figure 23, there are other small BNNT agglomerations on the surfaces of the Al powder.

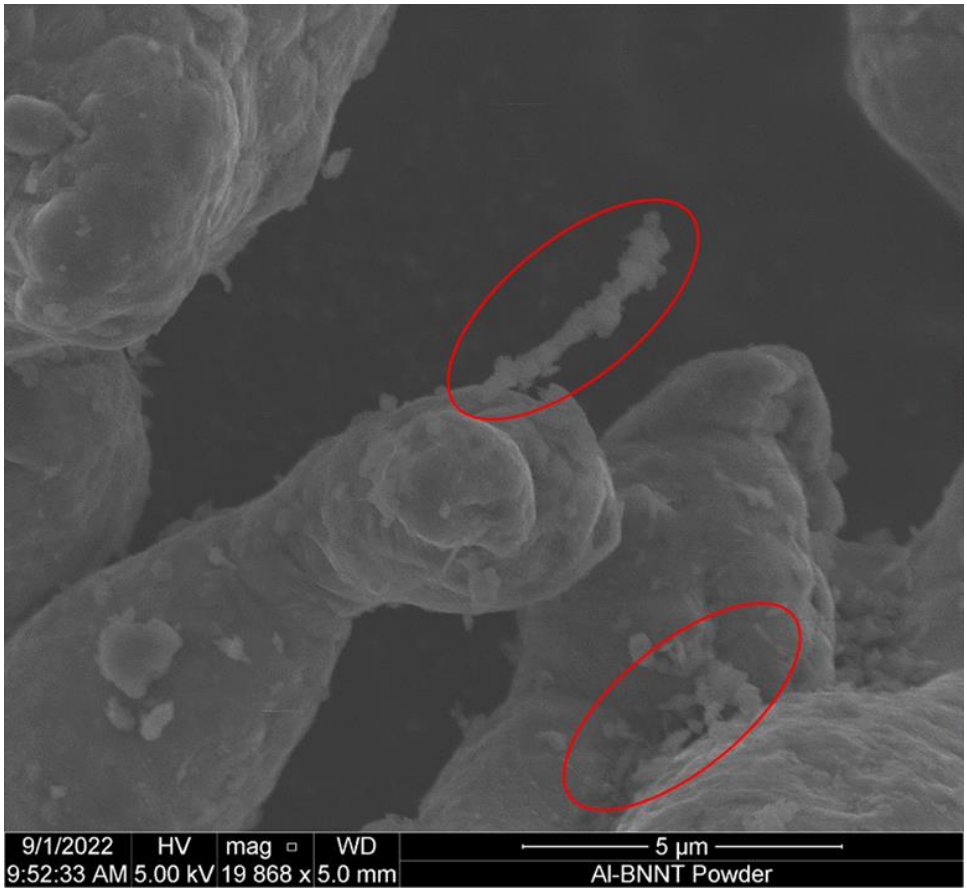

Figure 23. Agglomeration of BNNTs on aluminum matrix

Figure 24 is used to show what a large agglomeration of BNNTs will look like in an SEM image. The particles circled in red have a much different surface texture than the nearby Al particles; rather than being relatively smooth, these agglomerations have rough, inconsistent surface features. This is either a massive agglomeration of BNNTs or the BNNTs have agglomerated and encompassed an entire Al particle. Another indication that

this is an agglomeration of BNNTs and not just a very deformed Al particle is the charging that occurs when focusing the SEM's electron beam on the particle. Charging is a common problem when imaging insulating materials (like BNNT) in an SEM.

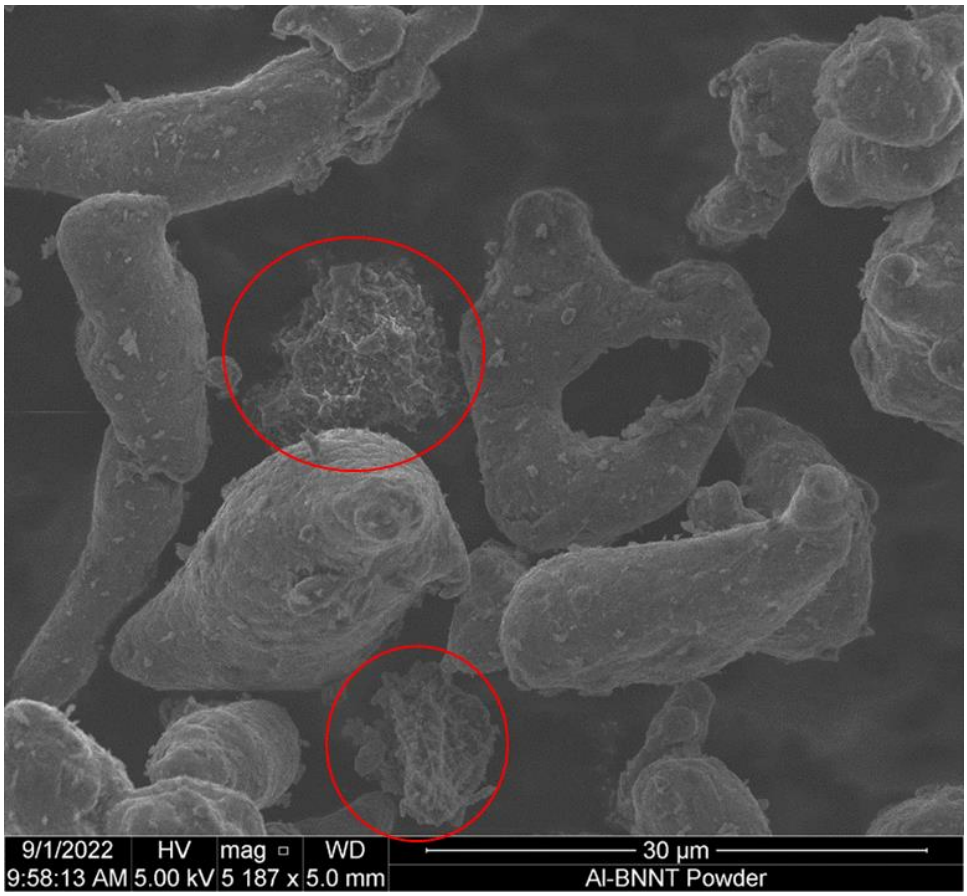

Figure 24. Large BNNT agglomerations compared to aluminum powder

4. Aluminum, B_4C and BNNT Powder

Figure 25 is an overview image of the powder that contains Al with B_4C, and BNNT as the ceramic reinforcements. Here the Al powder has the same general morphology as the original Al powder.

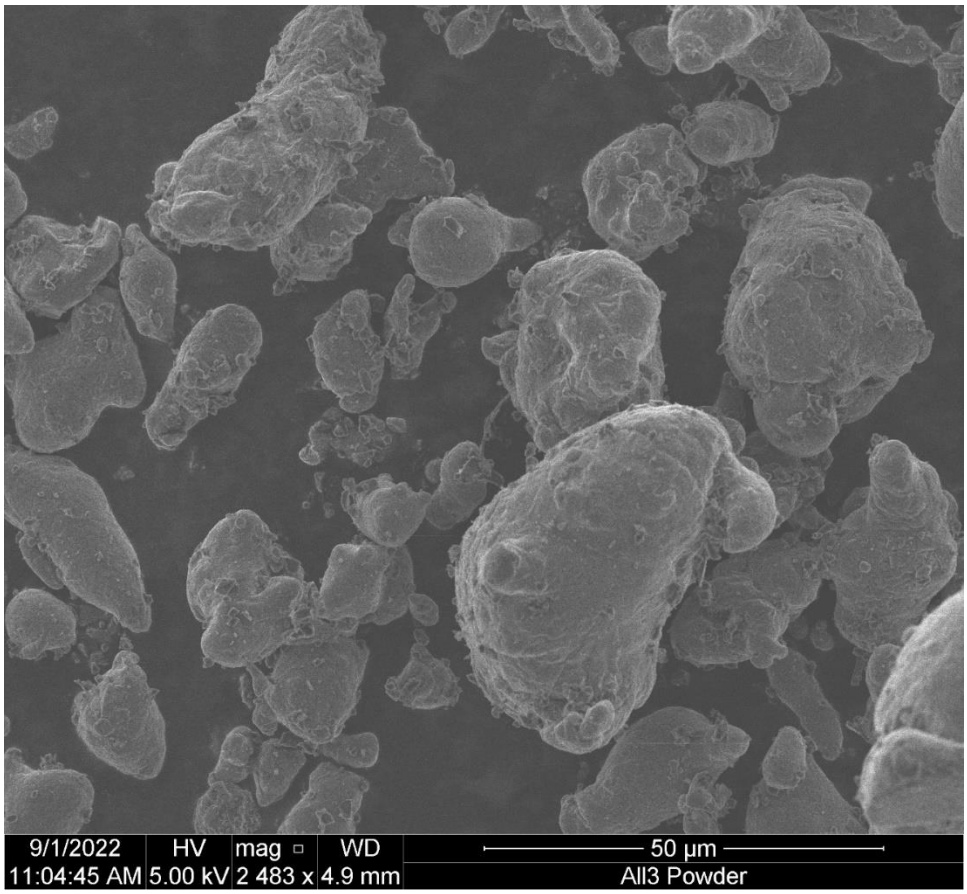

Figure 25. Aluminum, B_4C, and BNNT powder post HEBM

Figure 26a is an overview image showing both the B_4C, and the BNNT dispersed throughout the Al particles; selected B_4C are circled in green and selected BNNT are circled in red. Both reinforcements appear to be dispersed on the Al. The right half features two B_4C stacked on top of the Al with a small agglomeration of BNNTs on top of the B_4C. Figure 26b is a magnified image of selected ceramics. The BNNT that is hanging off the Al particle at the center of the figure measures approximated 100 nm in thickness and 1.2 µm in length; the thickness is slightly larger than the manufacturer's nominal nanotube diameter of 60 nm.

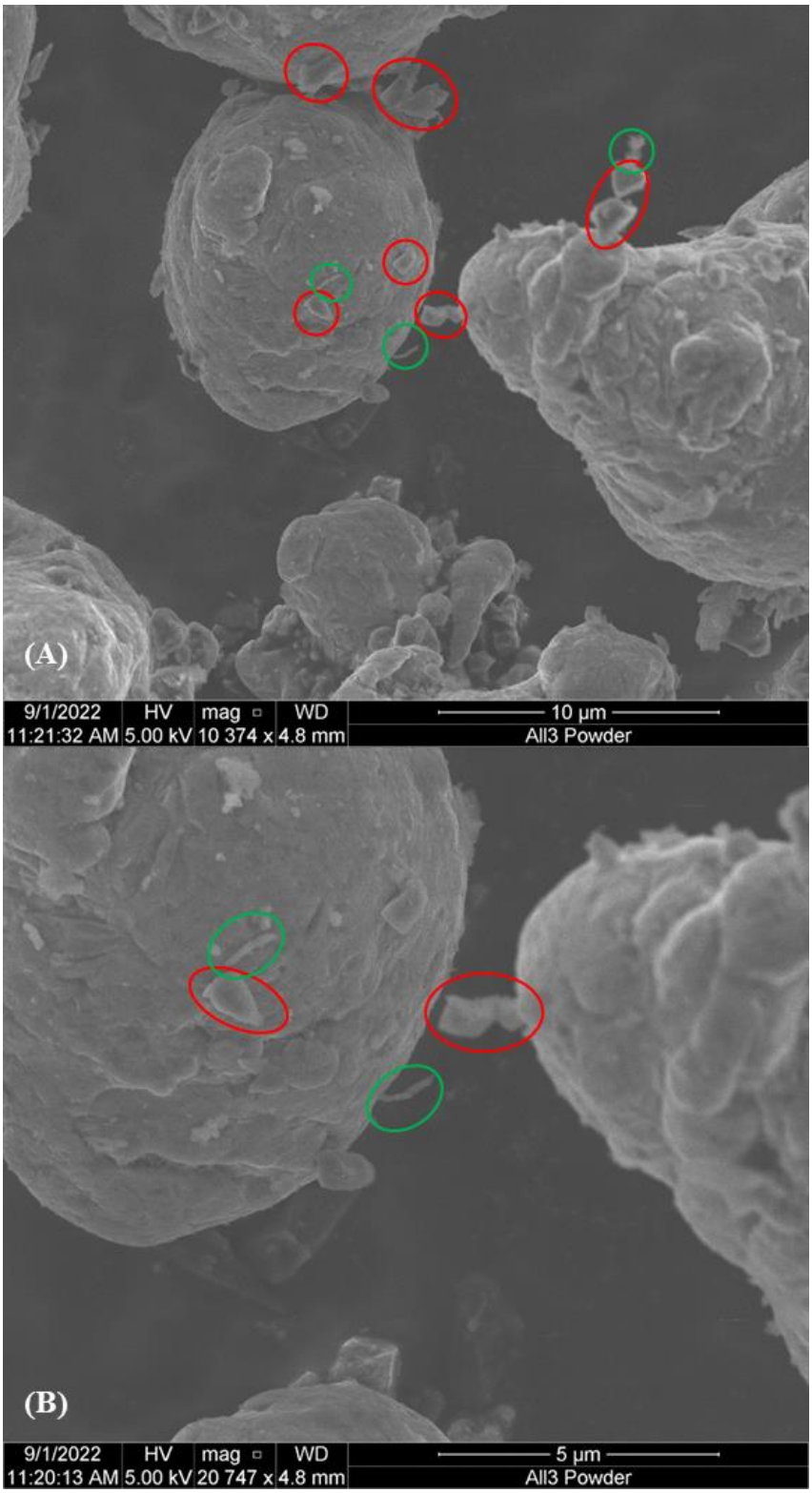

Figure 26. a) dispersed BNNTs and B_4C on aluminum b) magnified image of BNNTs and B_4C

Figure 27a and 27b display a feature that is connecting two Al particles. The feature measures from 290–560 nm thick and 10.88 μm in length. At higher magnifications the feature does take on the puffy look of an agglomeration of nanotubes. This agglomeration includes a B_4C attached at about half of the length. The nanotubes appear to be "bridging" the gap between the two Al powders. This is less common in powder but more common when microscopy is conducted after mechanical tests have been completed on a cold spray coating. Often the ceramic reinforcements improve the adhesion of splats and fills in voids at the splat boundaries.

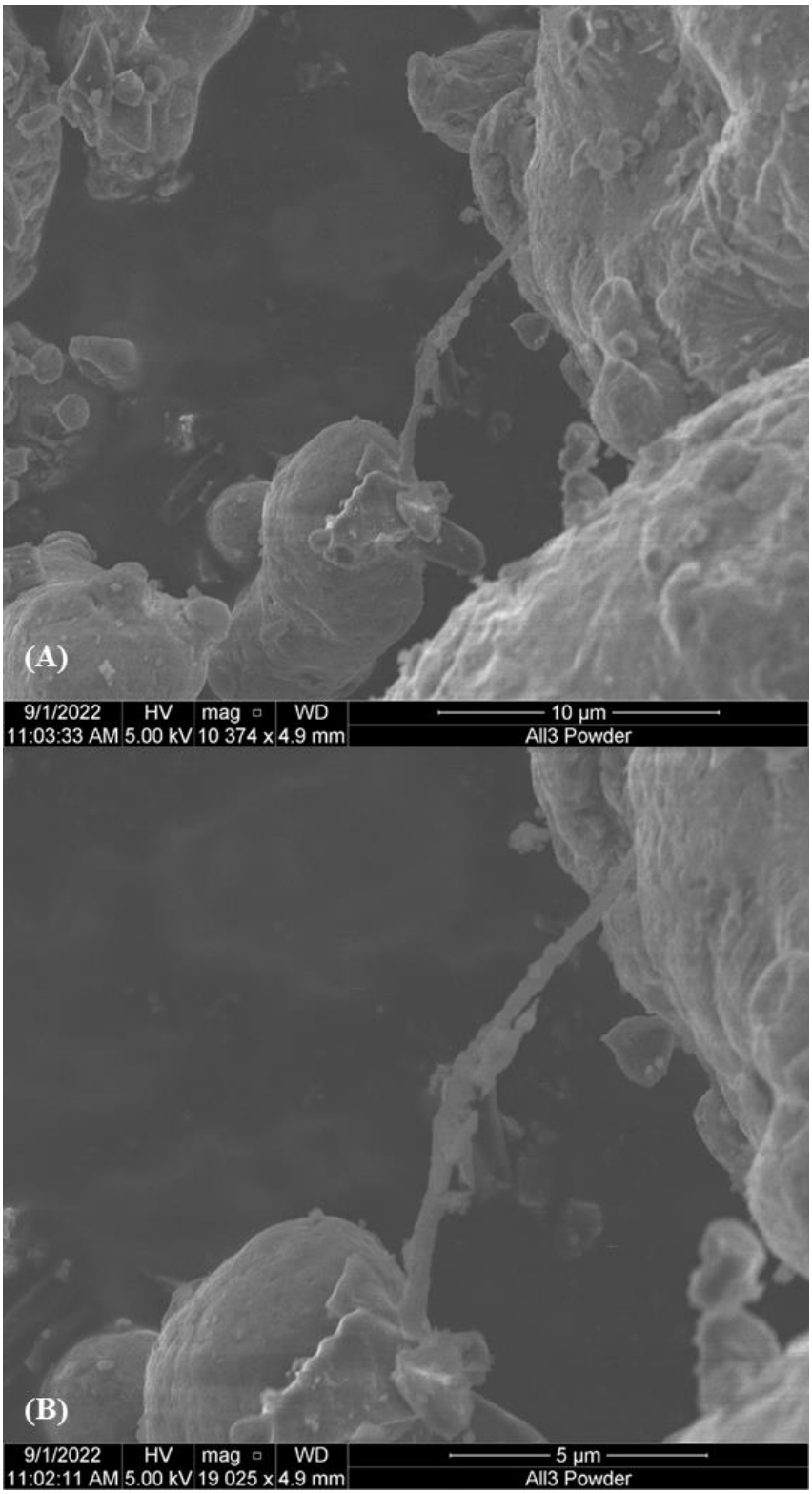

Figure 27. a) large feature connecting aluminum powder b) magnified image of feature

Overall, using the HEBM parameters outlined in Chapter III, Section B, "High Energy Ball Milling," proved to be effective and efficient in distributing the ceramic reinforcements throughout the Al matrix without overly deteriorating the matrix. Agglomerations of both B_4C and BNNTs do still exist, but these agglomerations seem to not dominate the powder features.

B. SAMPLE CHARACTERIZATION

1. Visual Inspection

Post cold spraying, the cold spray specimens were visually inspected. Figure 28 shows the four compositions. As previously alluded too, the Al/BNNT composition stood out from the others. This composition looks porous or ridged compared to the other three samples. This composition also has an inconsistent thickness that is noticeably thin compared to the Al and the Al/B_4C coating. The Al and the Al/B_4C coatings are thick and appear to be smoother and more uniform than the other two coatings. Both the samples containing B_4C are darker, this is because before milling, the B_4C powder is a rich black color. The composite coating containing all three powders has a smooth appearance, is thinner than the Al and Al/B_4C coatings, and slightly thicker than the Al/BNNT coating.

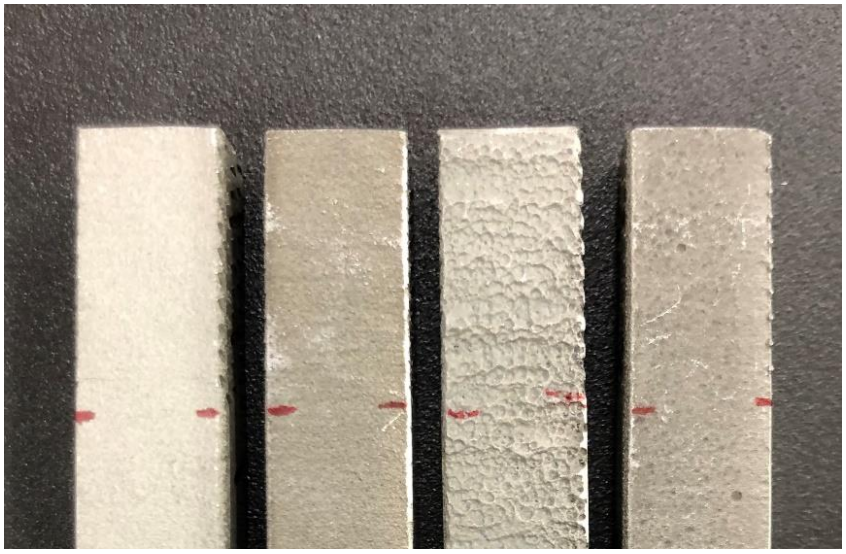

Figure 28. Top-down view of cold spray compositions. Left to right: Al, Al/B_4C, Al/BNNT, Al/B_4C/BNNT

2. Optical Inspection

Figure 29 shows the final optical images taken for each composition before etching. The Al/BNNT coating has an inconsistent thickness when compared to the other compositions; in the next section this thickness will be quantified. As with the visual inspection, this coating appears to be much more porous than the other coatings. This appearance of porosity could be a combination of pores and leftover alumina from the polishing step. Etching this coating and examining it in the SEM will give a better indication of this composition's porosity. The cold spray coatings that contain B_4C appear darker than the other coatings. The Al/B_4C composition is the darkest, which corresponds to it having the largest vol.% of B_4C. The Al cold spray coating appears to have small black spots with comet tails. This is leftover alumina from polishing combined with some porosity.

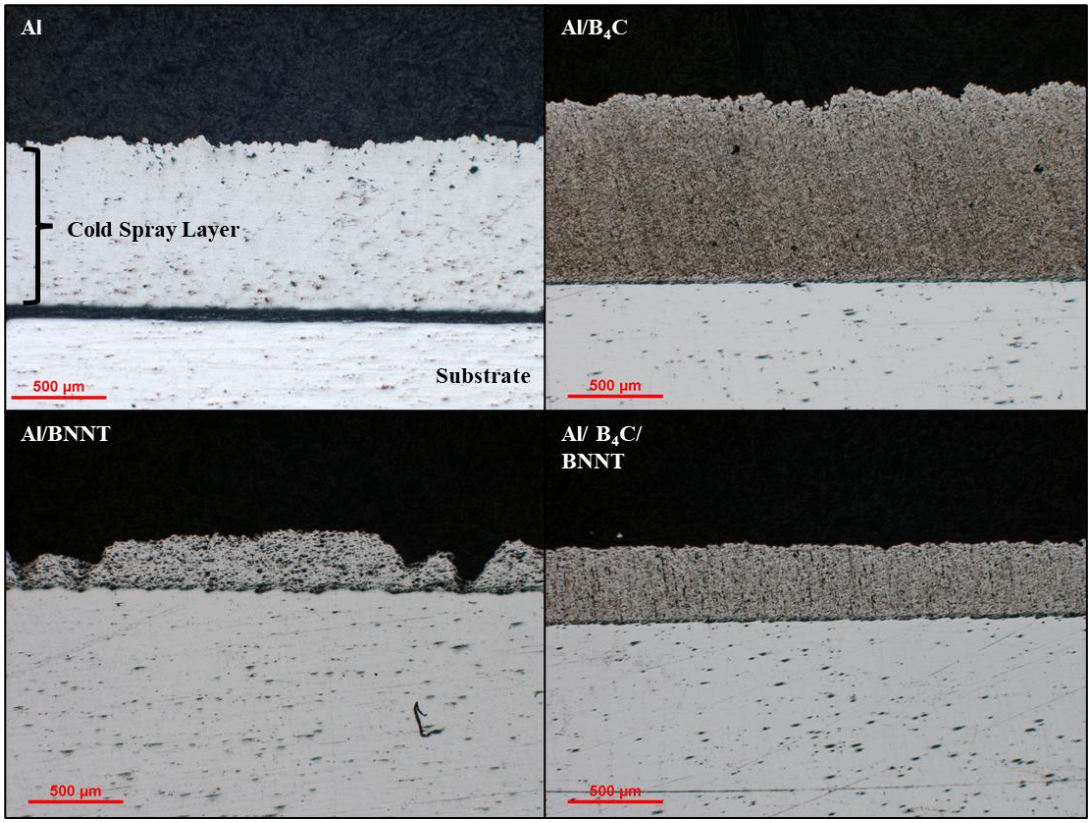

Figure 29. Optical microscope images of all four cold spray coating compositions

The Mg substrate for all four cold spray coatings shows the same characteristics. The substrate shows signs of scratches, left over alumina, and regions where corrosion has occurred. The thick black line between the cold spray coatings and the substrate (most evident in the Al composition) indicates the Mg is being ground away more quickly than the coatings. This mismatch in height becomes increasingly obvious at high magnifications. This study will not include involved examination of the Mg substrate under the SEM or optical microscope.

3. Coating Deposition and Microstructural Characterization

The average coating thicknesses are recorded in Table 13. These thicknesses are accomplished in ImageJ by measuring the polished cross-section images from the optical microscope and SEM. Each composition can be compared to the control group that consists of the pure Al coating. As reinforcements are added, the coating thickness decreases. Most noticeably, when either 2 vol.% or 4 vol.% BNNTs are added, the thickness rapidly decreases. This anomaly may be due to the high surface area and the low mass of the BNNTs, which causes poor flow through the feed lines. After spraying each composition, the powder feed lines were cleared with compressed air to prevent substantial line clogging. The composition that contained only BNNTs noticeably clogged and adhered to the inside of the powder lines at a much greater frequency compared to the other compositions. This could be largely due to the BNNTs agglomerating together. When the vol% of BNNTs was reduced from 4 to 2, the thickness did increase closer to the control thickness and the coating thickness's standard deviation also decreased. This is due to the presence of the 2 vol.% B_4C that are mixed with the 2 vol.% BNNTs. The hard, micron size B_4C break apart the agglomerated BNNTs, thus causing less clogging of the lines and more BNNTs being able to reach the substrate.

Table 13. Average Coating Thickness

Composition	Range	Average Thickness [μm]	Standard Deviation [μm]
Al	974.9-1116.1	1037.3	36.6
Al/B_4C	866.7-949.2	905.3	20.0
Al/BNNT	58.6-438	312.8	98.2
Al/B_4C/BNNT	448.6-568.2	508.9	37.9

Due to the large differences in coating thickness, the deposition efficiency was measured and calculated using (3). The deposition efficiencies are recorded in Table 14. The calculated deposition efficiencies verifies that the addition of BNNT is detrimental to the coating thickness. The addition of B_4C also decreases the deposition efficiency of the cold spray coatings but not to the same extent as the BNNTs.

Table 14. Composition Deposition Efficiency

Composition	Deposition Efficiency [%]
Al	76.8
Al/B_4C	61.0
Al/BNNT	13.0
Al/B_4C/BNNT	18.8

Another measurement that is frequently linked to thickness and deposition efficiency is porosity. From Figures 28 and 29, it was visually evident that greatest porosity occurred in the Al/BNNT coating. To accentuate grains, splat boundaries, and porosity, all compositions were etched. Unfortunately, when etching the samples, the Mg substrate began to severely corrode and adversely affect the imaging of the cold spray coatings. Due to this, the etching was stopped prematurely, and the grains/splat boundaries were not optimally etched for imaging. The porosity of the Al/BNNT was evaluated in ImageJ on one of the few adequately etched regions. For this composition, the porosity was calculated to be 2.65%. A heat treatment is not being performed during this study; thus, porosity calculations do not need to be compared pre and post heat treatment. Ignoring the surface regions with limited coating, the porosity within the Al/BNNT cold spray coating was sufficiently low. Therefore, no other coatings were evaluated for porosity in ImageJ.

Each mounted and polished puck was inspected under the SEM to observe the microstructure, micron/nano size particles, and the distribution of these particles. Figure 30 shows the control sample, pure Al, under the SEM. In Figure 30a, some of the splat boundaries/porosity are visible. These boundaries are the areas that are thin black lines and indents. Figure 30b is a magnified image of one of these regions.

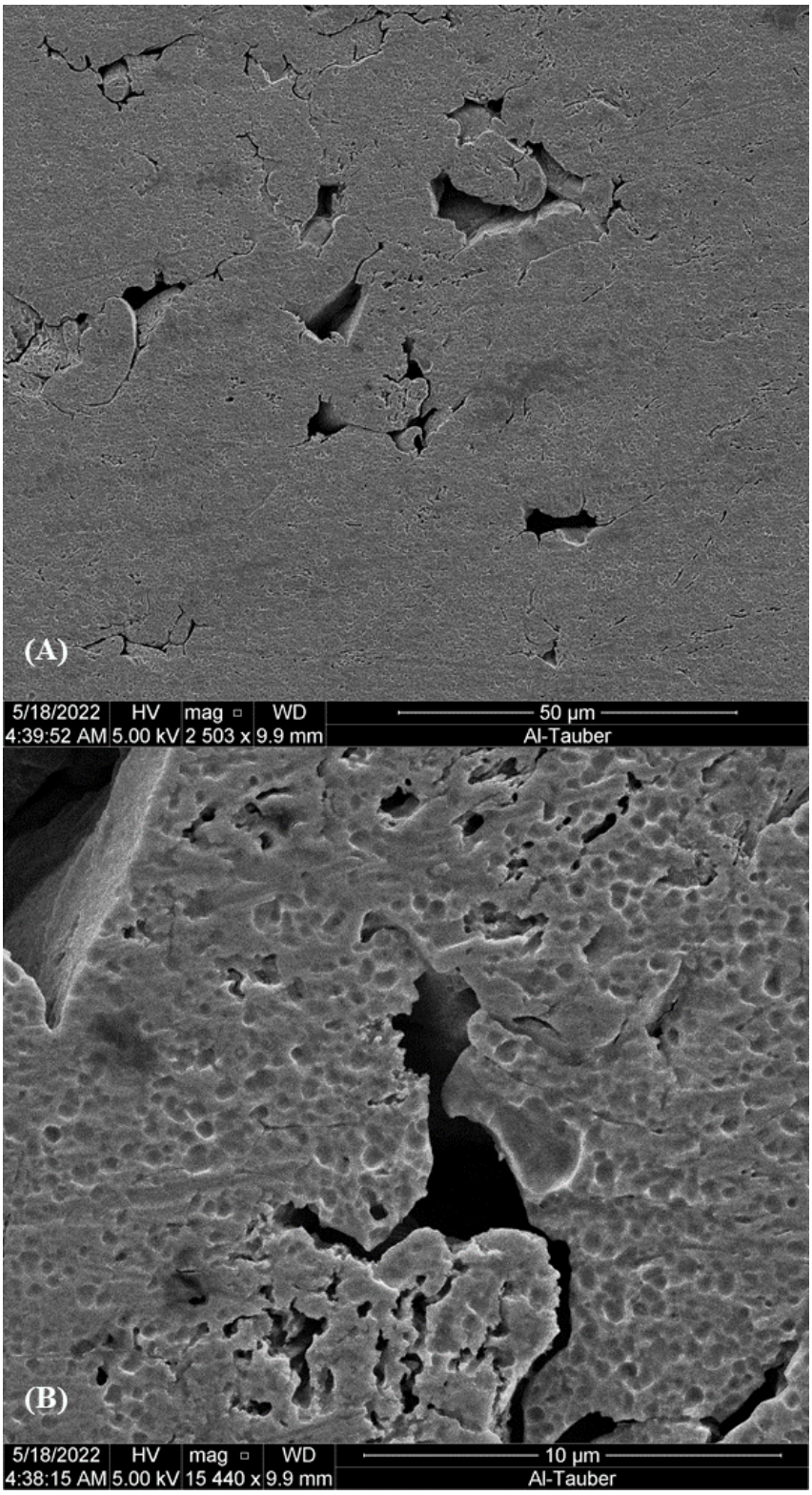

Figure 30. Aluminum cold spray coating a) overview of splat boundaries b) higher magnification image of a splat boundary

Figure 31 is a low magnification SEM image of the Al/B_4C coating. The darker spots are the micron sized B_4C particles or sites where B_4C were ejected during the grinding and polishing of the cross-section. These voids still retain the same general size and shape as the B_4C seen in Figure 9, and the B_4C post HEBM seen in Figure 20. This is expected as B_4C are very hard and durable compared to Al. Additionally, splat boundaries and voids are visible.

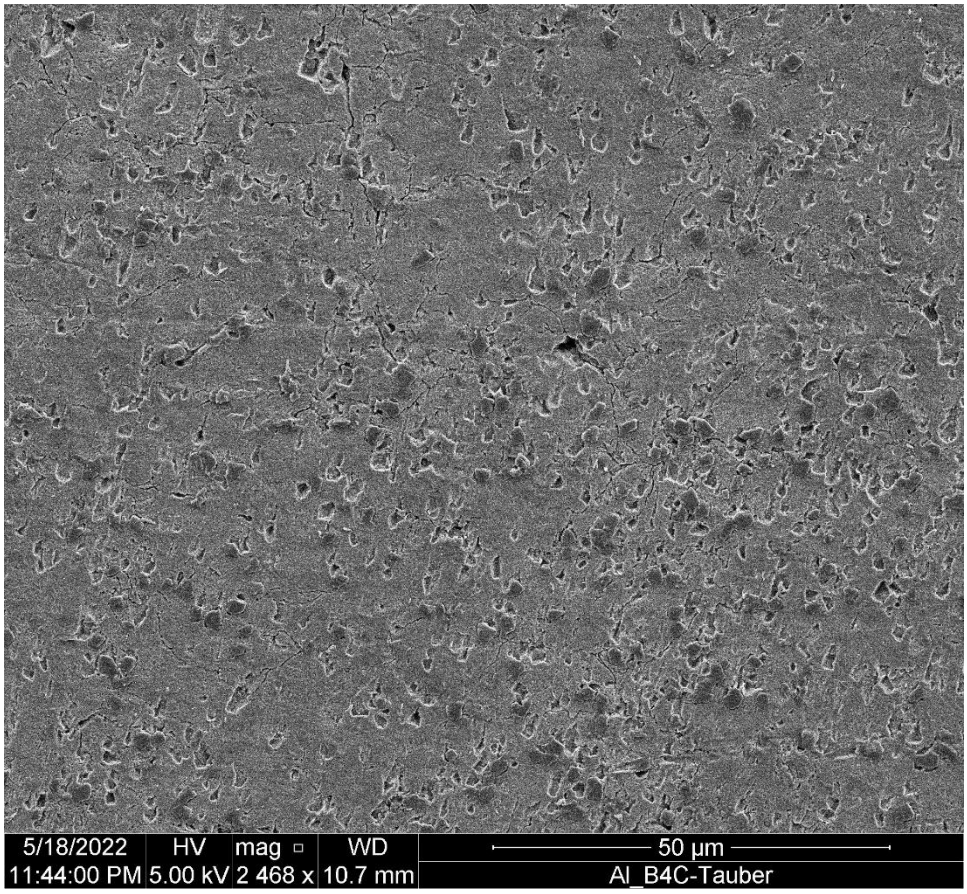

Figure 31. Overview SEM image of the Al/ B_4C composition

The goal of most reinforcing materials is to attach to the surface of the matrix material during the powder manufacturing process. Once the powder is sprayed, the reinforcing material will be found at the splat boundaries. The B_4C was well distributed throughout the Al matrix. In Figure 32a, the 1–3 µm B_4C are easily identifiable, due to their shape and the associated edge effect. Figure 32b is the same as 32a but shows, in red,

the location of the splat boundaries. The splat boundaries are not drawn through the B_4C; instead, where a B_4C is positioned within a splat boundary, the line stops and continues on the other side of the reinforcing particle. By comparing Figures 32a and 32b, it is evident that the B_4C do exist along the splat boundaries. In fact, the overwhelming quantity of visible and easily identifiable B_4C have made impressions and surface defects that make the splat boundaries difficult to identify.

As alluded to earlier in this section, there are many sites where B_4C appear to have been ejected or ripped out of the cold spray coating. Figure 33 shows many examples of this. A few of the ejection sites are highlighted in red, but by observation, there are many more of these sites throughout the image. These are identifiable as ejection sites of B_4C due to the identical shape and size of the remaining craters. Further in Chapter IV, the adhesion strength of the B_4C reinforcement will be measured. It is important to keep in mind the difference in failure mechanism. In the current scenario, where the cutting saw and the grinding wheel are working parallel to the cold spray coating, the applied force (from the cutting or grinding) can be simplified or thought of as acting in shear to the cold spray surface. Again, this will be revisited in later sections. Figure 34 shows a simplified schematic of this process where the portion of the puck resting against the grinding wheel contains the cold spray coating and substrate.

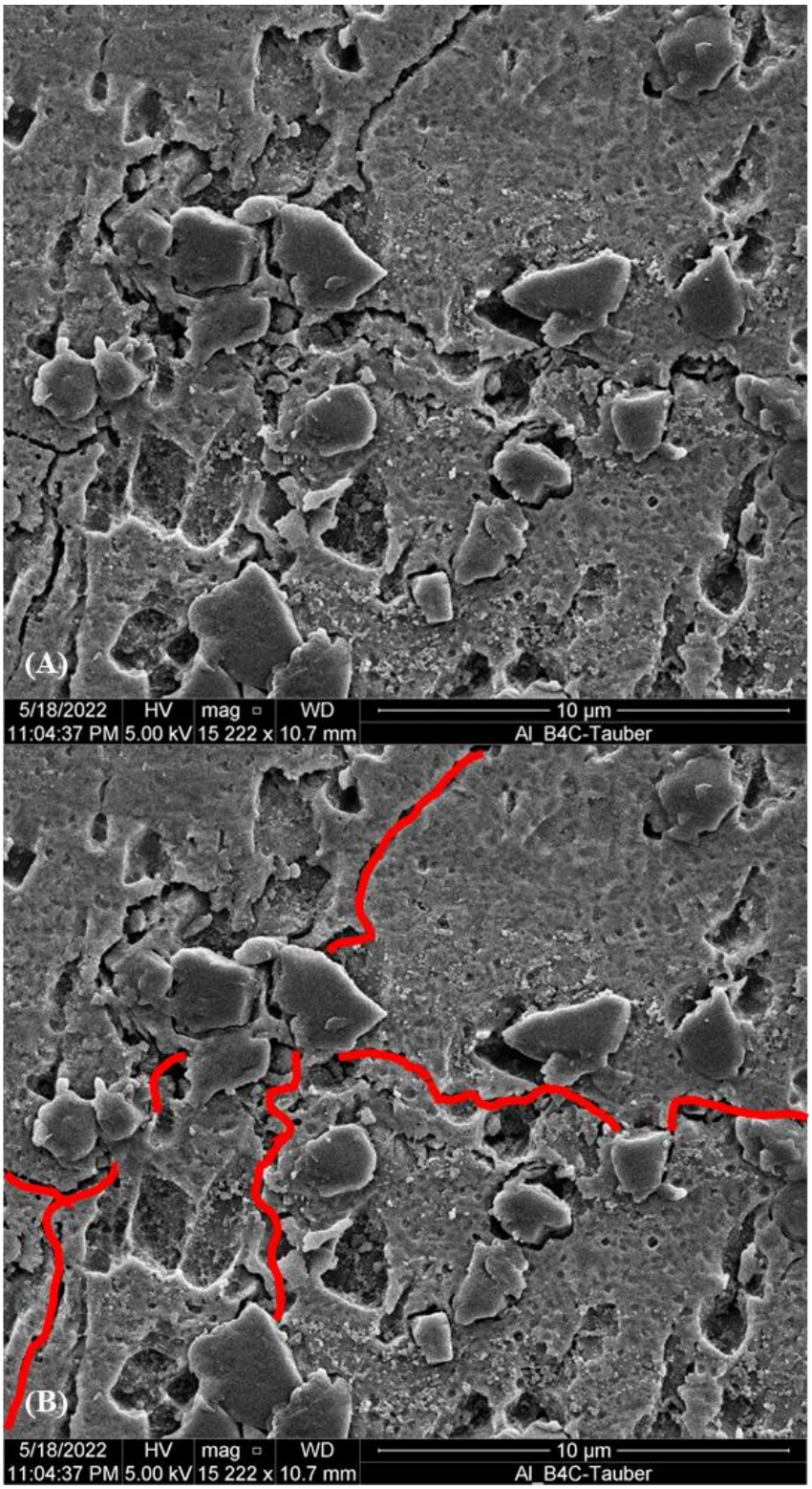

Figure 32. Al/B_4C SEM image a) original image b) image highlighting splat boundaries

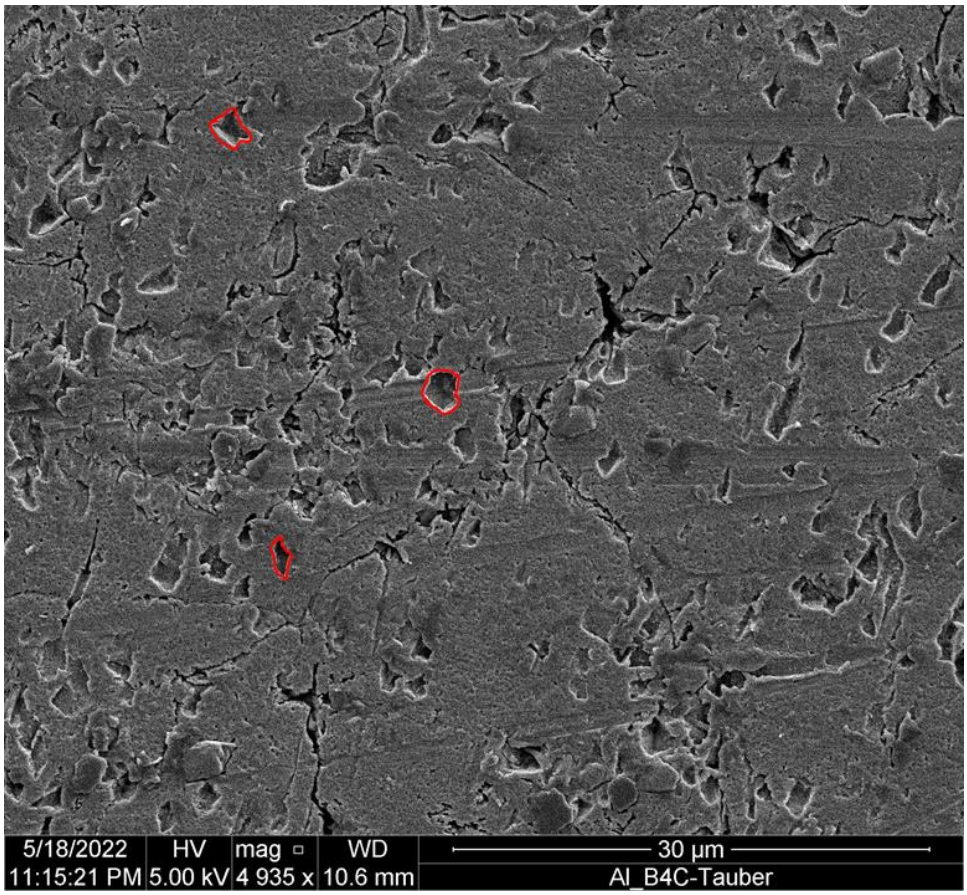

Figure 33. Al/B_4C coating showing B_4C ejection sites

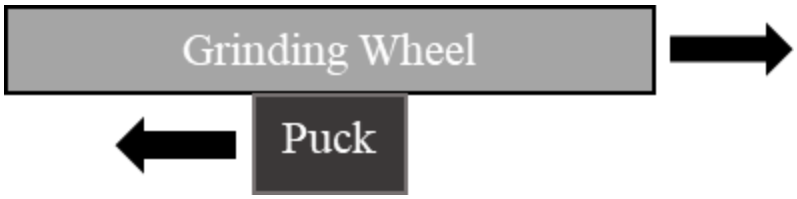

Figure 34. Example of shear force being applied to face of puck

The next cold spray coating to be examined was the Al/BNNT composition. Due to the nature of being a nanoparticle, BNNT is much more difficult to locate. Figure 35a shows an image of a splat boundary and what appears to be a pore. The inside of which is quite rough compared to the surrounding coating surface. Figure 35b shows a magnified image of the splat boundary.

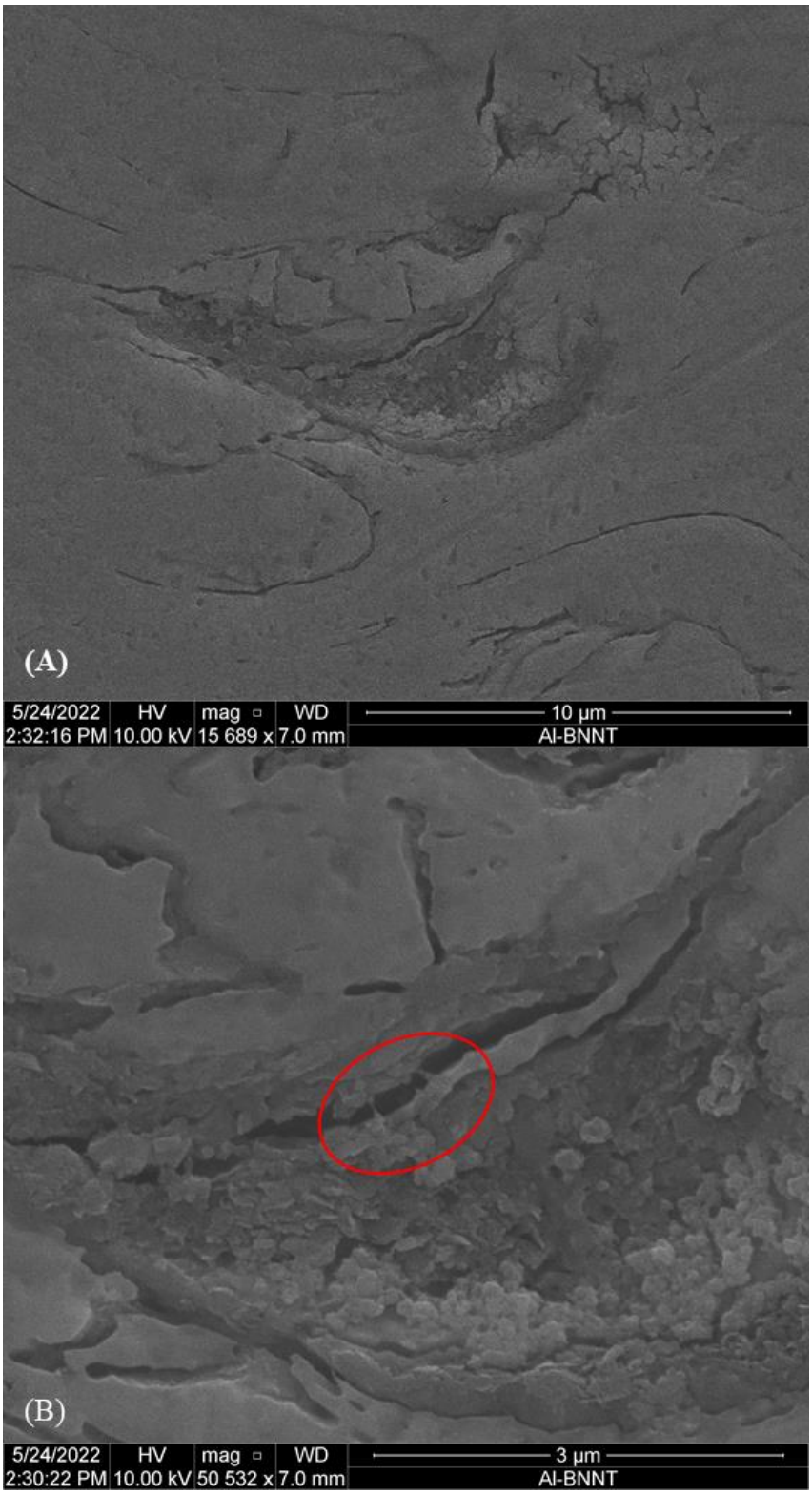

Figure 35. SEM image of Al/BNNT composition a) splat boundary with pore b) magnified image showing possible BNNTs

In Figure 35b, the area inside the pore is extremely coarse. This is not something seen in any of the areas surrounding the pores in the pure Al coating (Figure 30b) and varies from the texture seem in the Al/B_4C coating (Figure 32). This indicates that the texture within the pore is related to the addition of BNNTs. Circled in red in Figure 35b are what appear to be two nanotubes spanning across the splat boundary. Finding the nanotubes proved to be difficult. Most splat boundaries did not have identifiable BNNTs, even at very high magnification. Initially, during examination of the coating, some areas were passed over due to their abnormal surface features. Later, these areas were re-investigated.

Figure 36a and 36b show two examples of these areas; the areas of interest are slightly lighter in contrast to the rest of the cold spray coating. They appear like a spider-web, enveloping large splat boundaries and pores. Some of these feature's span over 30 μm in distance. Upon further inspection, these areas appear to be large webs of BNNTs consisting of both nanotubes and agglomerations of nanotubes. Although agglomerations are not necessarily desired, these features do provide proof that the BNNTs are distributed throughout the matrix and that they span across pores and splat boundaries to ideally increase the resiliency of the coating. When investigating the rest of the coating, away from splats boundaries and pores, this type of web or pattern was not found. This indicates that the webs are most likely not left-over residue from etching, clumps of gold from sputtering, or any other contaminate. Figure 37 shows Figure 36b at higher magnification; single and agglomerated BNNTs located at the splat boundary are circled in red. The circle near the center of the image appears to feature a single nanotube while the circles in the upper right and lower left-hand corners feature small agglomerations.

Although some BNNTs were identified, the lack of BNNTs, when compared to the same vol.% of B_4C, can likely be attributed to a couple of things. First, the HEBM process deforms or chops up many of the BNNTs, making them harder to identify within the coating. Second, the deposition efficiency for this composition is very low. Many of the BNNTs may have been deflected off the substrate during the actual cold spray process or were ejected out of the carrier gas stream while spraying the coating.

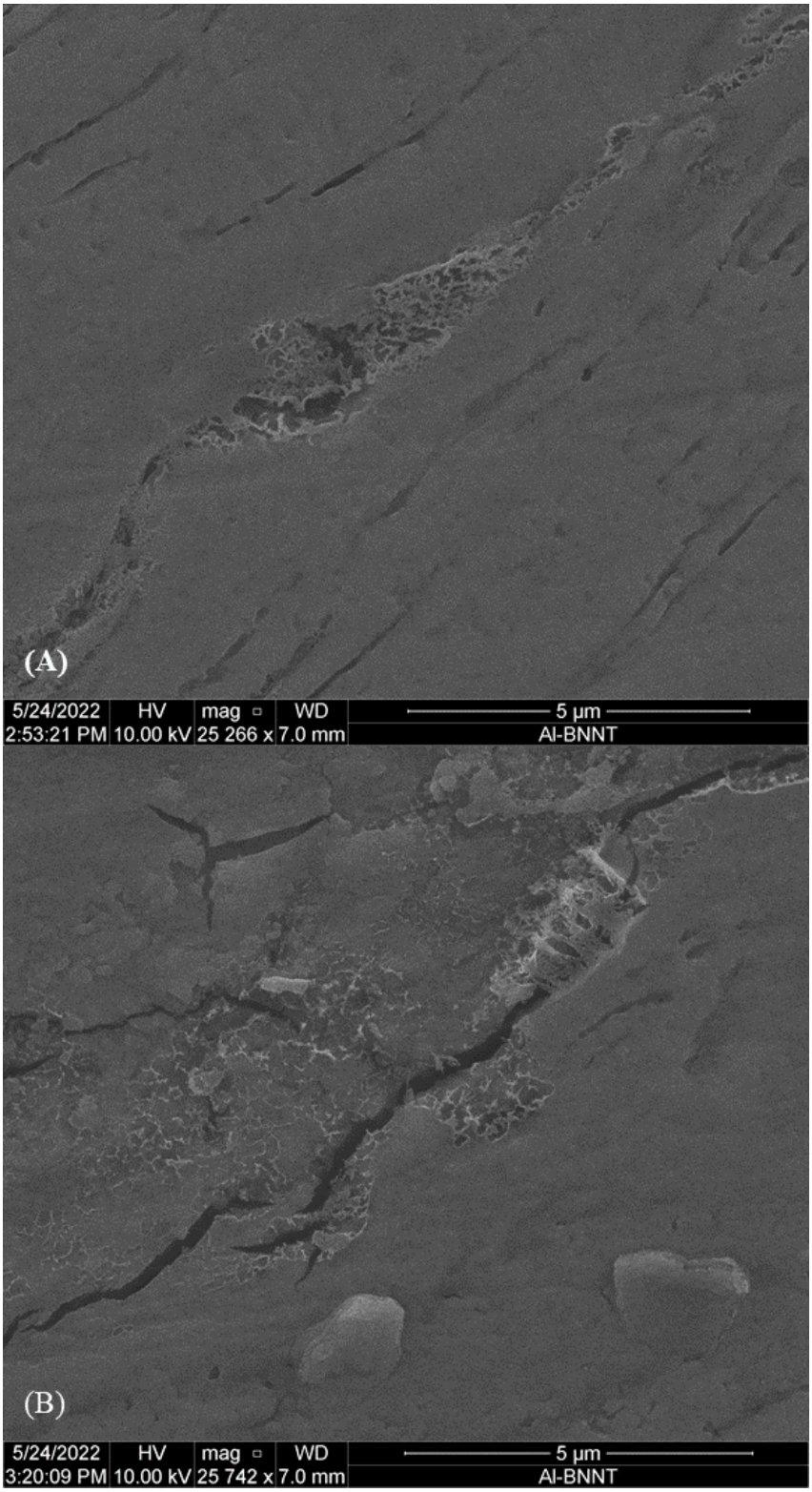

Figure 36. Two different areas of the Al/BNNT coating where BNNT webs surround and encompass splat boundaries

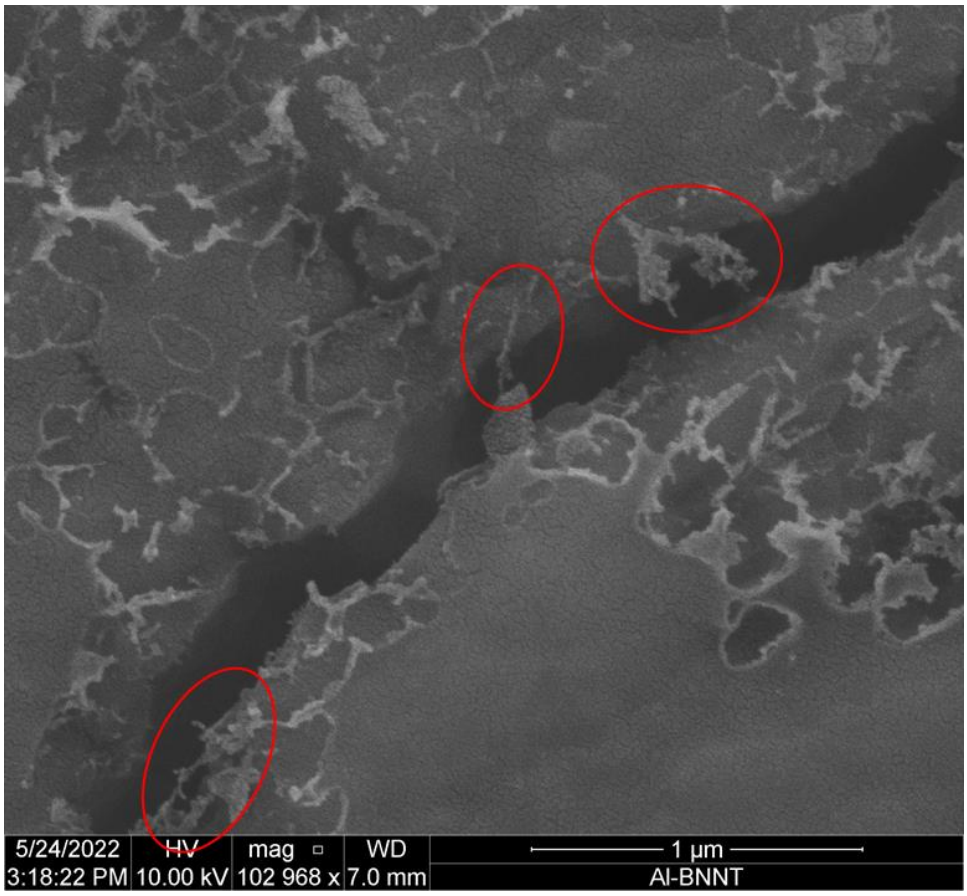

Figure 37. Magnified image of Figure 36b showing the existence of single BNNTS and agglomerated BNNTs at the splat boundary

The final coating is the Al/B_4C/BNNT or All3 composition. As a reminder, this composition contains 2 vol.% B_4C and 2 vol.% BNNTs. Figure 38 shows an image of the coating at the same magnification shown in Figure 31, the 4 vol.% B_4C coating. As compared to Figure 31, the All3 coating has much less B_4C visible and there is less B_4C ejection sites. The surface itself looks smoother in comparison to the Al/BNNT composition. Pores and splat boundaries are almost nonexistent.

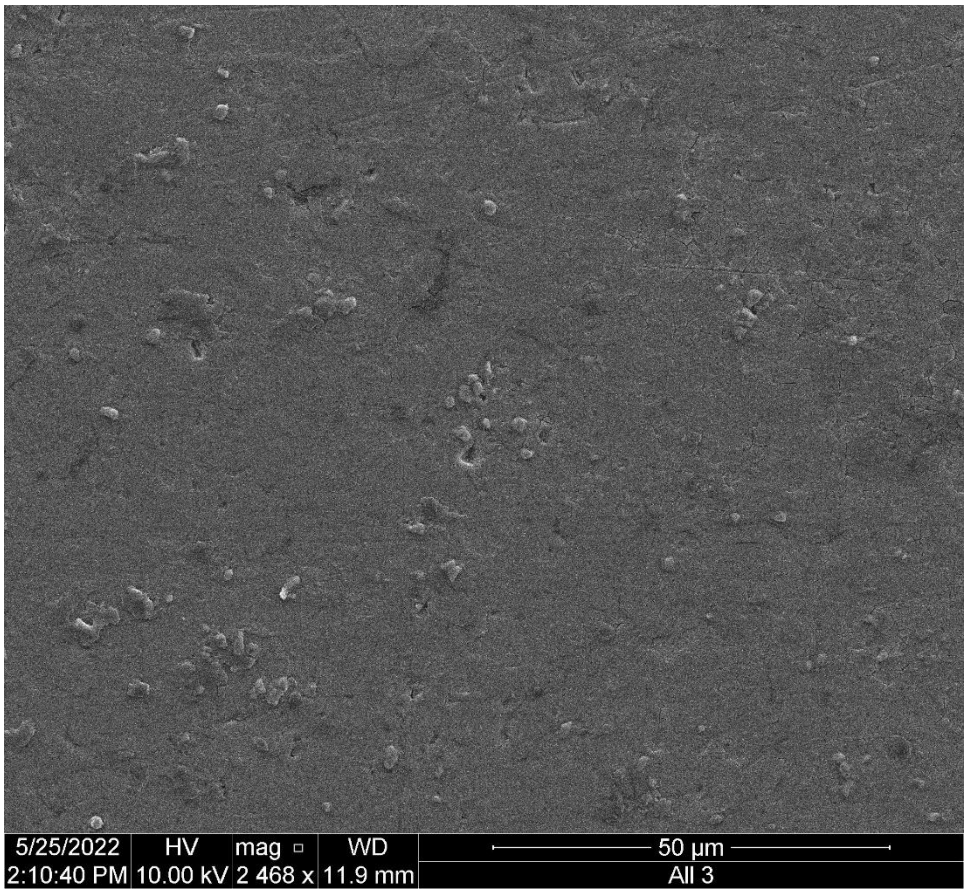

Figure 38. Overview image of the Al/B_4C/BNNT composition

There are less examples of B_4C and BNNTs within splat boundaries in this composition. Again, this is likely due to the decreased vol.% and the poor deposition efficiency. Figure 39 shows a B_4C, circled in red, situated at the intersection of multiple splat boundaries. The right side features the jagged, pronounced geometry of a typical B_4C while the left side seems to fade away into the rest of the coating. The left side of the B_4C is sticking into the coating with the right-side protruding outward. A small grouping of BNNTs is circled in green.

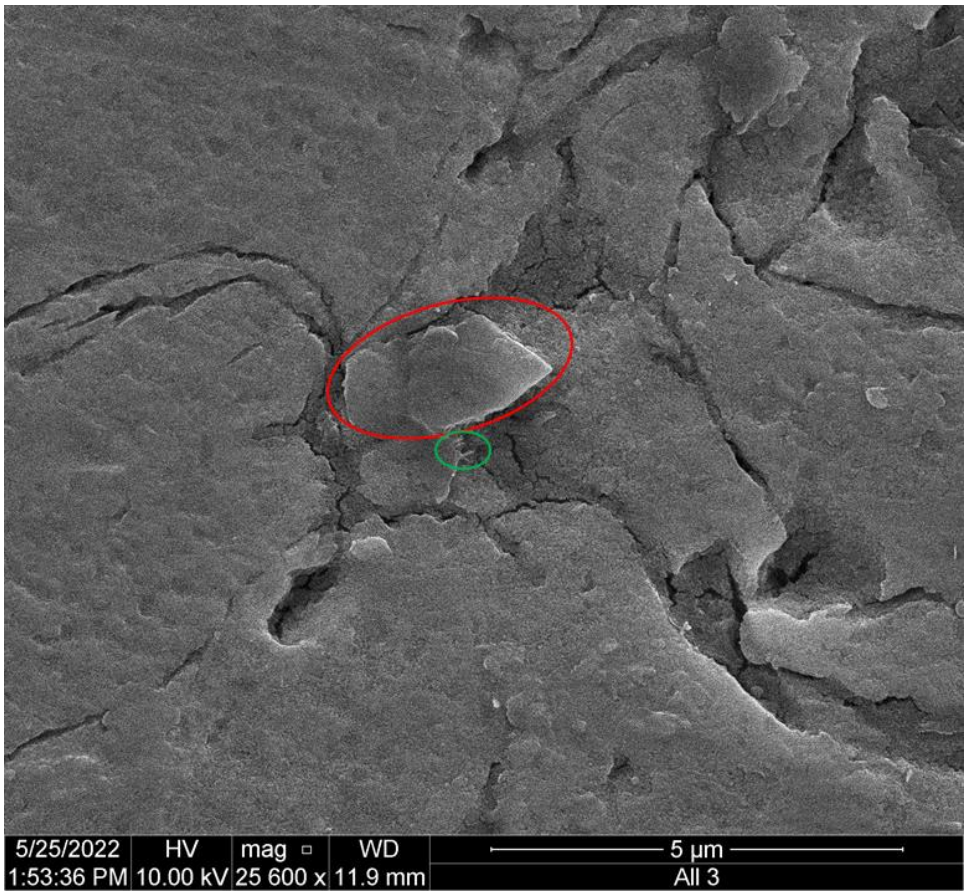

Figure 39. SEM image showing B_4C and possibly BNNTs within a splat boundary

Although it appears that some of the BNNTs were identified in Figure 39, additional evidence of their existence and dispersion needed to be explored. Figure 40 shows an example of a chopped up BNNT outside of a splat boundary; this BNNT appears on the left half of the image, looking very bright. This piece of a BNNT measures approximately 30 nm in width and 267 nm in length compared to the manufacturer's specifications of 60 nm width and up to 20 µm in length.

Figure 40. SEM image showing a chopped BNNT

Figure 41a shows a pore consisting of what appears to be primarily BNNT and possibly some B_4C particles. Figure 41b shows this same pore magnified. The coarse area within the pore is filled with agglomerated BNNTs that vary in shape and size. There are a few indications that BNNTs are filling the pore. Although the cold spray coatings have been sputter-coated (refer to Chapter III, Section G, Subsection 1, "Metallurgical Inspection"), at very high magnifications (~100k), charging was observed within the image and distorted the field of view. The other reason is that further imagery reveals this clumping is consistent throughout all the compositions containing BNNTs. Some of these images will be presented in later sections. The final take away is that BNNTs and B_4C were again located within splat boundaries and pores. Although clumping may have occurred, the ceramic reinforcements are being found in the splat boundaries.

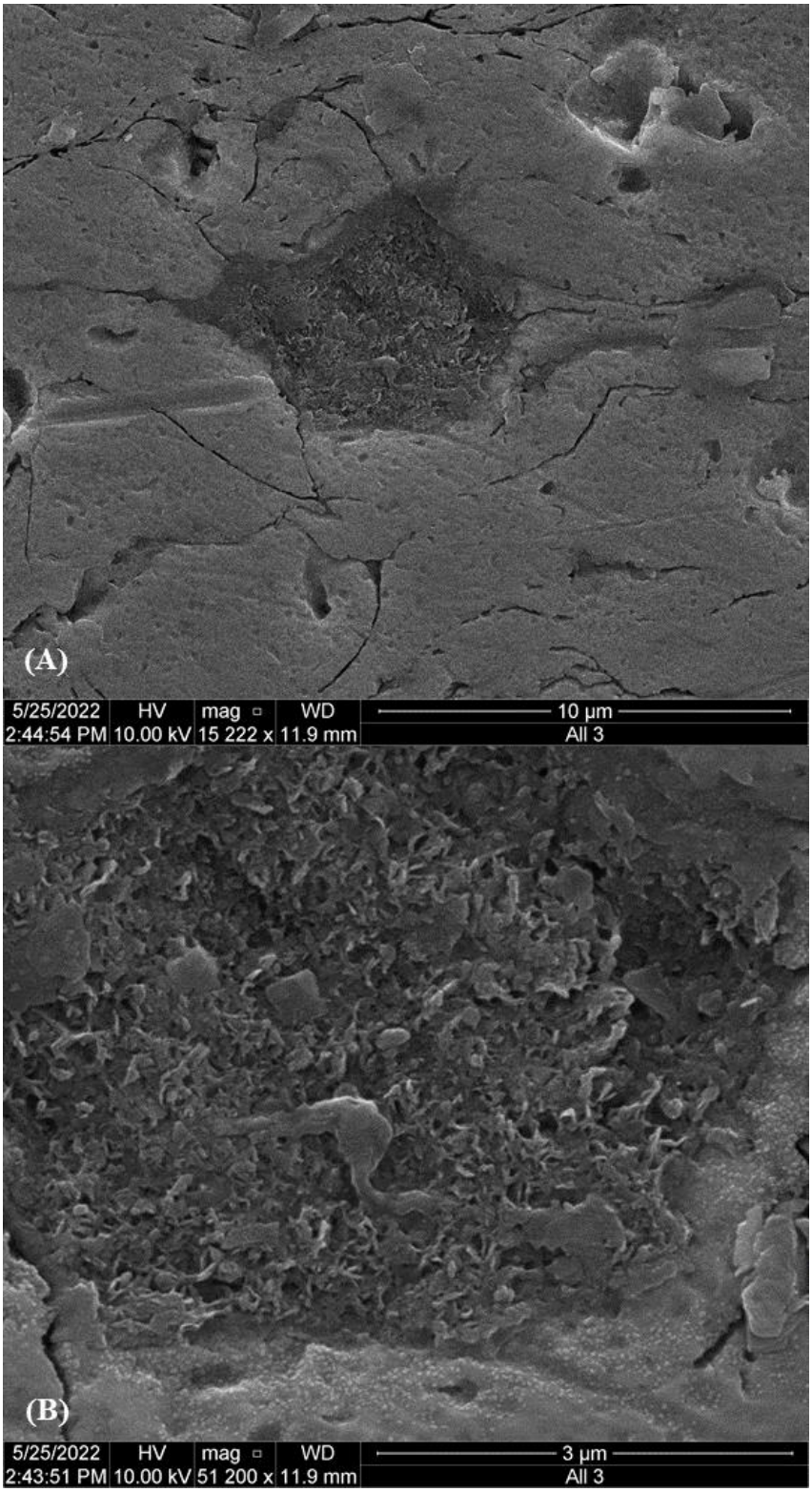

Figure 41. SEM image showing a pore a) pore intersects splat boundaries b) the magnified image of the pore showing agglomerated BNNTs

4. SEM Top-Down Imagery of Cold Spray Coating

After spraying the specimens, visual inspection revealed differences in the coatings (see Figure 28) with the most obvious difference being the porosity of the Al/BNNT coating. Figure 42 is a collage of low magnification top-down SEM images for each composition. The Al and Al/B_4C compositions look very similar; the small mounds resemble non-splatted Al powder particles. The Al/B_4C/BNNT coating is comparatively smooth. The outlier is the Al/BNNT composition. The top-down view shows craters spaced throughout the surface. Between the craters, the coating rises into a ridge. The craters vary in depth, size, morphology, and spacing.

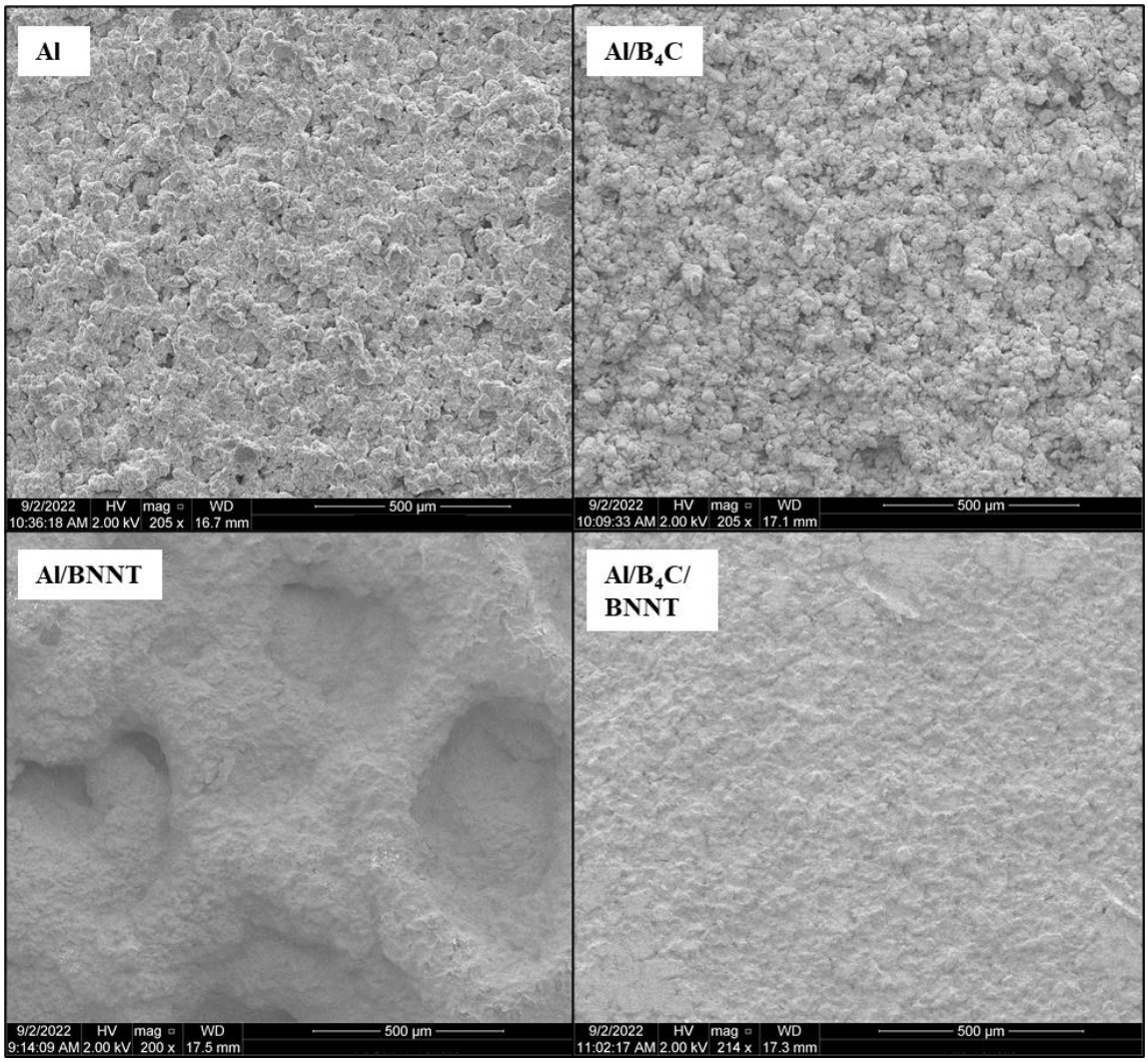

Figure 42. Top-down SEM images of each cold spray composition

Figure 43 is a higher magnification image focused on the bottom of a crater. The walls of the crater are a rough texture. These objects in Figure 43 are not B_4C contamination because the objects are too large. These features measure anywhere between 10 and 50 µm while the B_4C from the manufacturer measured between 1 and 3 µm. These features are primarily located within the craters, but a few can be found scattered on the ridges between the craters.

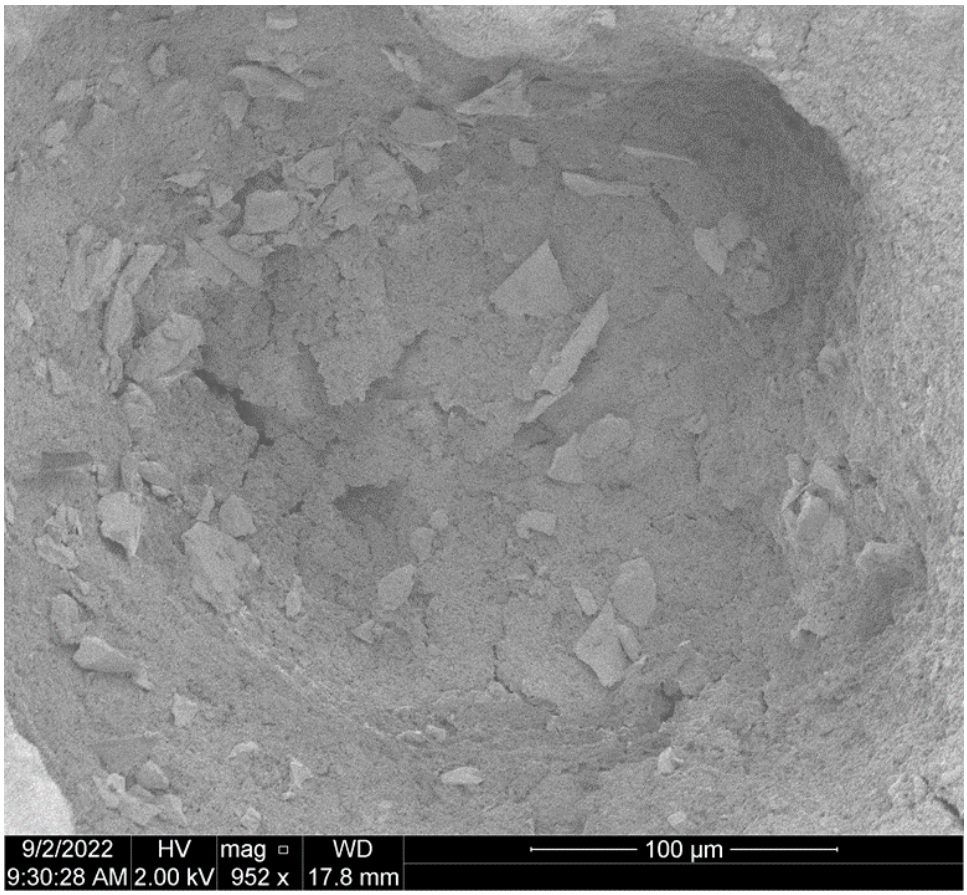

Figure 43. SEM top-down image of the inside of an Al/BNNT composition crater

Figure 44 is a higher magnification image focusing on a crack located at the bottom of the crater. The figure shows in greater detail the texture of the crater walls and floor. Additionally, there are identifiable BNNTs at the crack location; again, acting as anchors between splat boundaries. The BNNTs are circled in red in Figure 44.

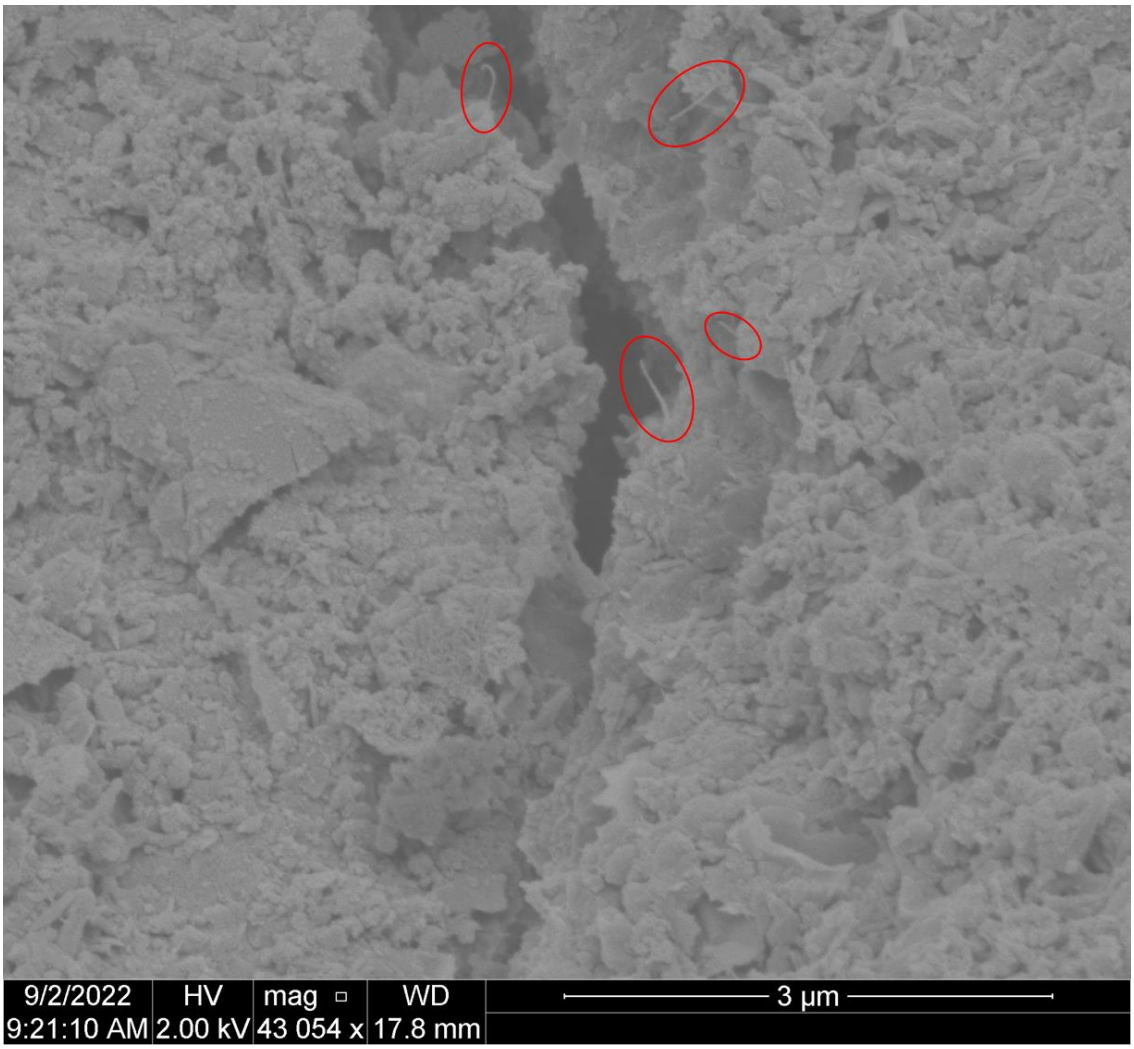

Figure 44. SEM top-down image of individual BNNTs located within Al/ BNNT composition crater

The Al/BNNT coating has a lower deposition efficiency and thinner/inconsistent coating thickness compared to the other compositions. A cratered surface was also unique to the Al/BNNT composition. The addition of 4 vol.% of BNNTs clearly has a detrimental effect on the cold spray coating. The craters must form during the spraying process and are likely due to impact from BNNT agglomerations. The morphology of the BNNT agglomerations seen in Figure 24 (loose powder before spraying) and again in Figure 41 (cross-section of Al/BNNT coating) matches well with the morphology of the crater walls seen in Figure 43Figure 44. A reason for the sharp plate-like particles in the craters requires further investigation.

C. HARDNESS

Hardness of Al is one of the mechanical properties that this study is attempting to increase by adding ceramic reinforcements. Hardness can be correlated with the strength of a material and more importantly, the wear resistance of the surface. The four compositions were tested for micro-indentation hardness at 15 different locations throughout each coating; pores within the coating were avoided. Figure 45 shows the average hardness for each composition and the error bars represent one standard deviation. The Al/B_4C composition experienced a 4.1% decrease in hardness over the control, while the Al/BNNT composition experienced an 14.1% increase, and the Al/B_4C/BNNT saw an increase of 20.8% over the control. Additionally, the standard deviation in the Al/B_4C/ BNNT composition was 67% smaller than the composition with the next smallest standard deviation.

To increase the hardness of a material or coating, the material must resist dislocations. The dislocations occur when a stress, such as a micro-indenter, is applied to the material and then propagates throughout the crystal structure. During the cold spray process, a high density of dislocations is already common in the coating from the high energy collisions between the cold spray particles and the surface. Adding reinforcements increases the density of the coating. Properly dispersed reinforcing materials, such as BNNTs and B_4C, can pin (stop) these dislocations from occurring; thus, increasing the harness of the material. This phenomenon is known as Orowan strengthening [48]. The outlier from Figure 45 is the Al/B_4C since its hardness is lower than that of the pure Al coating. Adding µB_4C to Al cold sprayed coatings was previously shown to be effective in increasing hardness [9]. The slight decrease in hardness may be due to the low vol.% of B_4C used in the coating or that the B_4C were sprayed onto a soft substrate. Often, the added ceramics will not reflect large increases in hardness until the vol.% is drastically increased. There are tradeoffs associated with increasing the vol.% of reinforcements. The possibility exists that increasing the vol.% of the reinforcements too high will begin to negatively affect mechanical properties, other than hardness, of the cold spray coating.

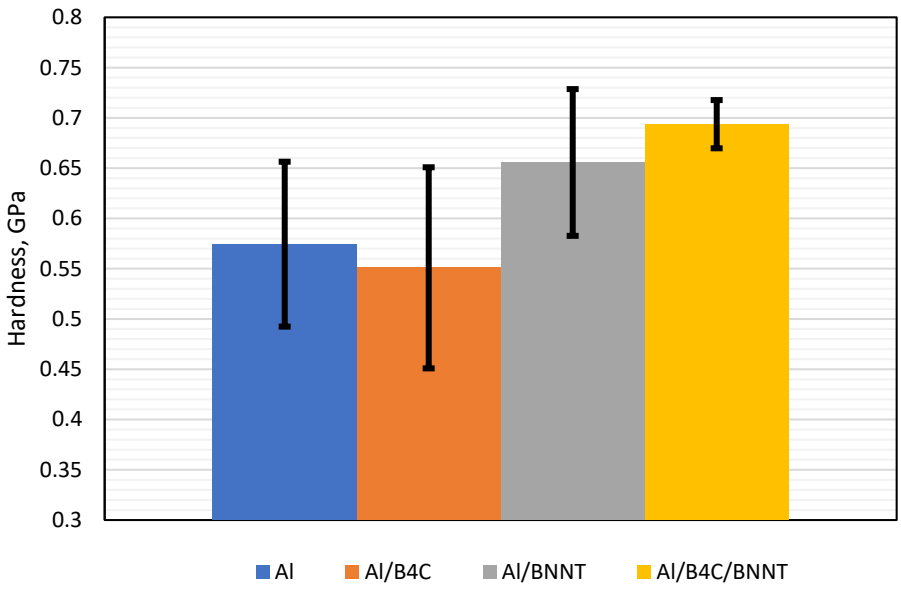

Figure 45. Results from Vickers micro-hardness testing

Cold spray coatings vary from conventional alloys in that nano and micro particles are embedded into the Al, where in an alloy they are integrated. Due to these particles being embedded, nanoindentation is the only tool to measure local changes in hardness and elastic modulus. Figure 46 shows the nanoindentation results for all four compositions. The blue dots represent all 100 indentations, the red dot represents the average, and the black box represents one standard deviation from the average. The Al/B_4C composition had the largest standard deviation, this matches the pattern in Figure 45. The other three composition's standard deviations do not correlate with the results from Figure 45. Both compositions that contain B_4C have the largest standard deviation.

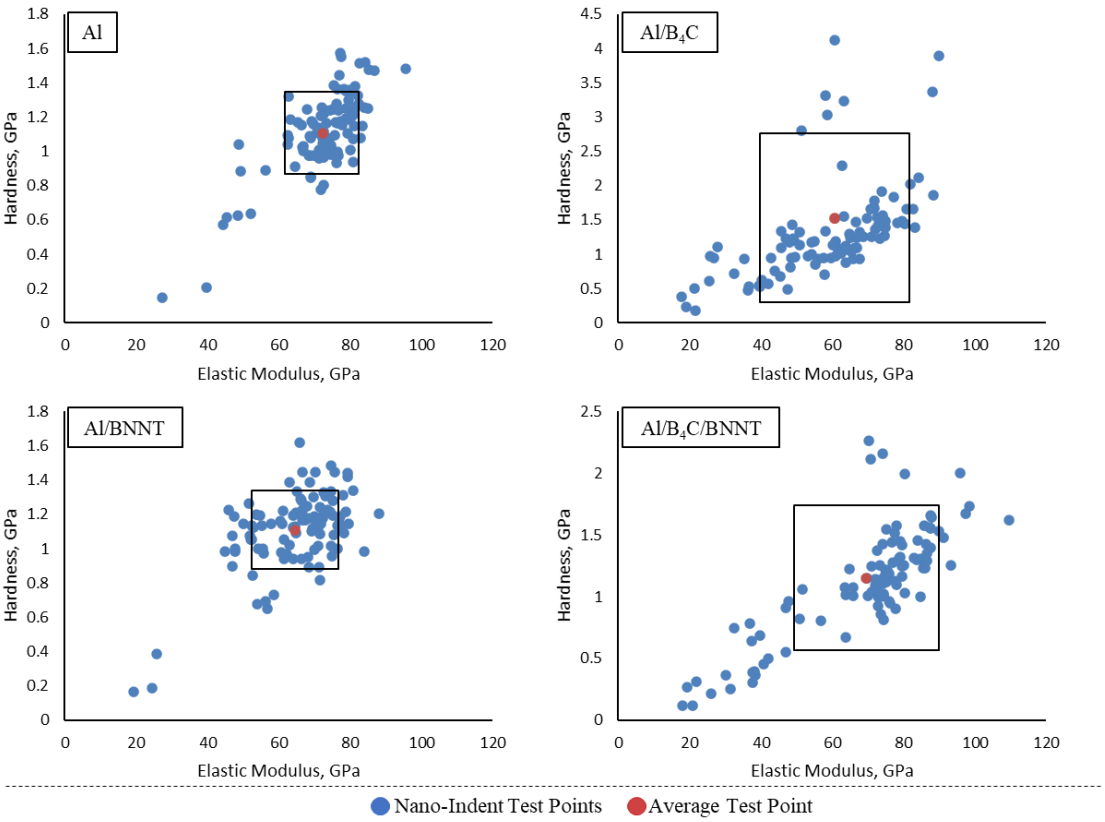

Figure 46. Nanoindentation results for each composition

Figure 47 combines the four standard deviation boxes and averages into one plot. The Al/B_4C composition had a 37.1% increase in hardness over the control Al sample, and a 15.7% decrease in elastic modulus. The Al/BNNT coating had the same hardness as the Al sample, and a 10.6% decrease in modulus. The Al/B_4C/BNNT had an increase of 4.2% increase in hardness, and a 3.6% decrease in elastic modulus. The results show that adding one ceramic reinforcement to coatings will decrease the elastic modulus and the hardness will maintain or increase from the control. Although the Al/B_4C/BNNT composition had a slight increase in hardness, the composition did not exhibit synergistic improvements. Ideally, the B_4C and BNNTs together would have taken the load from the matrix and increased the composition's strength.

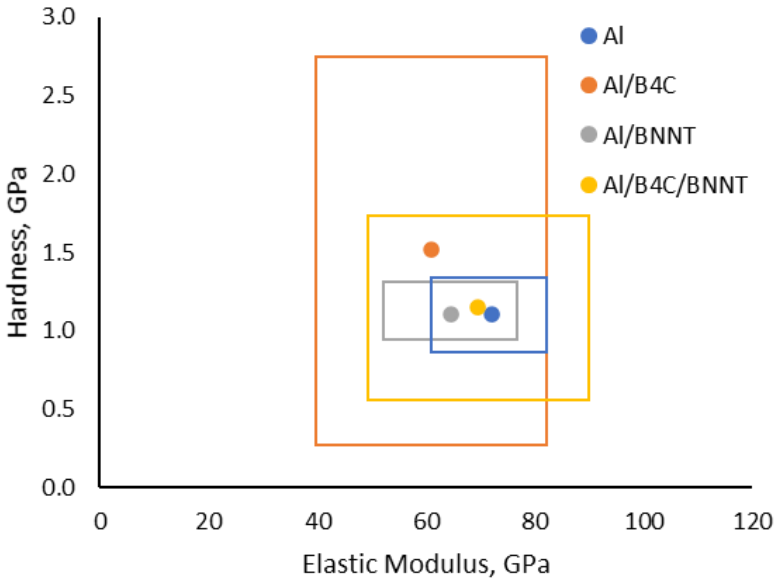

Figure 47. Comparison of nanoindentation hardness and elastic modulus

The large standard deviations of both compositions containing B_4C is attributed to the nanoindenter occasionally indenting pure aluminum, and other times indenting a single B_4C or a B_4C-Al boundary. Figure 48 demonstrates the various ways an indenter can interact with the cold spray coating. As stated in Chapter III, Section F, Subsection 1, "Nanoindentation," the nanoindentations were evenly distributed in a grid throughout the cold spray coating. Then, each point is verified to ensure it is not sitting on a void, pore, or scratch. These points are not moved if they fall directly on a B_4C, as this can accurately represent the properties of the area the indent is occurring. The standard deviation decreases when the vol.% of B_4C is decreased from 4 to 2 and again when the B_4C are not present in the composition.

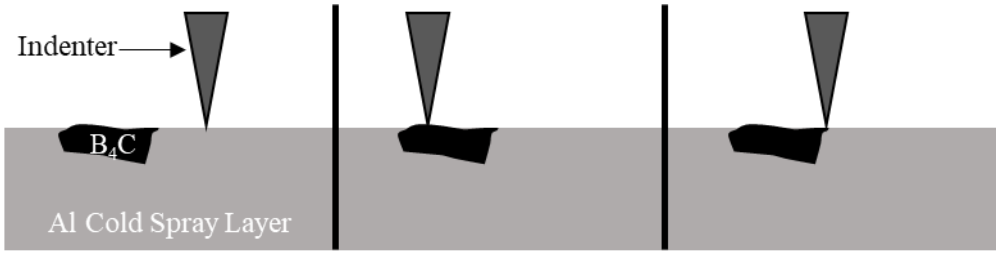

Figure 48. Indenting pure aluminum (left), indenting only a B_4C (middle), indenting the aluminum/B_4C boundary (right)

Average load vs. displacement curves for each composition is shown in Figure 49. Figure 49 validates the results in Figure 46 and 47. The largest displacements were seen in the Al and Al/BNNT coatings, because they exhibit lower mean hardness than the Al/B_4C coating. The load-displacement curves are all concave down as the sample is loaded to the ~3 mN. The horizontal line indicates the portion of the test where the load is held for 3 seconds. Then the curve is unloaded. The unloading portion is where the elastic modulus (or stiffness) is computed, and the plasticity can be calculated. If a test does not follow this pattern, or shows any irregularities, its data is removed. Figure 49 shows that all the curves are very similar in shape but are offset slightly in displacement; indicating there is no significant difference in work between the indentations.

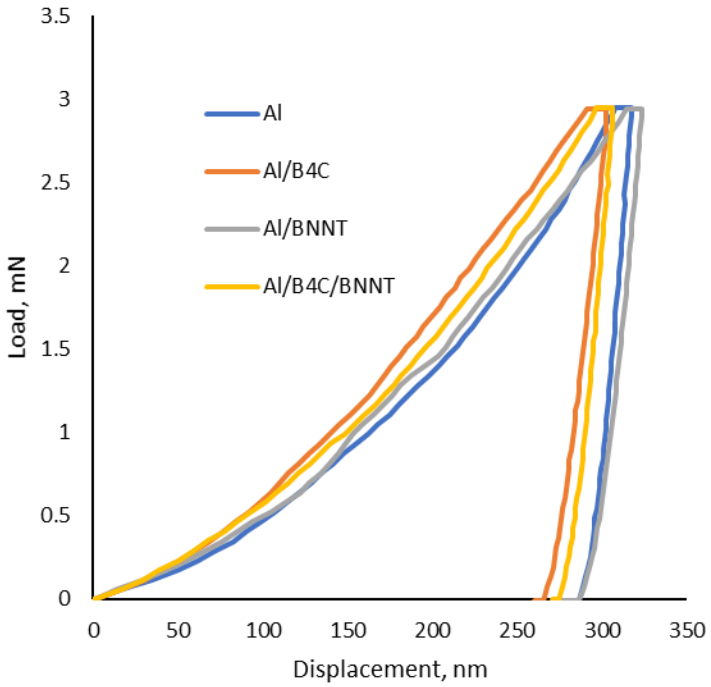

Figure 49. Representative average load-displacement curves from nanoindentation

Plasticity is the ability of a material when deformed to remain in this deformed state. Plasticity can be calculated by using the unloading curves. The ratio of the maximum displacement to the displacement remaining after the load is completely removed will equal the percent plasticity. Table 15 shows the plasticity calculations of the representative average for each nanoindentation. The Al composition has the greatest inclination to remain near its max displacement, while the Al/BNNT coating exhibits greater elastic tendencies.

Table 15. Percent Plasticity from the Average Nanoindentation

Composition ID	Plasticity [%]
Al	89.4
Al/B_4C	86.2
Al/BNNT	85.3
Al/B_4C/BNNT	88.8

D. ADHESION

Figure 50 shows the adhesion strength of each cold spray coating at fracture. The black error bars represent one standard deviation from the mean. This plot does not consider the mode in which the coating failed. The only coating that had an increase in adhesion strength from the Al was the Al/B_4C coating; this coating experienced a 31.2% increase but had the largest standard deviation. The Al/BNNT composition experienced a 6.4% decrease. The Al/B_4C/BNNT coating experienced a 0.2% decrease but had a much smaller standard deviation compared to the control. This data suggests the B_4C acts as effective anchors between the Al splats as well as between the substrate and the cold-spray coating. The variance in the B_4C coating is likely due to a combination of the B_4C being unevenly distributed throughout the coating and the increased residual stresses the substrate incurs when the hard B_4C particles impact it during spraying.

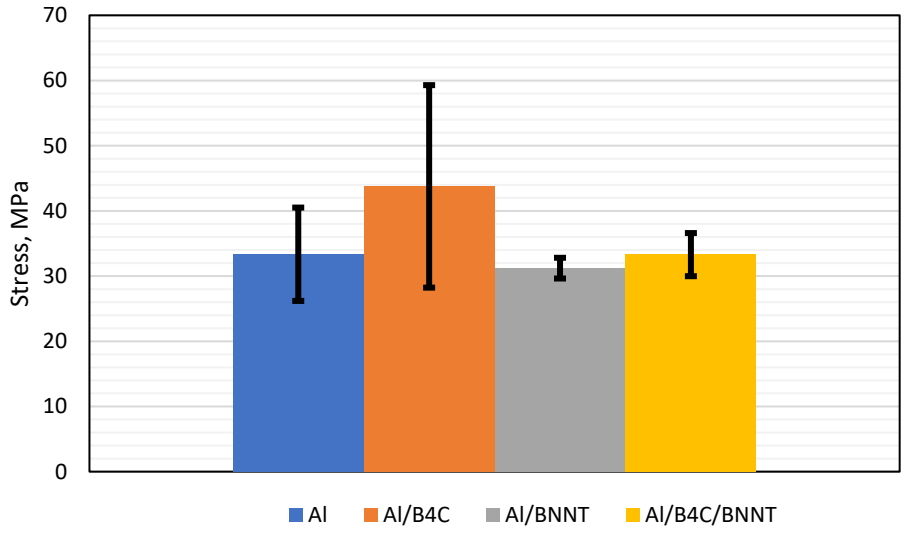

Figure 50. Adhesion testing results

Three main failure modes occur during adhesion testing: failure at the substrate/ coating interface, failure at the glue/coating interface, and failure within the coating; failures can be a combination of the multiple failure modes. In a real-world application, there is not a glue failure. This leaves the two true failure modes as delamination failure between cold spray coating and the substrate, and the cohesive failure within the cold spray coating itself. Figure 51 shows the most common failure mode for each composition. All Al adhesion tests experienced delamination of the cold spray coating from the substrate. This suggests that the bonding between the Al powder particles is stronger than the bonding between the substrate and the Al powder. The Al/B_4C mostly exhibited cohesive failure, similar to Figure 51, where the center of the adhesion dolly failed partially within the cold spray coating and partially at the substrate. One Al/B_4C test did experience delamination failure like Al. Al/BNNT failed cohesively through all tests as seen in Figure 51. Although Al/BNNT saw cohesive failure, the pullout zone was inconsistent in thickness and where the failure occurred. The Al/B_4C/BNNT failure in Figure 51 represents every failure of this composition; each adhesion test failed evenly, and cohesively, within the cold spray coating near the surface.

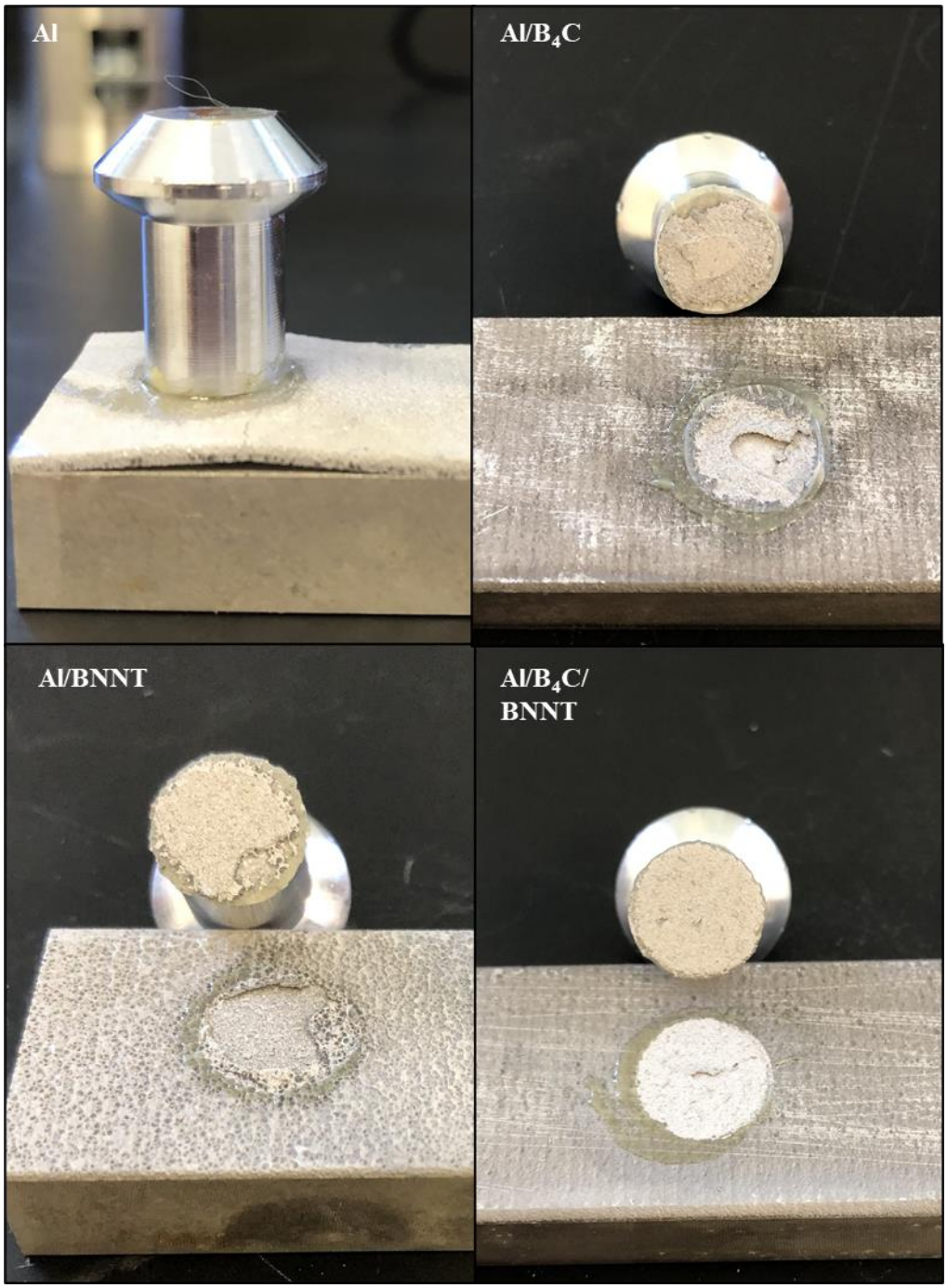

Figure 51. Most common failure mode for each cold spray coating

To preserve the delicate features from each of the adhesion tests, the choice was made to use top-down SEM imagery rather than cross-sectioning, grinding, and polishing the adhesion fracture surface. Figure 52 shows SEM images of the outer area of the Al/B_4C

adhesion test, the area being imaged is shown using the red square in the top left image. Figure 52a has a morphology that resembles that of a brittle fracture. Figure 52b is a magnified image of Figure 52a. Here, the Al splats are visible; one splat is outlined in red. An Al particle that retained a shape similar to the powder from the post processing figures is circled in red. The green circles are highlighting some of the visible B_4C. These three features are seen throughout the outer area of the Al/B_4C adhesion fracture surface.

Figure 53 shows the inner area of the Al/B_4C adhesion test, the area being imaged is again shown using the red square in the top left image. Figure 53a is a lower magnification image of this area. Without EDS testing available, it is difficult to determine whether this is primarily substrate or coating being imaged, but when compared to the texture seen in Figure 52a, this area is primarily the substrate with islands of the cold spray coating. Upon further inspection of Figure 53a, small craters were found throughout the image; these craters are circled in red. Figure 53b shows a magnified example of one of these features. The center of the crater is the same shape and size as a B_4C particle. The area around the B_4C vacancy looks like a capillary wave (or ripple) that occurs when a raindrop hits a water's surface. These features suggest that the B_4C is acting as anchoring sites for the cold spray coating during the adhesion tests. These features will be discussed later within this section.

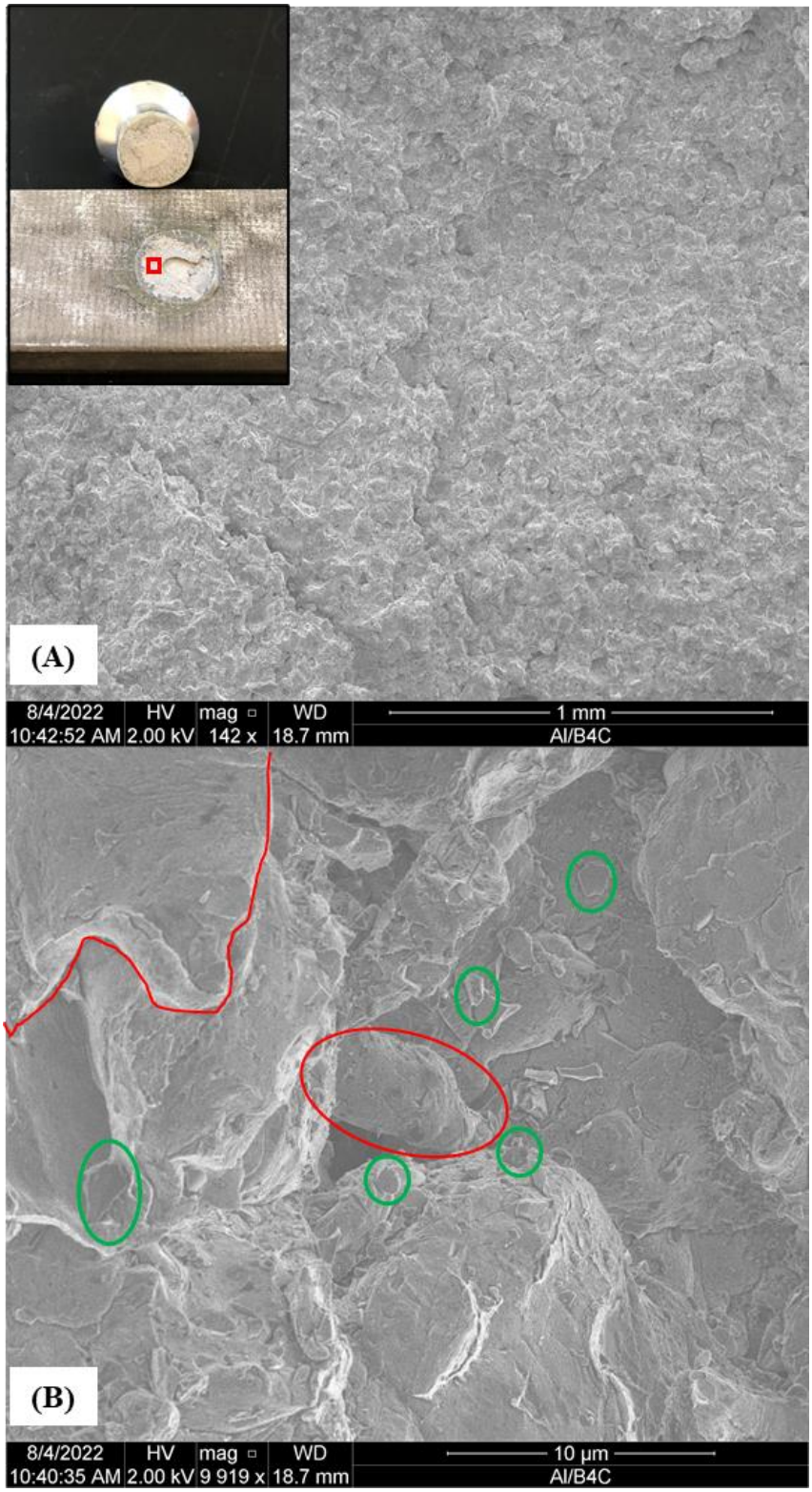

Figure 52. Al/B_4C adhesion fracture surface a) overview b) magnified image showing B_4C and splat boundaries

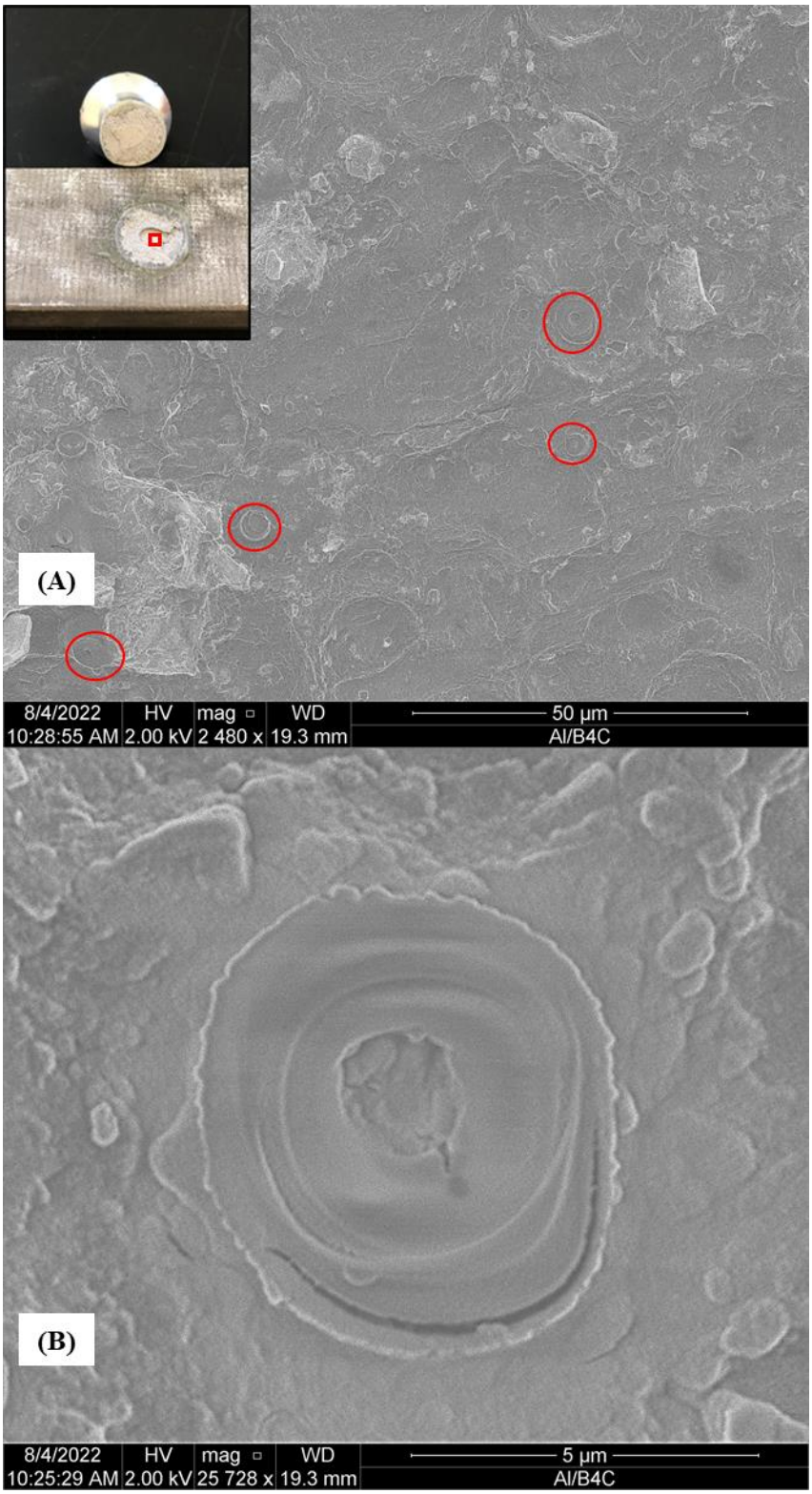

Figure 53. Al/B_4C adhesion fracture surface a) substrate with areas of coating b) magnified imprint of B_4C ripped out from the substrate

Figure 54 shows top-down images from the Al/BNNT adhesion tests. Aluminum splats can clearly be seen in Figure 54a, indicating cohesive failure. Figure 54b is a magnified image of the dark center portion seen in Figure 54a. Although slightly different than the spider-web like features seen in Figure 36, Figure 54b does show the BNNTs are encompassing a large aluminum particle and appear to be 10 μm in length. In magnified images, the BNNTs appear to be slightly pulled away from the Al particle as if another Al splat was removed from above the BNNTs during adhesion testing. This indicates the BNNTs are indeed positioned within the splat boundaries, acting as effective anchors, and possibly becoming stretched during the adhesion tests.

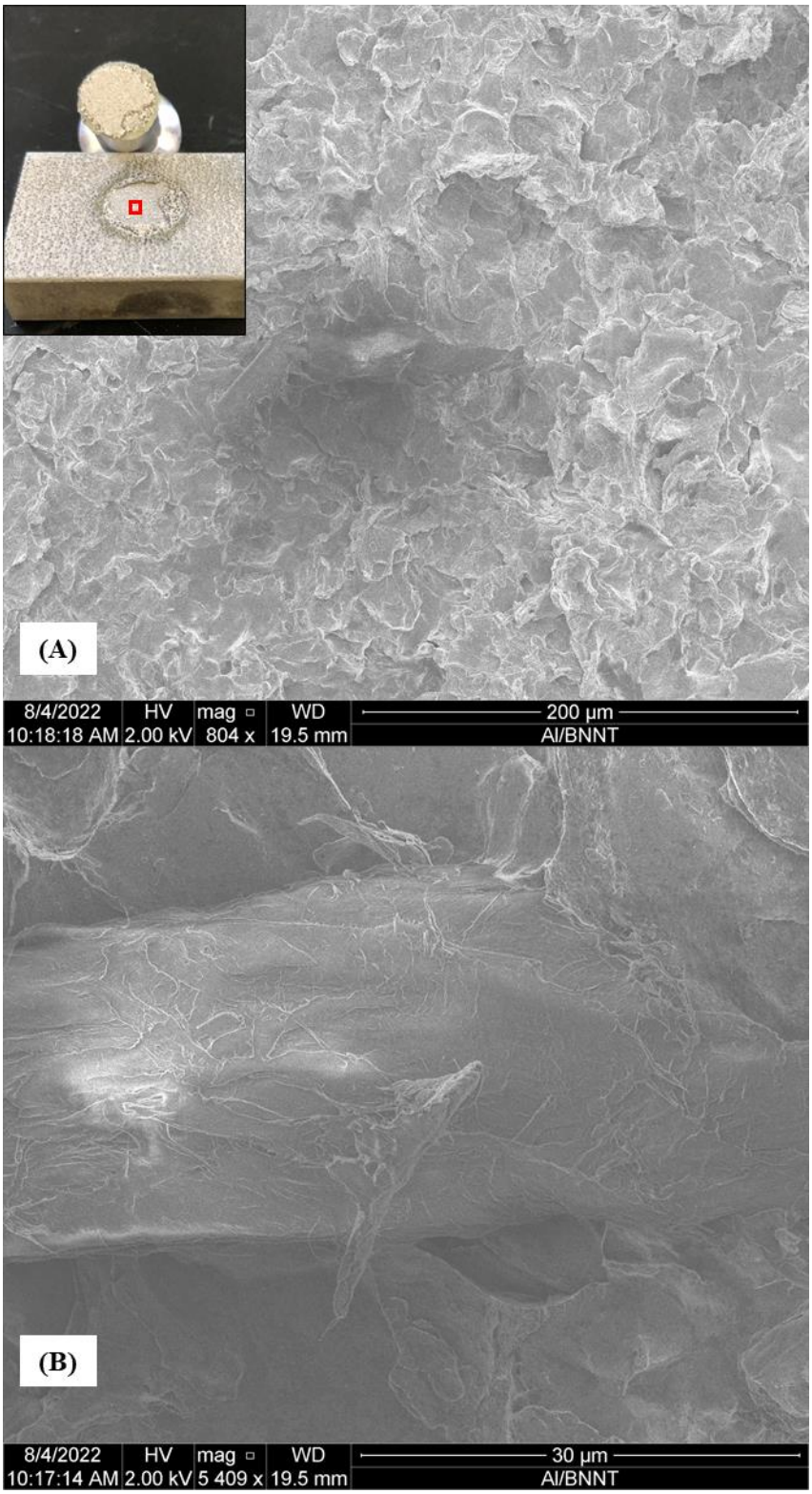

Figure 54. Al/BNNT adhesion fracture surface a) overview showing failure within coating b) aluminum splat covered in BNNTs

Figure 55 is an additional image from the Al/BNNT adhesion test. Here the red outline is showing a grouping of splats stacked on top of one another that appears to have been dislodged during the adhesion test. The ends of BNNTs are visible between the stacked splats.

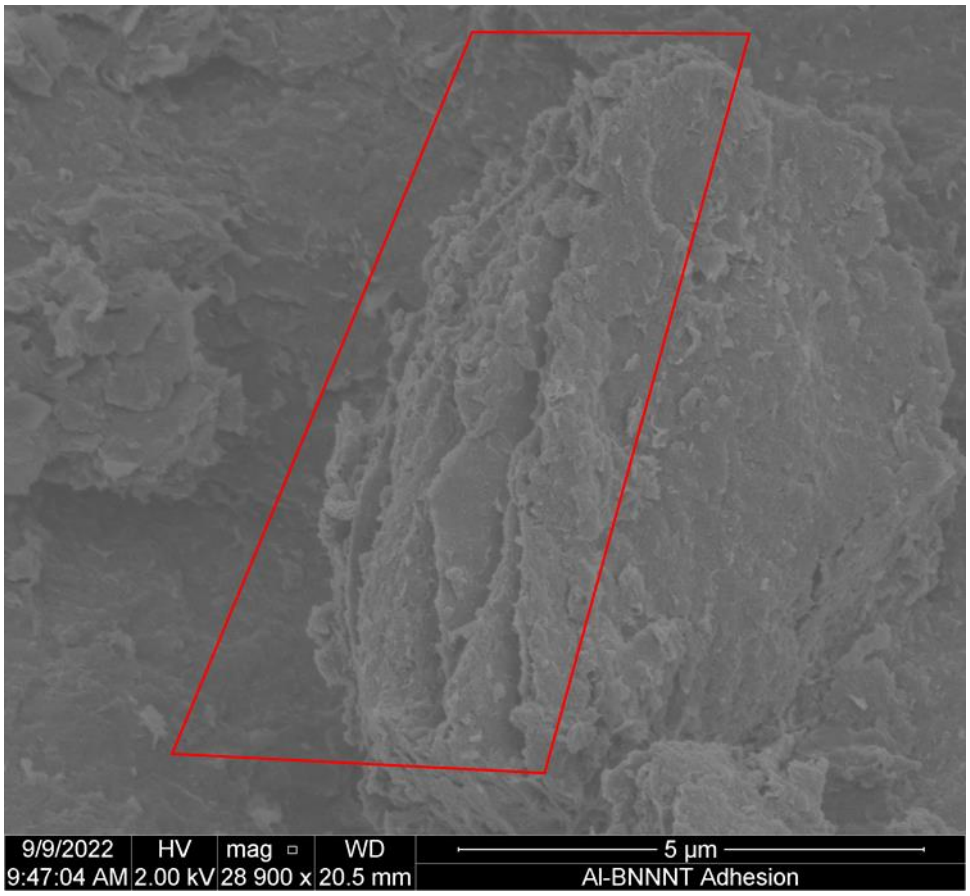

Figure 55. Al/BNNT adhesion fracture surface showing BNNTs sandwiched between aluminum splats

Out of all the compositions, the Al/B_4C/BNNT composition clearly failed cohesively. Figure 56 shows a low magnification image of the adhesion test. Notice how similar the topography and morphology of the coating is to the Al/BNNT coating shown in Figure 54a. Again, splats are easily identifiable.

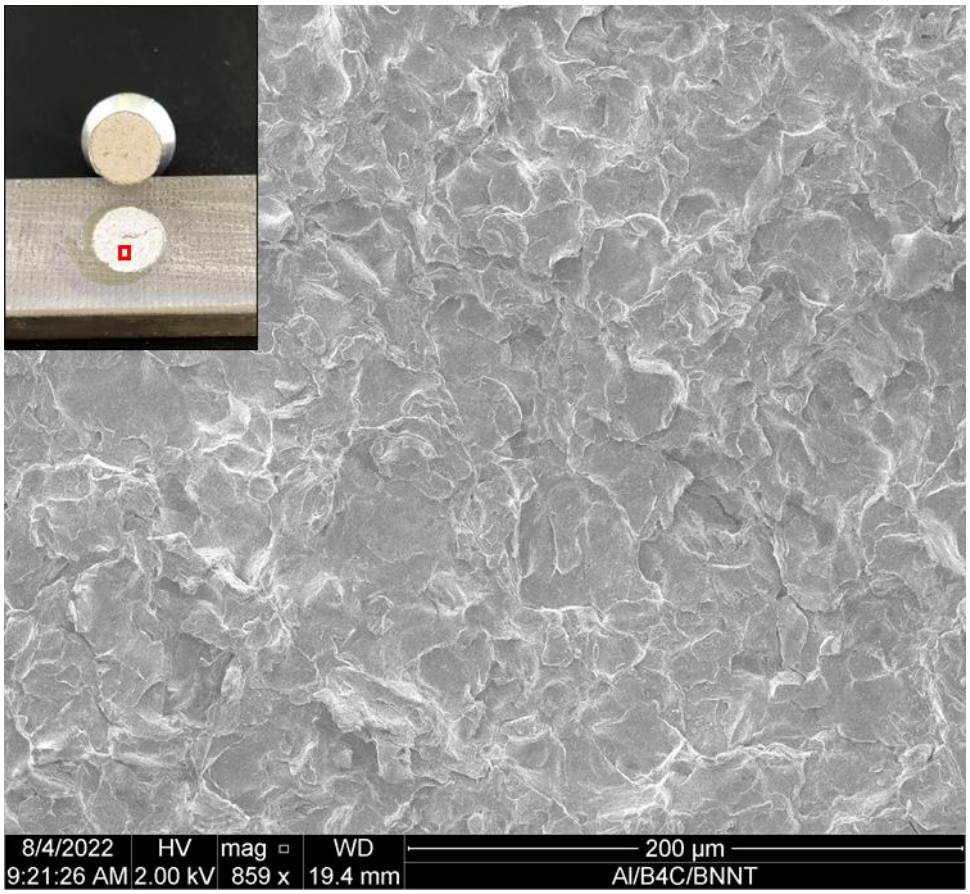

Figure 56. Al/B_4C/BNNT adhesion fracture surface

Figure 57 shows BNNTs wedged between splat boundaries; the splat boundary is to the right of the red dashed line.

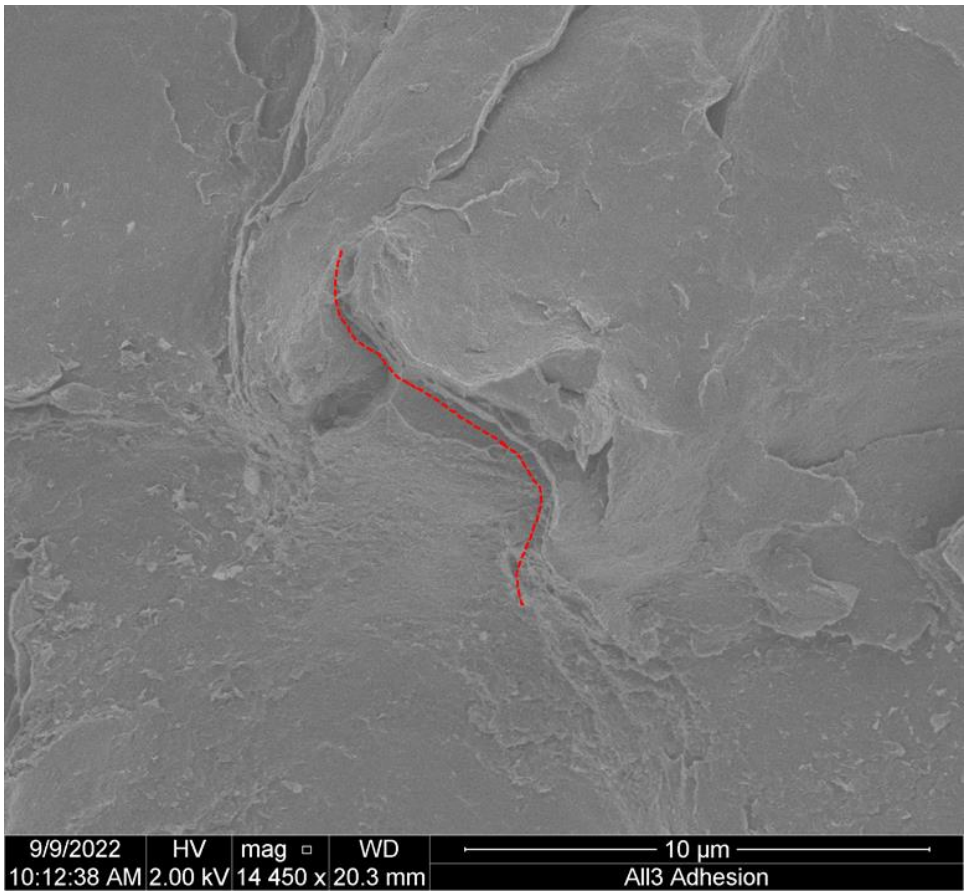

Figure 57. Al/B_4C/BNNT splat boundary and BNNTs

This composition did not fail at the substrate, as the Al/B_4C composition appeared too. Because of this, the question arises as to whether the B_4C leaves the same capillary wave pattern behind on the Al as Al/B_4C composition did on the substrate. Figure 58a shows a section of the All3 adhesion fracture surface, the areas circled in red show small craters similar in size and shape to B_4C. Figure 58b shows a magnified image of one of these B_4C craters. The figure shows that there are no ripple patterns as there was around the B_4C craters in Figure 53b, indicating less force was used to remove the B_4C in this composition compared to the Al/B_4C sample. Figure 58c is another section of the adhesion failure surface; B_4C are circled in green. Here, B_4C are visibly embedded into the top of the splat; opposite of the B_4C craters in Figure 58b.

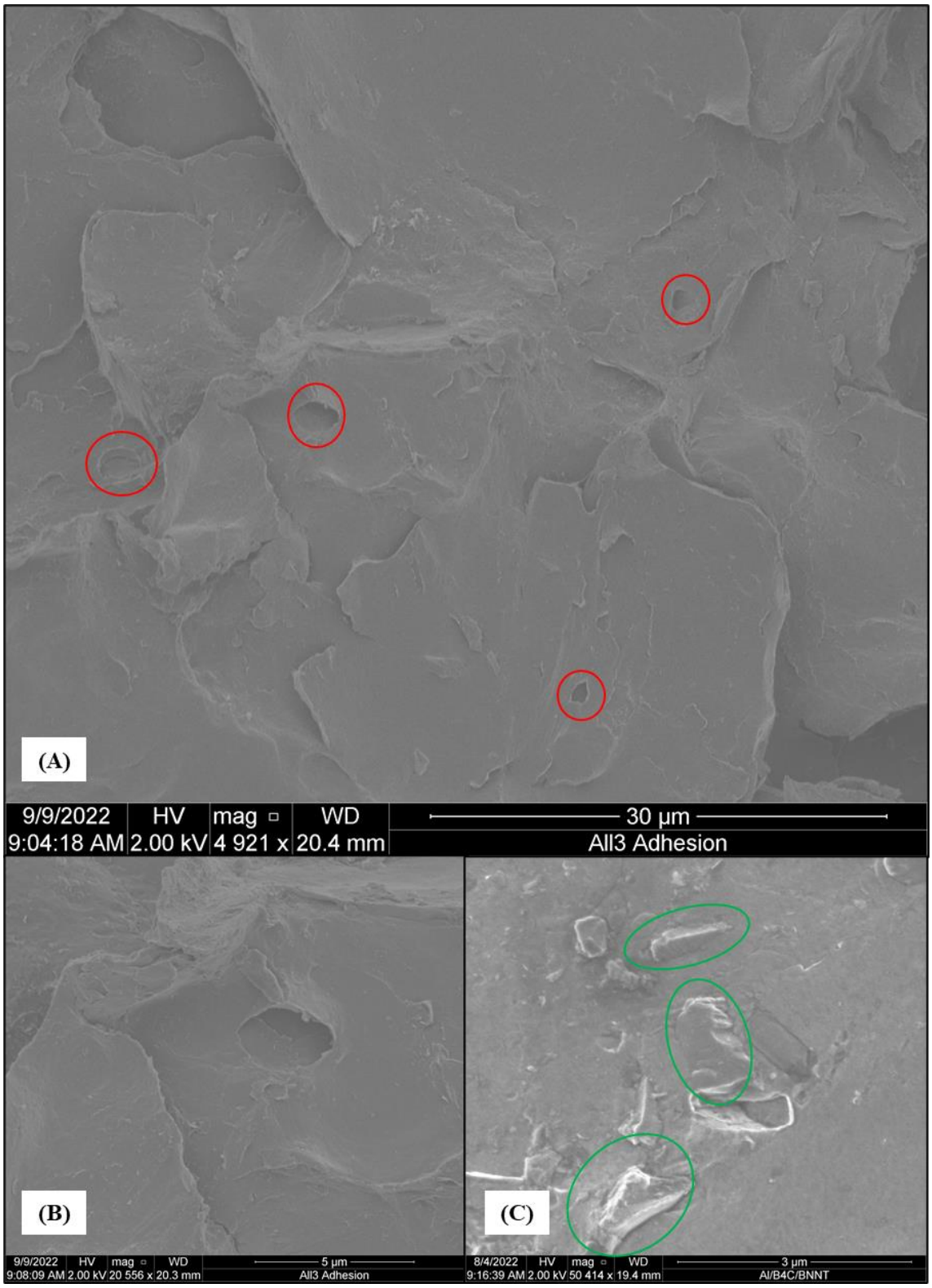

Figure 58. Al/B_4C/BNNT adhesion fracture surface a) B_4C craters on top of splats b) magnified image of B_4C crater c) B_4C embedded in top of splat

Recall in Chapter IV, Section B, Subsection 3, "Coating Deposition and Microstructural Characterization," B_4C were found to be easily ejected when examining the surface of the polished puck. This was equated to the B_4C experiencing a shear force during the cutting and grinding steps. During adhesion testing, the B_4C in the Al/B_4C and Al/B_4C/BNNT coatings were not as easily ejected; these coatings took over 31 MPa of force before failure occurred. The B_4C in the Al/B_4C adhesion test experienced enough force to be dislodged from the Mg substrate causing an outward ripple seen in the SEM. This force imparted by the adhesion testing can be equated to a tensile force, see Figure 59. B_4C demonstrated that they are stronger in tension than in shear. They are effective in holding splats together and anchoring the splats to the substrate.

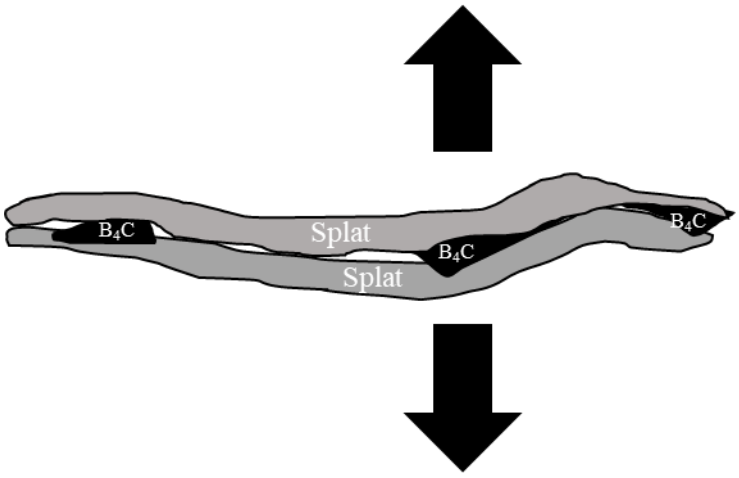

Figure 59. Example of B_4C acting as effective anchors in tension

The specific cold spray application will ultimately determine how a coating is designed to fail. In the marine and aerospace industries there is a desire for a cold spray coating to fail within the coating, i.e., cohesively, rather than delamination at the substrate [11]. When part of the coating remains, a protective coating (that can be repaired) still exists. The coating that remained behind in the Al/B_4C/BNNT adhesion tests, had a thickness that remained over half the original thickness of the coating. Figure 60 is a schematic showing the effect that the hardness of the feedstock material and the hardness of the substrate has on the powder particle's ability to adhere to the substrate. The Mg and

the Al fall into the soft-on-soft category. The addition of the hard ceramic reinforcements (specifically the B_4C) can be thought of moving the powder closer to the hard-on-soft category. Other than the hardness of the materials, the spray parameters and material oxidation can dictate how well the substrate and the cold spray coating adhere to each other.

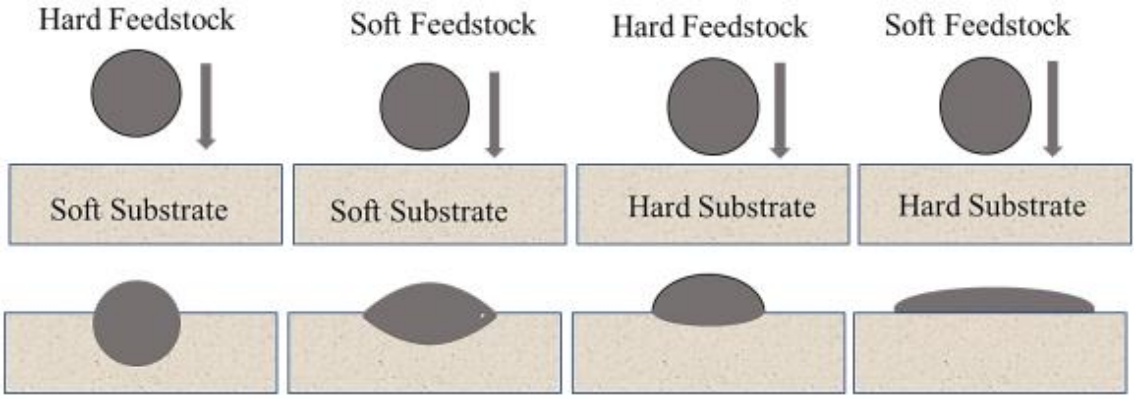

Figure 60. Effect of feedstock and substrate hardness on adhesion. Source: [11].

Figure 61 demonstrates the relationships shown in Figure 60. Figure 61a shows the interface profile between the Al coating and the Mg substrate as the red dotted line. Figure 61b shows the interface between the Al/B_4C/BNNT cold spray coating and the Mg substrate; the red dotted line represents the interface and individual B_4C are encircled in green. Both interfaces show coating penetration consistent with the soft-on-soft diagram in Figure 60. In Figure 61b, the B_4C penetrate further into the Mg substrate, like the hard-on-soft diagram in Figure 60, anchoring the Al coating to the Mg substrate.

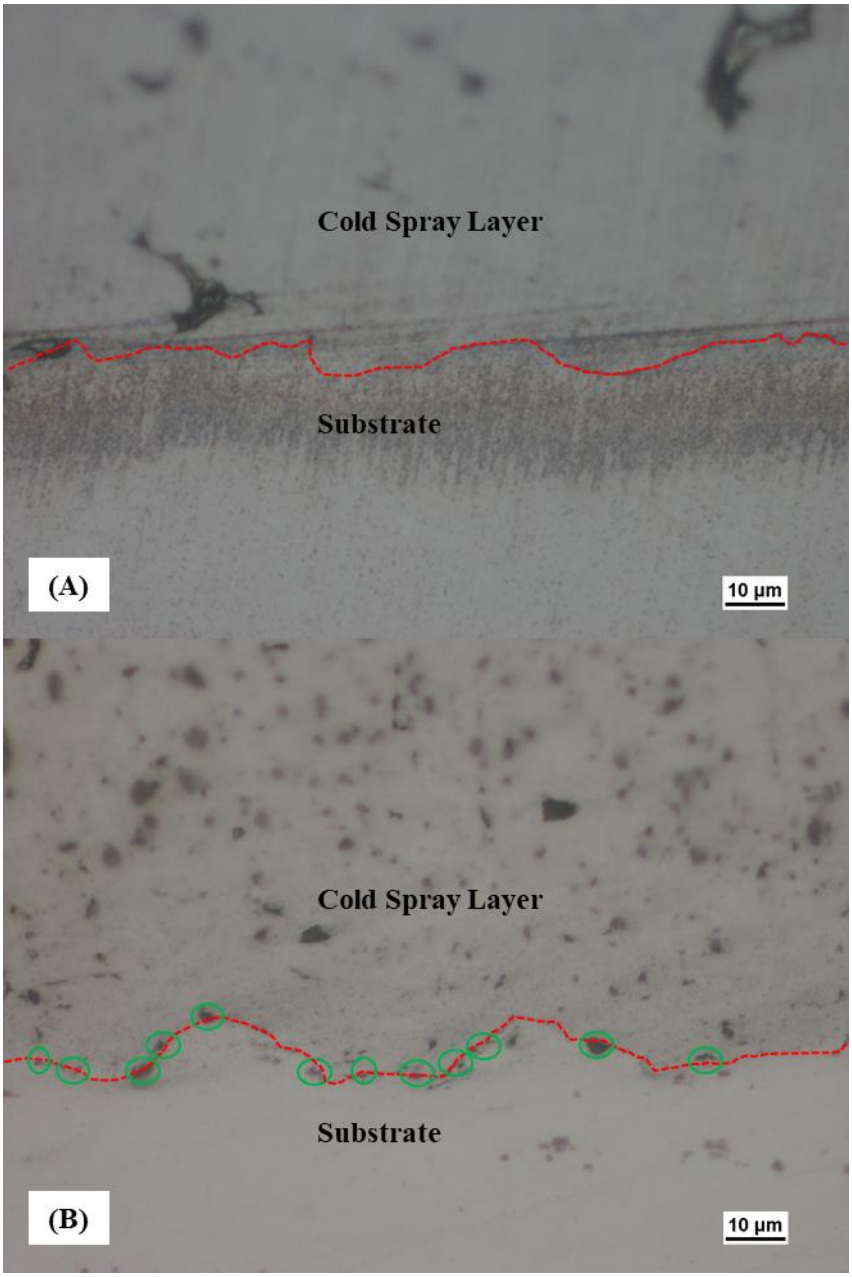

Figure 61. a) Al coating and Mg substrate interface b) Al/B_4C/BNNT coating and Mg substrate interface

After investigating the coatings with the SEM and optical microscope, the anomaly is the Al/B_4C coating. This coating failed at the highest force but does appear to have partially failed directly at the substrate, not within the coating itself. The greater vol.% of B_4C particles assisted in holding the Al splats together and outlasting the bonds between

the Mg substrate and the Al covered in B_4C. When the vol.% of B_4C is decreased in the Al/B_4C/BNNT coating, the failure mode is cohesive, i.e., the Mg substrate bonding with the B_4C covered Al is stronger than the B_4C anchoring Al splats to each other. Although, the B_4C failed at the substrate, the failure occurred at over 40 MPa! This value is magnitudes higher than the adhesion strength of Naval ship paint [50]. When designing for a strong cold spray coating, the tradeoff between an extremely high adhesion strength where failure occurs at the substrate (Al/B_4C) or a good adhesion strength where the failure occurs within the coating (Al/B_4C/BNNT) would need to be considered.

E. TENSILE TESTS

Two tensile specimens were sprayed with each composition These sprayed tensile bars then underwent tensile testing. In the following figures, the annotation "_1" after the composition indicates this is the first specimen tested and the annotation "_2" indicates the second specimen tested. Figure 62 shows the stress vs strain curves from the tensile testing of each cold spray coating in accordance with ASTM E8/E8M – 09. These curves consider the cross-sectional area of the cold sprayed tensile specimens found in Table 12. For this study, the most significant substrate and cold spray coating information comes from the elastic region of the curves before the material hits its yield point, outlined by the red box in Figure 62. In this region, it can be observed that each coating is deforming in a non-uniform way.

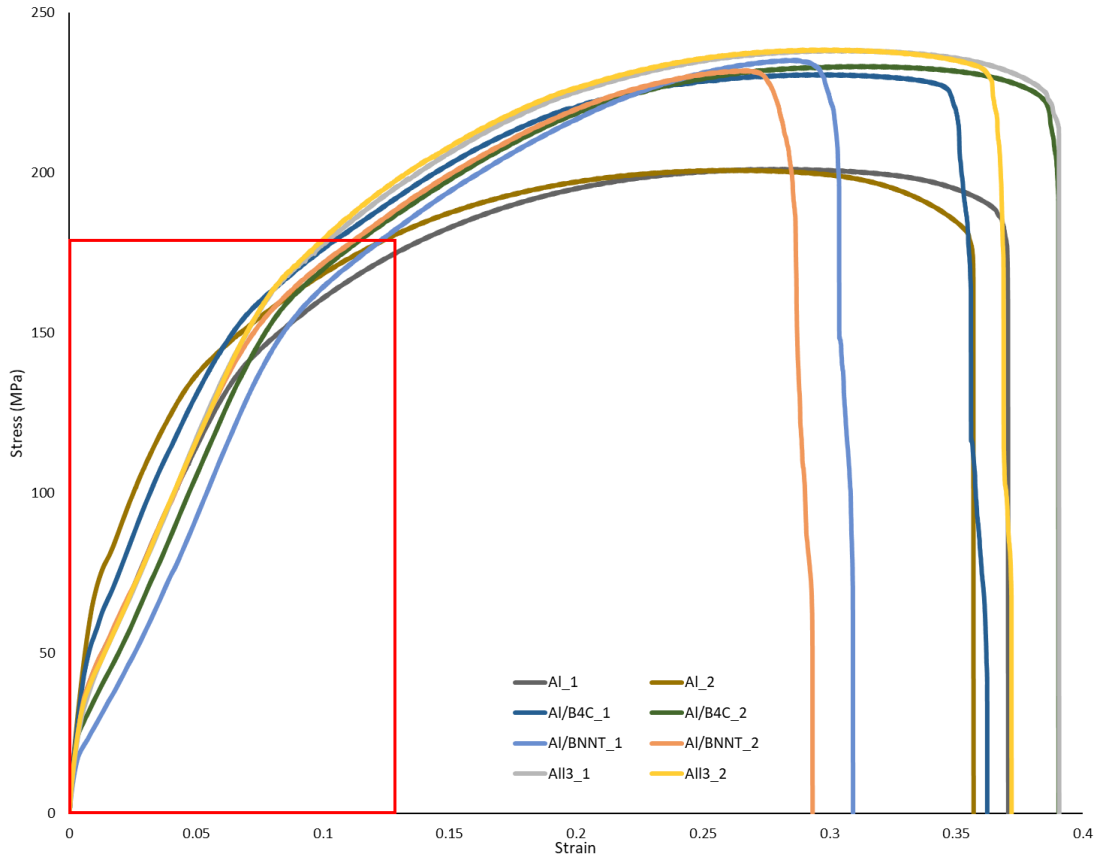

Figure 62. Stress vs. strain curves from tensile testing

Figure 63 is a generic AZ31 stress vs strain curve. An uncoated AZ31 specimen was not tested, so this curve's shape will be used as a reference; the actual stress values themselves are not as significant as the overall shape of the curve. Figure 64 shows the stress vs strain curves for all eight tests, focusing primarily on the elastic region. AZ31 exhibited traditional stress-strain behavior for a metal with a linear elastic region, a sharp transition corresponding to the yield point, and an inverted parabola indicating plastic behavior and eventual fracture. The coated AZ31 investigated here did not exhibit the same behavior. Instead, these eight curves each start with a steep, linear slope and then, at varying values of stress and strain, the curves each transition to a second linear elastic region with a more moderate slope.

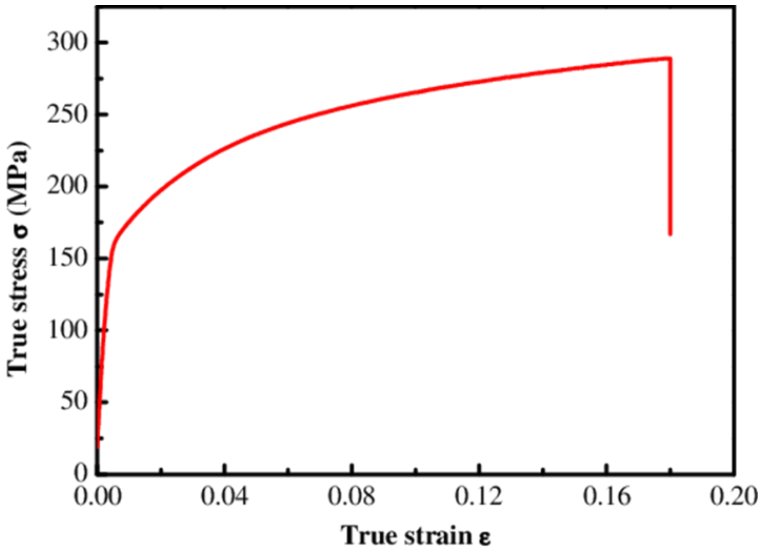

Figure 63. Generic AZ31 stress vs strain curve. Source: [49].

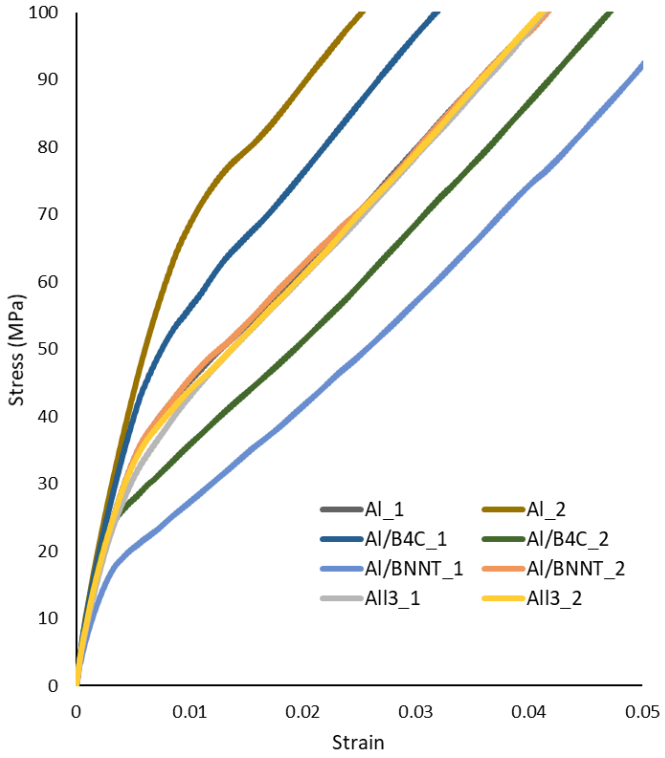

Figure 64. Elastic region of stress vs strain curves for each coating

Table 16 numerically displays the differences between these curves in the elastic region. The initial slope is where the coating theoretically is still intact and supports a percentage of the load. The rupture point is the approximate strain and stress in which the coating ruptures and the load is transferred to the AZ31 substrate. The final slope is the slope within the elastic region before the yield point (where the AZ31 substrate is fully supporting the load). The value of the final slope will not match published values for the elastic modulus of AZ31 due to the stresses the substrate has experienced throughout the cold spray process. Each composition's makeup and thickness are slightly different. This causes variance in how effective and how long they can assist in supporting the load. For these reasons, the initial slopes and the rupture points are skewed. It can be deduced that the load is being partially carried by the coating initially because of what happens after the rupture point: each composition adjusts to similar slopes until the yield point is reached, see Figure 64 beginning around a strain of 0.015. Meaning the load is now fully transferred to the AZ31 substrate.

Table 16. Stress vs. Strain Curve's Behavior in the Elastic Region

Composition	Initial Slope	Rupture Point	Final Slope
Al_1	6042.0	0.0058, 35.99 MPa	1760.8
Al_2	7450.4	0.0108, 70.92 MPa	1772.6
Al/B_4C_1	7473.5	0.0084, 52.40 MPa	1837.9
Al/B_4C_2	7406.2	0.0033, 24.24 MPa	1818.8
Al/BNNT_1	5028.2	0.0034, 17.80 MPa	1778.3
Al/BNNT_2	6816.9	0.0059, 36.48 MPa	1758.5
Al3_1	6860.0	0.0050, 30.74 MPa	1852.3
Al3_2	7013.6	0.0057, 35.05 MPa	1843.0

Figure 65 shows examples of each composition immediately before tensile failure. These coatings are weakly attached to the substrate between the tensile bar shoulders. At this point, the coatings have fully ruptured and are not supporting any of the load. Each coating is failing perpendicular to the tensile force. As experienced in the polishing and grinding steps, the coatings are much weaker when experiencing a shear force than a tensile force. Upon tensile failure, the coating is ejected from the substrate in between the tensile bar shoulders and the bars are left bare, or a very thin portion of the coating remains.

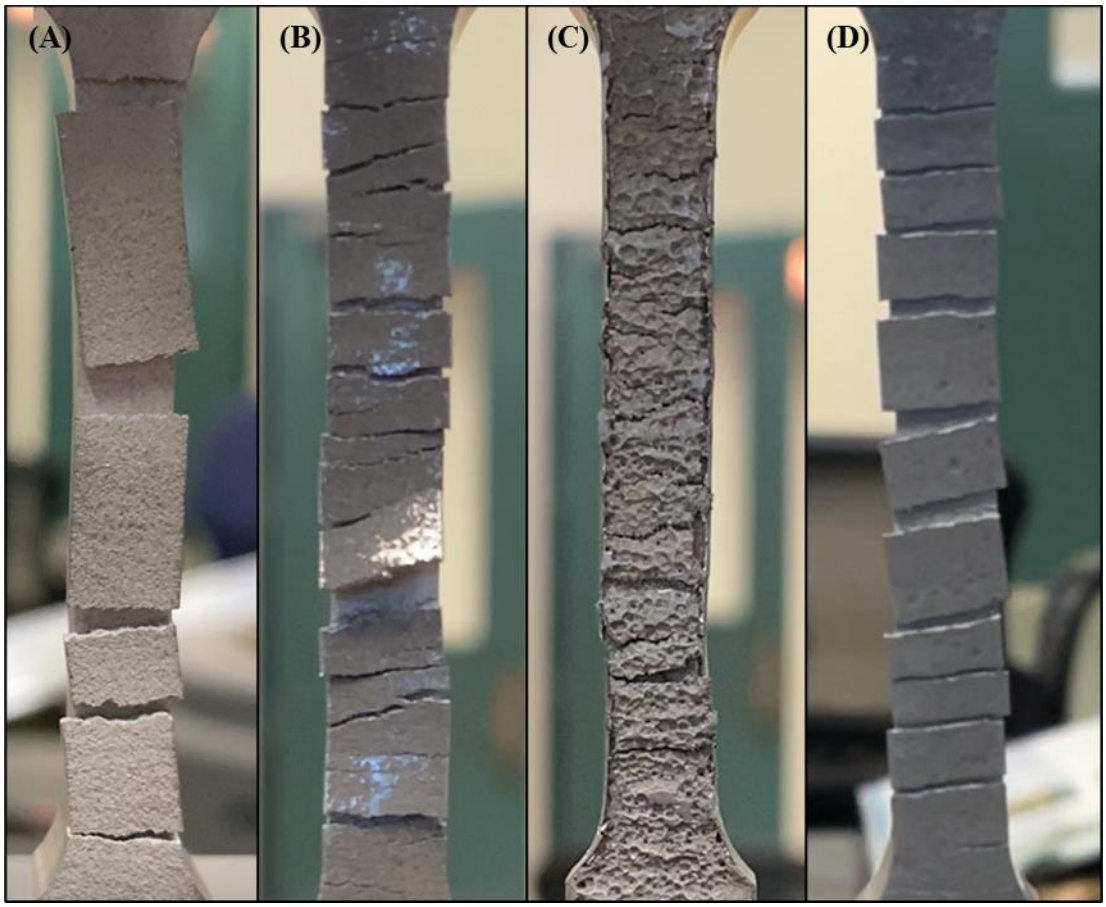

Figure 65. Coatings immediately before specimen failure during tensile testing a) Al b) Al/B_4C c) Al/BNNT d) All3

After the coatings were ejected from the substrate in between the tensile bar shoulders, the substrates were analyzed in the SEM. Images of the substrate surfaces from all four compositions post tensile testing are seen in Figure 66. The Al coating separated at the substrate while the Al/B_4C coating had a partial separation at the substrate and within the coating; pieces of the coating are visible on the substrate. The Al/BNNT and the Al/B_4C/BNNT coatings appear to have left a thin coating over the substrate. These results are similar to the adhesion tests. In every composition, except for the Al, there are lines traveling through the coating. These lines are perpendicular to the tensile force and show how the compositions failed.

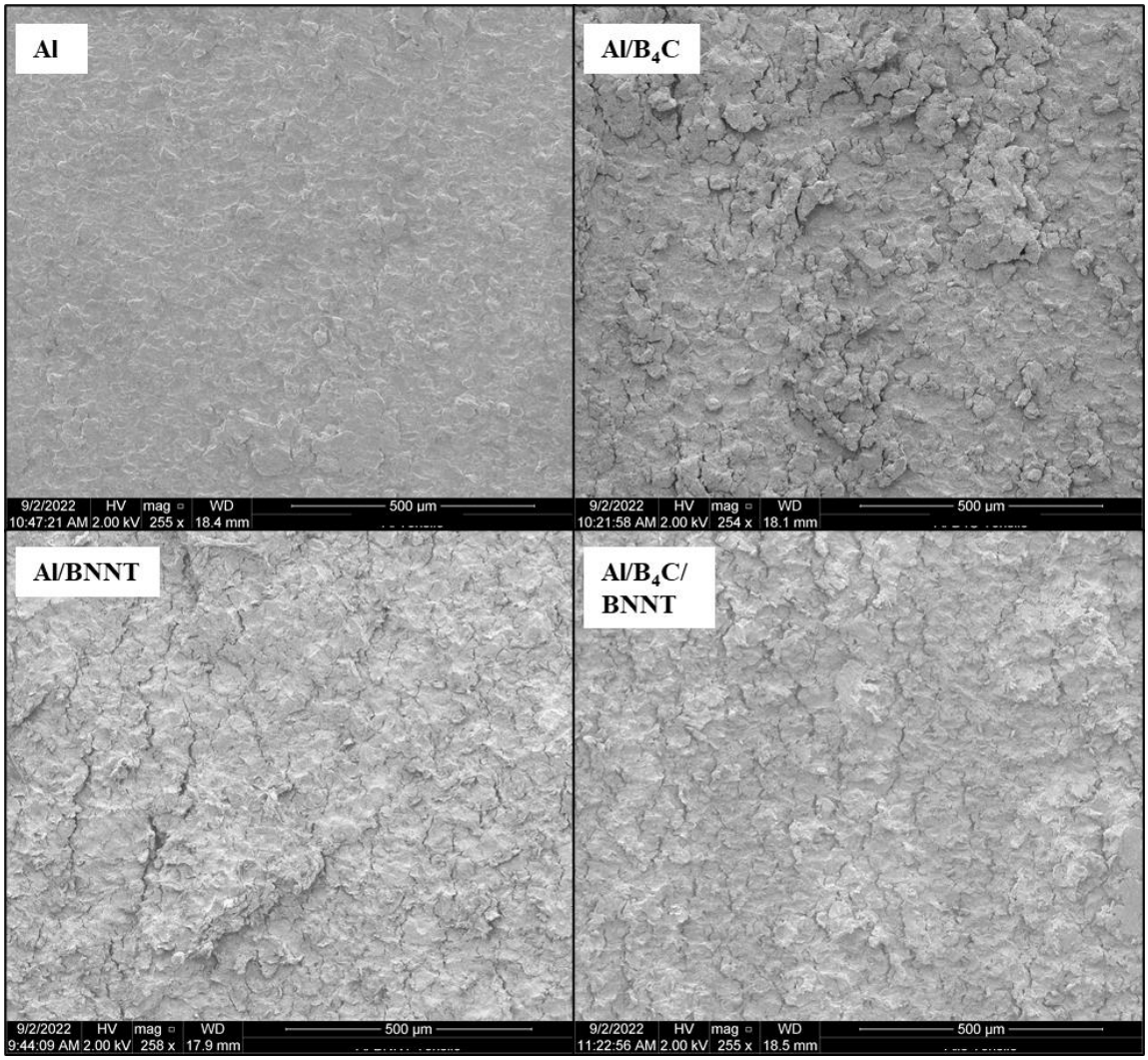

Figure 66. Top-down SEM images of the substrate area, between the tensile bar shoulders, after failure

Figure 67 shows the Al/B_4C composition that remained on the bar post tensile testing. The B_4C, circled in red, are positioned in between splats that have been pulled apart during tensile testing.

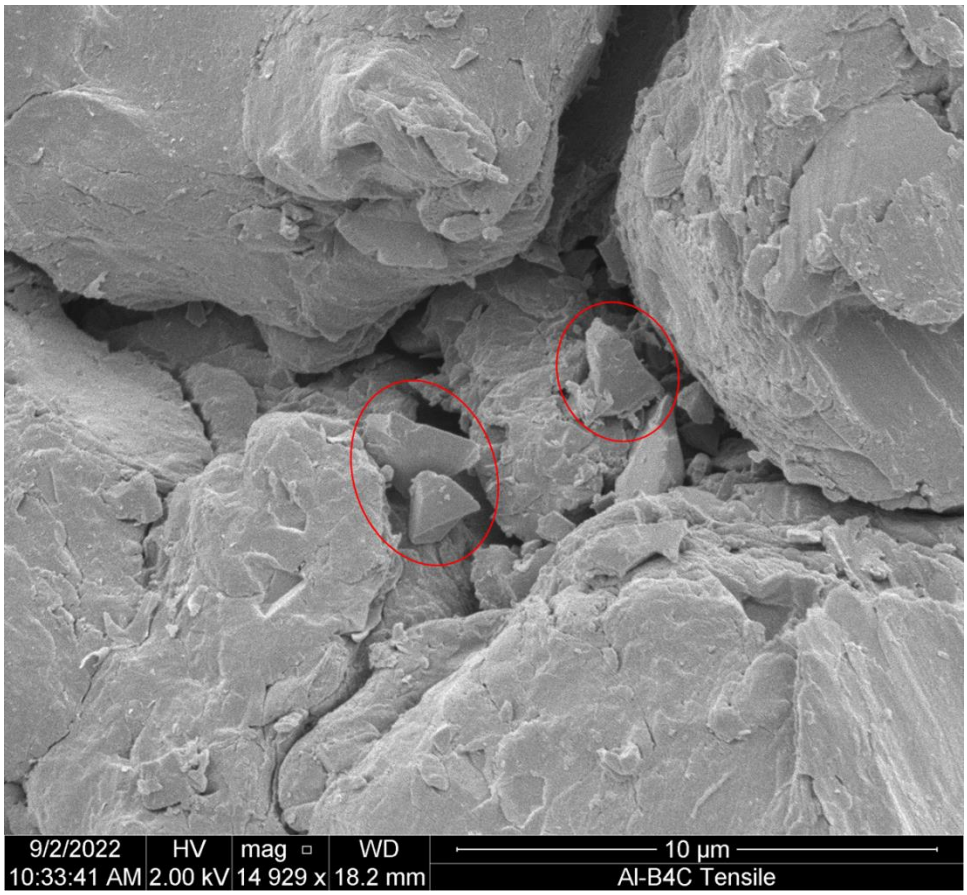

Figure 67. Al/B_4C tensile testing specimen showing the existence of B_4C between splats

Figure 68a and 68b show magnified images of the remaining Al/BNNT coating post tensile testing. The BNNTs are circled in red. Figure 68a shows multiple BNNTs that have failed as anchors within the composition during tensile testing. Figure 68b shows a single long, thin BNNT that is positioned at the bottom of one of the splat boundaries that were pulled apart during tensile testing.

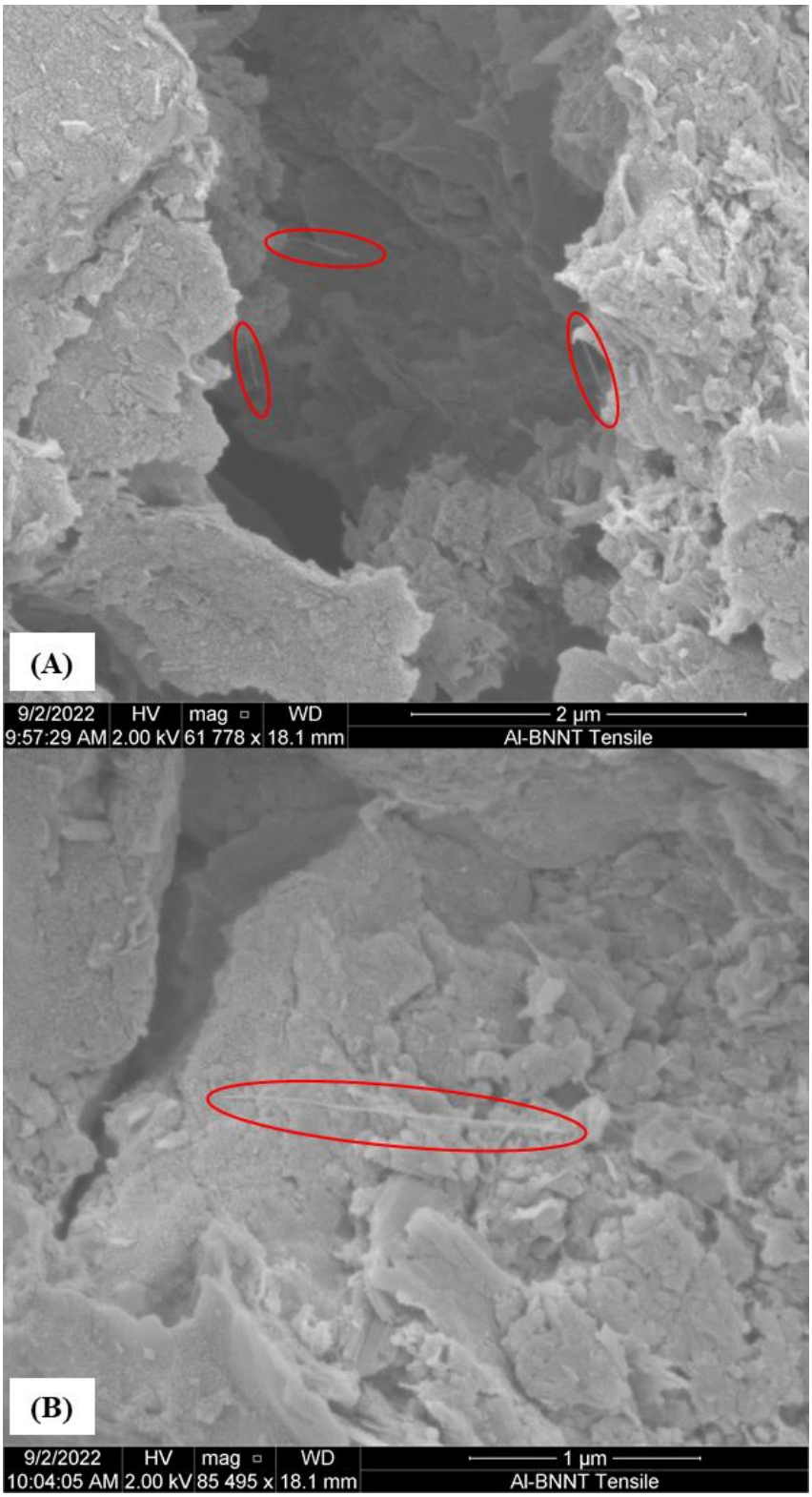

Figure 68. Al/BNNT tensile testing specimen a) BNNTs within splat boundaries b) single BNNT at the bottom of splat boundary

An Al/B_4C/BNNT splat boundary separated during the tensile testing is show in Figure 69. The B_4C along the boundary are circled in green and a BNNT is circled in red. Additional BNNTs are visible on the right side of the splat boundary. Figures 67 through 69 again show that the reinforcing ceramics, when properly dispersed within the Al matrix, can act as anchors between splats, resulting in resilient coatings.

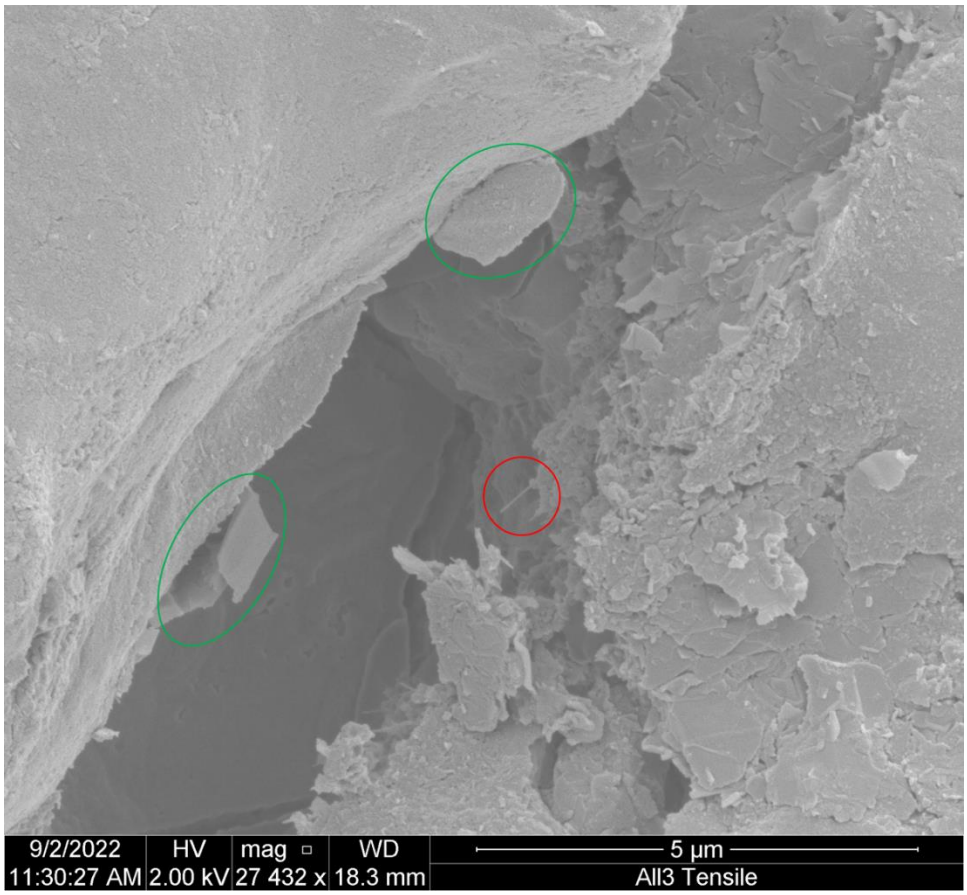

Figure 69. Al/B_4C/BNNT tensile testing specimen showing the existence of B_4C and BNNTs between splats

V. CONCLUSION

A. SUMMARY

This study lays a baseline for working with BNNTs in cold spray. BNNTs were utilized as both a single MMC reinforcement and a dual MMC reinforcement, along with B_4C. Although BNNTs have been used in different aspects of industry, material science, and additive manufacturing, this is the first time they have been successfully utilized in cold spray. As new cold spray coatings are developed and manufactured, there is increased potential for the DOD and industry to utilize these coatings for their specific traits that have been tailored to end user's particular application.

Adequate dispersion of the BNNTs and B_4C throughout an aluminum matrix by HEBM was achieved. These powders were successfully sprayed onto magnesium (AZ31) substrates with the 4 vol.% BNNT mixture having the lowest deposition efficiency, and the least uniform, thinnest coating. However, the dual reinforced coating, containing 2 vol.% B_4C and 2 vol.% BNNT, was sufficiently thick and uniform. The dual reinforced coating showed an increase over the control, pure aluminum coating in both the micro-hardness tests and the nanoindentation hardness tests. During tensile testing, all coating compositions influenced the elastic region of the stress vs strain curve; indicating the cold spray coatings do partially support the load until failure of the coating occurs. Primarily, this study showed BNNTs consistently provide strong adhesion to the magnesium substrate while allowing a cohesive failure to occur within the coatings. Extensive SEM imaging was conducted during all aspects of this study to qualitatively understand the influence that reinforcing ceramics have on the mechanical properties of the cold spray coatings.

B. FUTURE WORK

The cold spray compositions from this study will undergo additional testing and evaluation to include wear and EDS. New coatings will be sprayed with varying vol.% of BNNTs to quantify at what vol.% of BNNTs do the cold spray coating become uniform and thickness increases. Additional adhesion testing of the most promising coating, the dual reinforced coating, will be conducted after the coating is heat treated. Corrosion

resistance was not studied but could be further investigated by using a substrate that is less susceptible to corrosion and closer to pure aluminum on the galvanic series; possibly a marine grade aluminum alloy such as AA6061. The tensile specimens were affected by the cold spray coatings. To further see the effect on tensile data, a trial should be conducted using varying thicknesses of one cold spray composition.

LIST OF REFERENCES

[1] V. Champagne and D. Helfritch, "The unique abilities of cold spray deposition," *International Materials Reviews*, vol. 61, no. 7, pp. 437–455, Jul. 2016 [Online]. doi: 10.1080/09506608.2016.1194948.

[2] S. Kumar, M. Kumar, and N. Jindal, "Overview of cold spray coatings applications and comparisons: A critical review," *World Journal of Engineering*, vol. 17, no. 1, pp. 27–51, Jan. 2020 [Online]. doi: 10.1108/wje-01-2019-0021.

[3] S. Kuroda, J. Kawakita, M. Watanabe, and H. Katanoda, "Warm spraying—A novel coating process based on high-velocity impact of solid particles," *Science and Technology of Advanced Materials*, vol. 9, no. 3, p. 033002, Sep. 2008 [Online]. doi: 10.1088/1468-6996/9/3/033002.

[4] A. Papyrin, V. Kosarev, S. Klinkov, A. Alkimov, and V. Fomin, *Cold Spray Technology*. Oxford, UK: Elsevier, 2007.

[5] C.J. Li, W.Y. Li, Y.Y. Wang, G.J. Yang, and H. Fukanuma, "A theoretical model for prediction of deposition efficiency in cold spraying," *Thin Solid Films*, vol. 489, no. 1–2, pp. 79–85, Oct. 2005 [Online]. doi: 10.1016/j.tsf.2005.05.002.

[6] R. S. Lima, J. Karthikeyan, C. M. Kay, J. Lindemann, and C. C. Berndt, "Microstructural characteristics of cold-sprayed nanostructured WC–Co coatings," *Thin Solid Films*, vol. 416, no. 1–2, pp. 129–135, Sep. 2002 [Online]. doi: 10.1016/s0040-6090(02)00631-4.

[7] R. Raoelison, Y. Xie, T. Spanathan, M. Planche, R. Kromer, S. Costil, and C. Langlade, "Cold gas dynamic spray technology: A comprehensive review of processing conditions for various technological developments till to date," *Additive Manufacturing*, vol. 19, pp. 134–159, Jan. 2018 [Online]. doi: 10.1016/j.addma.2017.07.001.

[8] R. Huang and H. Fukanuma, "Study of the influence of particle velocity on adhesive strength of cold spray deposits," *Journal of Thermal Spray Technology*, vol. 21, no. 3–4, pp. 541–549, Dec. 2011 [Online]. doi: 10.1007/s11666-011-9707-0.

[9] S. Rice, "Enhancing mechanical properties of cold-sprayed aluminum coatings using graphene-nanoplatelet and micro-boron-carbide reinforcements," M.S. thesis, MAE, NPS, Monterey, 2022.

[10] D. L. Gilmore, R. C. Dykhuizen, R. A. Neiser, T. J. Roemer, and M. F. Smith, "Particle velocity and deposition efficiency in the cold spray process," *Journal of Thermal Spray Technology*, vol. 8, no. 4, pp. 576–582, Dec. 1999 [Online]. doi: 10.1361/105996399770350278.

[11] S. Singh, R. K. S. Raman, C. C. Berndt, and H. Singh, "Influence of cold spray parameters on bonding mechanisms: A review," *Metals*, vol. 11, no. 12, p. 2016, Dec. 2021 [Online]. doi: 10.3390/met11122016.

[12] A. Nieto, A. Agarwal, D. Lahiri, A. Bisht, and S. R. Bakashi, *Carbon Nanotubes: Reinforced Metal Matrix Composites*. FL, USA: Crc Press, 2021.

[13] P. D. Pastuszak and A. Muc, "Application of composite materials in modern constructions," *Key Engineering Materials*, vol. 542, pp. 119–129, Feb. 2013 [Online]. doi: 10.4028/www.scientific.net/kem.542.119.

[14] Y. T. R. Lee, H. Ashrafizadeh, G. Fisher, and A. McDonald, "Effect of type of reinforcing particles on the deposition efficiency and wear resistance of low-pressure cold-sprayed metal matrix composite coatings," *Surface and Coatings Technology*, vol. 324, pp. 190–200, Sep. 2017 [Online]. doi: 10.1016/ j.surfcoat.2017.05.057.

[15] AZoM, "Aluminium - Specifications, properties, classifications and classes," June 27, 2019 [Online]. Available: https://www.azom.com/ article.aspx?ArticleID=2863

[16] N. H. Tariq, L. Gyansah, J.Q. Wang, X. Qiu, B. Feng, M.T. Siddique, and T.Y. Xiong, "Cold spray additive manufacturing: a viable strategy to fabricate thick B_4C/Al composite coatings for neutron shielding applications," *Surface and Coatings Technology*, vol. 339, pp. 224–236, Apr. 2018 [Online]. doi: 10.1016/ j.surfcoat.2018.02.007.

[17] M. Yandouzi, A.J. Bottger, R.W.A Hendrikx, M. Brochu, P. Richer, A. Charest, and B.Jodoin, "Microstructure and mechanical properties of B_4C reinforced Al-based matrix composite coatings deposited by CGDS and PGDS processes," *Surface and Coatings Technology*, vol. 205, no. 7, pp. 2234–2246, Dec. 2010 [Online]. doi: 10.1016/j.surfcoat.2010.08.143.

[18] A. Sova, A. Papyrin, and I. Smurov, "Influence of ceramic powder size on process of cermet coating formation by cold spray," *Journal of Thermal Spray Technology*, vol. 18, no. 4, pp. 633–641, Jul. 2009 [Online]. doi: 10.1007/s11666-009-9359-5.

[19] A. Nieto, H. Yang, L. Jiang, and J. M. Schoenung, "Reinforcement size effects on the abrasive wear of boron carbide reinforced aluminum composites," *Wear*, vol. 390–391, pp. 228–235, Nov. 2017 [Online]. doi: 10.1016/j.wear.2017.08.002.

[20] J. Li, K. Hu, and Y. Zhou, "Formation of TiB2/TiN nanocomposite powder by high energy ball milling and subsequent heat treatment," *Materials Science and Engineering: A*, vol. 326, no. 2, pp. 270–275, Mar. 2002 [Online]. doi: 10.1016/s0921-5093(01)01499-x.

[21] J. H. Kim, T. V. Pham, J. H. Hwang, C. S. Kim, and M. J. Kim, "Boron nitride nanotubes: synthesis and applications," *Nano Convergence*, vol. 5, no. 1, Jun. 2018 [Online]. doi: 10.1186/s40580-018-0149-y.

[22] N. Kostoglou, C. Tampaxis, G. Charalambopoulou, G. Constantinides, V. Ryzhkov, C. Doumanidis, B. Matovic et al., "Boron nitride nanotubes versus carbon nanotubes: A thermal stability and oxidation behavior study," *Nanomaterials*, vol. 10, no. 12, p. 2435, Dec. 2020 [Online]. doi: 10.3390/nano10122435.

[23] K. S. Kim, M. J. Kim, C. Park, C. Fay, S. Chu, C. Kingston, and B. Simard, "Scalable manufacturing of boron nitride nanotubes and their assemblies: A review," *Semiconductor Science and Technology*, vol. 32, no. 1, p. 013003, Dec. 2016 [Online]. doi: 10.1088/0268-1242/32/1/013003.

[24] Y. Chen, M. Conway, J. S. Williams, and J. Zou, "Large-quantity production of high-yield boron nitride nanotubes," *Journal of Materials Research*, vol. 17, no. 8, pp. 1896–1899, Aug. 2002 [Online]. doi: 10.1557/jmr.2002.0281.

[25] N. G. Chopra, R. J. Luyken, K. Cherrey, V. H. Crespi, M. L. Cohen, S. G. Louie, and A Zettl, "Boron nitride nanotubes," *Science*, vol. 269, no. 5226, pp. 966–967, Aug. 1995 [Online]. doi: 10.1126/science.269.5226.966.

[26] P. Nautiyal, C. Rudolf, A. Loganathan, C. Zhang, B. Boesl, and A. Agarwal, "Directionally aligned ultra-long boron nitride nanotube induced strengthening of aluminum-based sandwich composite," *Advanced Engineering Materials*, vol. 18, no. 10, pp. 1747–1754, Jul. 2016 [Online]. doi: 10.1002/adem.201600212.

[27] D. Lahiri, A. Hadjikhani, C. Zhang, T. Xing, L. H. Li, Y. Chen, and A. Agarwal, "Boron nitride nanotubes reinforced aluminum composites prepared by spark plasma sintering: microstructure, mechanical properties and deformation behavior," *Materials Science and Engineering: A*, vol. 574, pp. 149–156, Jul. 2013 [Online]. doi: 10.1016/j.msea.2013.03.022.

[28] N. Yanar, E. Yang, H. Park, M. Son, and H. Choi, "Boron nitride nanotube (BNNT) membranes for energy and environmental applications," *Membranes*, vol. 10, no. 12, p. 430, Dec. 2020 [Online]. doi: 10.3390/membranes10120430.

[29] J. H. Kang, G. Sauti, C. Park, V. Yamakov, K. Wise, S. Lowther, C. Fay et al., "Multifunctional electroactive nanocomposites based on piezoelectric boron nitride nanotubes," *ACS Nano*, vol. 9, no. 12, pp. 11942–11950, Nov. 2015 [Online]. doi: 10.1021/acsnano.5b04526.

[30] K. K. Pandey, S. Singh, S. Choudhary, C. Zhang, A. Agarwal, L. H. Li, Y. Chen, and A. K. Keshri, "Microstructural and mechanical properties of plasma sprayed boron nitride nanotubes reinforced alumina coating," *Ceramics International*, vol. 47, no. 7, pp. 9194–9202, Apr. 2021 [Online]. doi: 10.1016/j.ceramint.2020.12.045.

[31] T. Norrell, G. Ferguson, T. Ansell, T. Saladin, A. Nardi, and A. Nieto, "Synthesis and corrosion behavior of cold sprayed dual nanoparticle reinforced Al coatings," *Surface and Coatings Technology*, vol. 401, p. 126280, Nov. 2020 [Online]. doi: 10.1016/j.surfcoat.2020.126280.

[32] Z. Li, G. Fan, Q. Guo, Z. Li, Y. Su, and D. Zhang, "Synergistic strengthening effect of graphene-carbon nanotube hybrid structure in aluminum matrix composites," *Carbon*, vol. 95, pp. 419–427, Dec. 2015 [Online]. doi: 10.1016/j.carbon.2015.08.014.

[33] H. Kwon, G.-G. Lee, S.-G. Kim, B.-W. Lee, W.-C. Seo, and M. Leparoux, "Mechanical properties of nanodiamond and multi-walled carbon nanotubes dual-reinforced aluminum matrix composite materials," *Materials Science and Engineering: A*, vol. 632, pp. 72–77, Apr. 2015 [Online]. doi: 10.1016/j.msea.2015.02.057.

[34] X. Zhang, S. Li, D. Pan, B. Pan, and K. Kondoh, "Microstructure and synergistic-strengthening efficiency of CNTs-SiCp dual-nano reinforcements in aluminum matrix composites," *Composites Part A: Applied Science and Manufacturing*, vol. 105, pp. 87–96, Feb. 2018 [Online]. doi: 10.1016/j.compositesa.2017.11.013.

[35] Centerline Limited Supersonic Technologies Div., "SST-A5001 technical data sheet," January 2020 [Online]. Available: https://www.supersonicspray.com/uploads/documents/SST-TDS-A5001-PR-2_0-0120.pdf

[36] Us Research Nanomaterials, Inc, "Boron carbide powder / B_4C powder (B_4C, 99.9%)," [Online]. Available: https://www.us-nano.com/inc/sdetail/6703

[37] BNNano, "Boron nitride nanobarb (TM) Powder - 1.0 gram," [Online]. Available: https://bnnano.myshopify.com/products/boron-nitride-nanobarbtm-powder

[38] L. Lu, S. Hu, L. Liu, and Z. Yin, "High speed cutting of AZ31 magnesium alloy," *Journal of Magnesium and Alloys*, vol. 4, no. 2, pp. 128–134, Jun. 2016 [Online]. doi: 10.1016/j.jma.2016.04.004.

[39] A. Dziubińska, A. Gontarz, K. Horzelska, and P. Pieśko, "The microstructure and mechanical properties of AZ31 magnesium alloy aircraft brackets produced by a new forging technology," *Procedia Manufacturing*, vol. 2, pp. 337–341, 2015 [Online]. doi: 10.1016/j.promfg.2015.07.059.

[40] J. Aroh, “Magnesium alloys for space hardware design,” NASA, Kennedy Space Center, Rep. 20170011677, 2017 [Online]. Available: https://ntrs.nasa.gov/api/citations/20170011677/downloads/20170011677.pdf

[41] SPEX Sample Prep, “Mixer/mill® high energy ball mill,” 2020 [Online]. Available: https://www.spexsampleprep.com/uploads/files/brochures/1006-113946-Mixer_Mill%20Brochure%202020.pdf

[42] G. F. Vander Voort, *Metallography, principles and practice.* Materials Park, OH: ASM International, 1999.

[43] W. C. Oliver and G. M. Pharr, “An improved technique for determining hardness and elastic modulus using load and displacement sensing indentation experiments,” *Journal of Materials Research*, vol. 7, no. 6, pp. 1564–1583, Jun. 1992 [Online]. doi: 10.1557/jmr.1992.1564.

[44] W. C. Oliver and G. M. Pharr, “Measurement of hardness and elastic modulus by instrumented indentation: Advances in understanding and refinements to methodology,” *Journal of Materials Research*, vol. 19, no. 1, pp. 3–20, Jan. 2004 [Online]. doi: 10.1557/jmr.2004.19.1.3.

[45] C. Comte and J. von Stebut, “Microprobe-type measurement of young’s modulus and poisson coefficient by means of depth sensing indentation and acoustic microscopy,” *Surface and Coatings Technology*, vol. 154, no. 1, pp. 42–48, May 2002 [Online]. doi: 10.1016/s0257-8972(01)01706-6.

[46] Masterbond, “EP15ND-2 Product Information | MasterBond.com,” [Online]. Available: www.masterbond.com. https://www.masterbond.com/tds/ep15nd-2

[47] A. Chua, “Mechanical behavior of cold sprayed Cu-Ni coating,” M.S. Thesis, MAE, NPS, Monterey, 2021.

[48] I. A. Ibrahim, F. A. Mohamed, and E. J. Lavernia, “Particulate reinforced metal matrix composites—A review,” *Journal of Materials Science*, vol. 26, no. 5, pp. 1137–1156, Jan. 1991 [Online]. doi: 10.1007/bf00544448.

[49] J. R. Xu, H. P. Yu, and C. F. Li, “Effects of process parameters on electromagnetic forming of AZ31 magnesium alloy sheets at room temperature,” *The International Journal of Advanced Manufacturing Technology*, vol. 66, no. 9–12, pp. 1591–1602, Aug. 2012 [Online]. doi: 10.1007/s00170-012-4442-3.

[50] The National Shipbuilding Research Program Surface Preparation and Coatings Panel, “Application of polysiloxane topcoats during navy shipbuilding,” 2015 [Online]. Available: https://www.nsrp.org/wp-content/uploads/2015/09/Deliverable-2014-430-Polysiloxane_vs_Silicone_Final_Report-Bath_Iron_Works.pdf

THIS PAGE INTENTIONALLY LEFT BLANK

INITIAL DISTRIBUTION LIST

1. Defense Technical Information Center
   Ft. Belvoir, Virginia

2. Dudley Knox Library
   Naval Postgraduate School
   Monterey, California